Observational studies of the Martian low-latitude cloud belt(Dissertation_全文)

AUTHOR(S):

Nakakushi, Takashi

CITATION:

Nakakushi, Takashi. Observational studies of the Martian low-latitude cloud belt. 京都大学, 2003, 博士(理学)

ISSUE DATE:

2003-03-24

URL:

https://doi.org/10.14989/doctor.k9944

Observational studies of the Martian low-latitude cloud belt

Takashi Nakakushi

Kwasan Observatory, Graduate School of Science, Kyoto University

Ph. D. Thesis
submitted to the Department of Astronomy, Faculty of Science,
Kyoto University

Dedicated to my father,
Kazuyoshi Nakakushi

Abstract

This is a thesis on the Martian climate, based on our observations in 1997, 1999 and 2001. The central substance is the low-latitude cloud belt, which appears in northern summer and is considered to be coupled with the Martian seasonal climate variation.

We have established a calculation algorithm on our own in order to solve the radiative transfer equations and to directly estimate the cloud optical depths. Such methods had not yet been given elsewhere. This algorithm is primarily based on the well-known "discrete-ordinate" method, which is originally introduced by *Chandrasekhar* [1960]. We extend his idea based on the numerically stable methods of *Liou* [1973], and the "matrix method" given by *Stamnes and Swanson* [1981] and *Stamnes and Dale* [1981]. Phase functions are approximated by the "δ-M method" introduced by *Wiscombe* [1977]. The key idea to derive the optical depth of a certain atmospheric component is the assumed constant optical depths of other constituents. Furthermore, to improve confidence of the ground-based observations, we introduce a new statistical procedure, which treats a "regional-mean" value rather than a value at a certain point on Mars.

The 1997 and 1999 apparitions were around its northern summer oppositions. Mars showed highly developed clouds that formed the low-latitude cloud belt. Comparing the diurnal variations of the apparent contrasts of Syrtis Major to the adjacent bright areas with those of the optical depths of the low-latitude clouds over those regions, we conclude that the time when those regions are subject to the morning clouds is around 0900 Martian Local Time (MLT) and that the diurnal variation of the degree of blue clearing strongly depends on the difference between the optical depth of water ice clouds over Syrtis Major and that over the adjacent bright area. Moreover, our simple linear regression analyses of the degree of blue clearing to the optical depths of water ice clouds suggest that the key region in which the water ice cloud optical depth determines the degree of blue clearing is Syrtis Major.

The next focus is the dissipating behavior of the low-latitude cloud belt appearing around the aphelion, the behavior of which has never been explicitly examined. We derive the optical thickness of water ice clouds (WICs) as $\tau_{\rm WIC} \approx 0.1$ ($\lambda \simeq 4400$Å) at solar longitude $L_s = 174^\circ$ in 2001. The latitudinal coverage of the cloud belt is approximately L_s-independent just until its end. The cloud belt divides into a "semi-encircling" cloud band and discrete WICs before its dissipation (over $L_s \sim 100^\circ$-110°) in many cases. We suggest that this cloud division should embody localization of the cross-equatorial Hadley circulation.

This thesis is mainly based on the results in two papers; *Nakakushi et al.* [2001a], published on *Journal of Geophysical Research, 106*, 5043-5056; *Nakakushi et al.* [2002a], published on *Publications of the Astronomical Society of Japan, 54*, L31-L34. The computing codes for the estimation of the optical depths used in these papers and described in Part II are fruits of collaboration with T. Akabane and S. Saito. The author improved the algorithm and codes by dealing with a large image dataset and many target points, which enables statistically more faithful analyses. The author also carried out all the data analyses, discussions, and summaries presented in those papers and this thesis. The observations included were conducted together with the co-authors of the two papers.

Contents

List of Figures

List of Tables

Part I

General Introduction

Chapter 1

Introduction

Mars is, as the traditional description has it, a brother of Earth. Despite all the observational difficulties, long before the beginning of spacecraft exploration, Mars was already a popular topic of science discussion (and public speculation).

Mars has an atmosphere, polar caps, and widespread geological evidence of the former presence of rivers, glaciers, and even oceans. Yet the atmosphere today is a frigid veil of carbon dioxide, less than 1% of the atmospheric pressure of Earth, so cold that water is found as vast deposits of ice and wisps of water vapor. Liquid water is certainly very rare, and possibly absent, on the surface of Mars today. Where are the volatiles that Mars should have had at the time of its formation? How much water did the planet accrete, and how much was present near the surface at the end of accretion? How was the atmosphere lost? Where is the water gone? Did Mars indeed have abundant water and a much more massive atmosphere in its early history, only to lose it? How did the surface inventory change with time? How and when did the fluvial features form? What climatic conditions were required for their formation? How and when did the climate change? *What caused Mars to turn out as it did? Could the same thing happen to us?* These challenging questions have been driven many researchers to Martian paleoclimatology. In addition, many spacecraft launched and approached, landed, and observed (or some have been observing) Mars to find many new things and to develop our knowledge. These situations may have many non-areophysicists[1] talk as if all but the past-to-present climate changes and the search for the missing matters were miscellaneous researches.

NEVER! IT IS WRONG!!

The main concern is with the presence throughout this thesis. The present Martian climate, in particular, behavior of water ice clouds is the central issue. This chapter begins with an overview of the situation of recent planetary science and of "areophysics."

1.1 Background

1.1.1 The Present Situation of Solar System Science, and Planetology

Some scientists say, " The solar system is not an objective of astronomy/astrophysics any longer." (They are often astrophysicists, for some reason.) Perhaps he or she excludes the sun — in anyway, his or her statement is correct, in a sense. However, if he or she continues, "It has already been the target of geophysics," it is wrong in many senses — except the Earth itself.

[1] "areo-" is a combining form which means "Mars" or "Martian."

In terms of scientific fields, planetary science is a mixture of astronomy/astrophysics, geophysics, astrochemistry, geochemistry, and space science/technology. Astrobiology (and space medicine) might be included. In terms of methodology, the way to solar system bodies consists of observational, theoretical, technological, experimental, and recently, numerical approaches. Therefore, solar system bodies are already in a new *interdisciplinary* field. Within this new field, studies focusing the nine planets have been gradually admitted as "planetology" as well as "planetary science" recently. Whatever its name may be, researchers should know better than to ask what kind of (conventionally-categorized) field the solar system *should* belong to. Nevertheless if you still insist, the answer is: "Solar system bodies are the objectives of solar system science."

The arguments in this section are to be quite natural for every researcher that majors in planetology. That is why the author dares to claim it here.

1.1.2 "Areophysics"

Even within the "planetology" within the "solar system science," the interests are vast. That is, even if we focus only on the nine planets, they are quite different from one another. This situation is similar if we further confine our interests within the terrestrial planets (or the Jovian planets).

As stated in the beginning of this part, Mars have long been the most familiar and gravitating planet for astronomers in history. We do not repeat the "tales" of the earlier centuries because Mars is still of our interest without them, of course.

Mars is particularly interesting because of its similarities and differences compared to Earth (see Table 2.1). Among them, the highly important *similarities* are:

- Earth and Mars have very similar rotation rates and axial tilts.
- Both have relatively transparent atmospheres through which solar radiation penetrates to the surface much of the time.
- Carbon dioxide is an important radiating gas in the thermal infrared for both planet.
- The temperature regime of Mars is more like that of Earth than of any other planet.

The most striking *difference* is, of course, that Mars do not have oceans. The second is its large orbital eccentricity, so that the seasonal phasing are important factors for Mars' present climate, but of relatively minor importance for Earth today. Of course there are other important aspects worthy of special mention. All of them characterize the present Martian climate. We will extend these issues of the significant contributions to the uniqueness of Mars in the next chapter.

Changes in the surface and atmosphere of Mars have been observed for many years [e.g., *Slipher*, 1962; *Martin et al.*, 1992]. Similarly to the usual astronomical observations, a particular phenomenon of interest is observable through an appropriate filter. Figure 1.1 shows samples of filtered images. Generally said, bright condensate clouds show on ultraviolet-, blue-, and sometimes green-filter images, but are usually absent on red-filter images. On the contrary, red-filtered images generally provide surface albedo markings, and prevailing airborne dust clouds.

It has been difficult to telescopically distinguish repetitive seasonal variability from interannual variability because of the large variations in the apparent angular size of Mars during its 780 day synodic cycle; it imposes a 15 to 17-year periodicity in scientifically useful observation

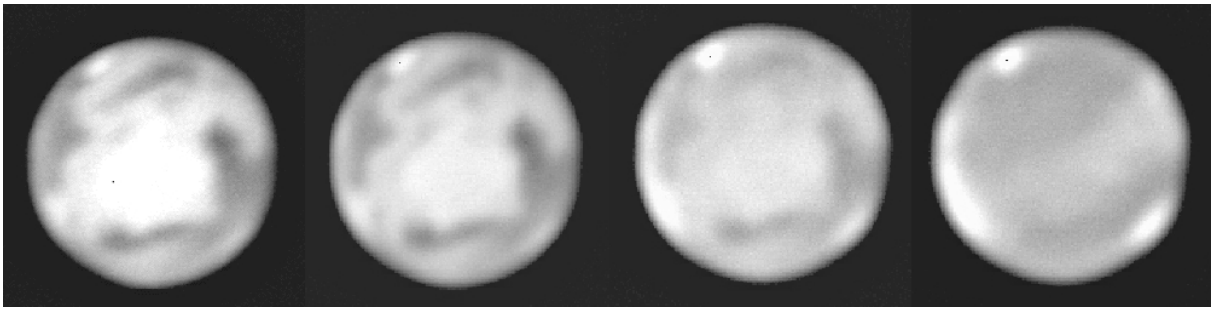

Figure 1.1: Filtered images of Mars. These images were taken on March 4, 1997 ($L_s = 86°$, the sub-solar latitude $D_s = 25°$N, the sub-Earth latitude $D_e = 23°$W,). The wavelengths, time, and the sub-Earth longitude (LON_{SE}) were 751nm on 16:06 UT, $LON_{SE} = 324°$W; 647nm on 16:08 UT, $LON_{SE} = 325°$W; 549nm on 16:14 UT, $LON_{SE} = 326°$W; 436nm on 16:19 UT, $LON_{SE} = 327°$W (left to right). The upper-left direction is the north on Mars.

of a particular Martian season, specified by the areocentric solar longitude L_s. Spacecraft observations have revealed details of the seasonal variations on Mars during a few Martian years, but the time span limited by these observations precludes conclusions on the amount of interannual variability in the climate. Also, most spacecraft observations have lacked the synoptic character and repetition frequency necessary to study atmospheric phenomena. The most serious shortcoming of (terrestrially) ground-based observations compared to those by spacecraft is that quantitative discussion is generally difficult. Although the direct observations by spacecraft (both orbiters and landers) must be densely widespread in order to activate theoretical and numerical studies, data points (not simply the amount of database) are seriously insufficient. The every approach available now has intrinsic advantage and disadvantage: there is no perfect one. The most important is to deal with them weighted equally, and the "areophysics" have met a new phase to do so.

1.2 Preview

This thesis gives some insights on the seasonal low-latitude water ice cloud belt based on our recent ground-based imaging observations. As pointed out in the previous section, only a few *quantitative* Earth-based investigations, especially those of the diurnal variation of the cloud activity, have been accumulated. For instance, *Erard* [2000] said, "Atmospheric opacity cannot be measured from the images, because standard stars are not available for each night and the images cannot be calibrated in intensity." However, we have enabled quantitative analyses of the water ice opacity.

The greater part of the results in this thesis are based on the water ice optical depth. Before we go into the details, we outline the present Martian climate and atmospheric aerosols, including some descriptions of our observations in 1997, 1999, and 2001, in the rest of Part I. Because opacity of water ice clouds is the key in this study, the rest of this thesis starts with a complete description of our algorithm for the retrieval of the opacity of water ice clouds (Part II). These sections (the rest of Part I, and Part II) forms the combined introductions appeared in the two published papers in which the author played a role of the first author (*Nakakushi et al.* [2001a] on *Journal of Geophysical Research*, and *Nakakushi et al.* [2002a] on *Publications*

of the Astronomical Society of Japan). Part III shows what we named the "cloud effect": the effect of the low-latitude cloud belt on the blue clearing phenomena (based on *Nakakushi et al.* [2001a]). Part IV discusses the dissipating behavior of the cloud belt (based on *Nakakushi et al.* [2002a]). These results in the two parts above are unique in the history of Mars research, which results are mostly owed to the author. The summary of this thesis is presented in Part V.

Chapter 2

Overview of the Martian Atmosphere

In this chapter, we describe some important aspects of the present Martian atmosphere and climate. Of course, there are too many to complete here. Among them, we highlight most closely related matters to the scope of this thesis, the low-latitude seasonal cloud belt, that is, the most characteristic substance of northern summer climate.

2.1 Basic Atmospheric States

2.1.1 Outline: North-South Asymmetry

Table 2.1 shows some scientific up-to-date facts of Mars. As seen in the table, although the atmospheric pressure is surely more similar to that on Earth than any other planets, it is rather small, so that the specific heat is also much smaller to that of the Earth's atmosphere, and the response to thermal forcings are much rapider than Earth, accordingly. This low pressure considerably limits the water vapor pressure, leading to the dry atmosphere.

The term "north-south asymmetry" is a kind of *double entendre* ; geometrical/geological and climatological/meteorological asymmetries between the northern and southern hemispheres. The geometrical asymmetry is clearly recognized in Figure 2.1. The northern hemisphere is relatively smooth and free of craters, with an ice-cap that is mainly composed of water. The southern polar cap contains carbon dioxide, and the surrounding terrain is heavily cratered.

The topography of a planet can reveal much about its evolution. Crater density is one of clues to estimate the geological age: the more cratered southern hemisphere is thereby considered to be older than the northern hemisphere [e.g., *Carr*, 1996]. *Smith et al.* [1999] have obtained a high-resolution global view of the topography of Mars from Mars Global Surveyor. They showed the inter-hemispherical difference in elevation is averagely $\sim$ 5km (see also Figure 2.1). In addition, their data confirmed that the high elevations of the southern hemisphere reflect internal processes and showed that a widespread deposit from an impact crater forms much of the high elevations. Furthermore, they suggested that surface water over much of the planet would have drained into a large basin in the northern hemisphere.

Hemispheric dichotomies are not unusual in the solar system. Earth (continent-dominant in the north and ocean-dominant in the south) and the moon (lava plains on the nearside and the heavily cratered farside) are good examples. Unlike the moon, however, Mars has an atmosphere that can transport dust and water vapor around the planet. Hence, one might expect that, over

Table 2.1: Mars Facts.

Orbit semimajor axis	1.52366 AU
Eccentricity	0.0934
Obliquity	25.19°
Mean orbital period	1.8809 Earth solar years†
	686.98 Earth days
	669.98 Mars solar days (sols)
Mean solar day	24^{h} 39.6^{m}
	1.0260 Earth solar days†
Synodic Cycle	779.9 Earth solar days†
Mean radius	3389.92 km *
Surface gravity at equator	3.711 m s^{-2}
Bond albedo ‡	0.16†
Mean atmospheric pressure at surface	560 Pa
Average mass of atmosphere	2.17×10^{16} kg
Mean atmospheric scale height	10.8 km

All the data, except those with a dagger (†) from *National Astronomical Observatory* [2001], are from *Carr* [1996].

* This is equivalent geometrically to ~ 60 km deg^{-1} on the ground surface.

‡ The *Bond albedo* is the ratio of the amount of light reflected by a body into all directions to the amount of light incident on the body. This is important for the energy balance on a planet. The Bond albedo is also called the spherical of integrated albedo.

the long term, atmospheric mixing would lead to a balanced distribution of polar ice. This is not what we see, however.

Another striking difference in atmospheric phenomena is the seasonal behavior, in particular, during the summers in the respective hemispheres. Dust storms, which may be the most well-known, are mostly confined during southern summer; the activity of water ice clouds, orographic clouds and the seasonally appearing water ice cloud belt which encircles the whole equator in particular, characterizes northern summer. This difference has been attributed to the planetary eccentricity and the fact that perihelion occurs just before the southern summer solstice (see Figure 2.2), resulting in solar incident radiation being as much as 44% higher than experienced in northern summer occurring around aphelion: southern summer is shorter, but more intense than northern summer.

2.1.2 Atmospheric Thermal Structure

In terms of thermal balance in a planetary atmosphere, we can separately treat the incident sunlight and the thermal emission from the planet because the respective energy peaks and distributions are sufficiently different in wavelengths each other.

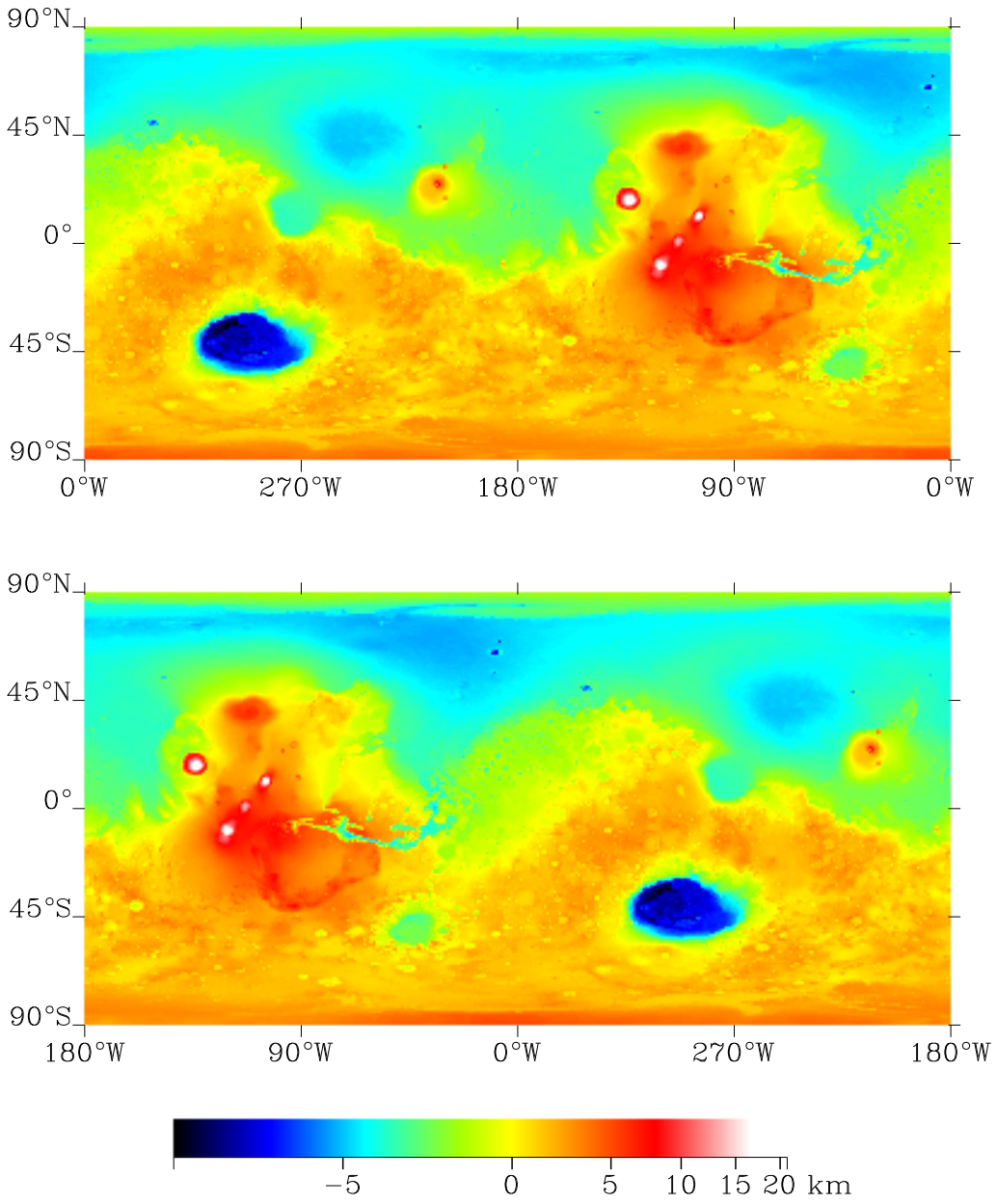

Figure 2.1: Mars topography with $1^\circ \times 1^\circ$ resolution. "Topography" is defined as the difference between the planetary radius and the areoid radius for each point. The plotted data is the median of each $1^\circ \times 1^\circ$ bin ("median topography"). This map is produced from the MGS MOLA (Mars Orbiter Laser Altimeter) data. The digit data are available in a table from on World Wide Web (the initial experiment gridded data records "IEG100_A.TAB" on the "MOLA Topographic Map" site, http://wufs.wustl.edu/missions/mgs/mola/iegdr.html), distributed by the NASA Planetary Data System (PDS) [http://pds.jpl.nasa.gov/].

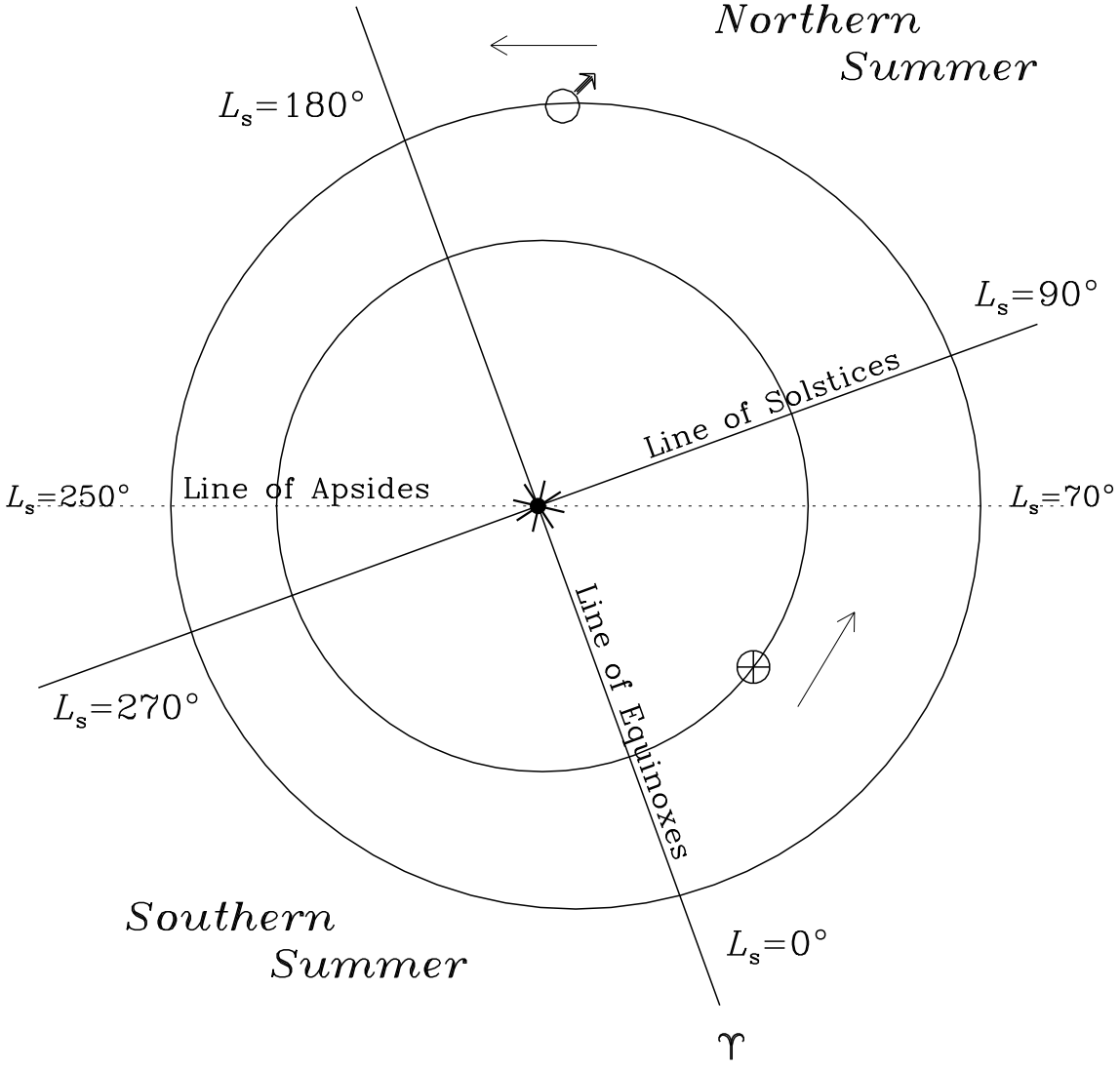

Figure 2.2: Mars orbit.

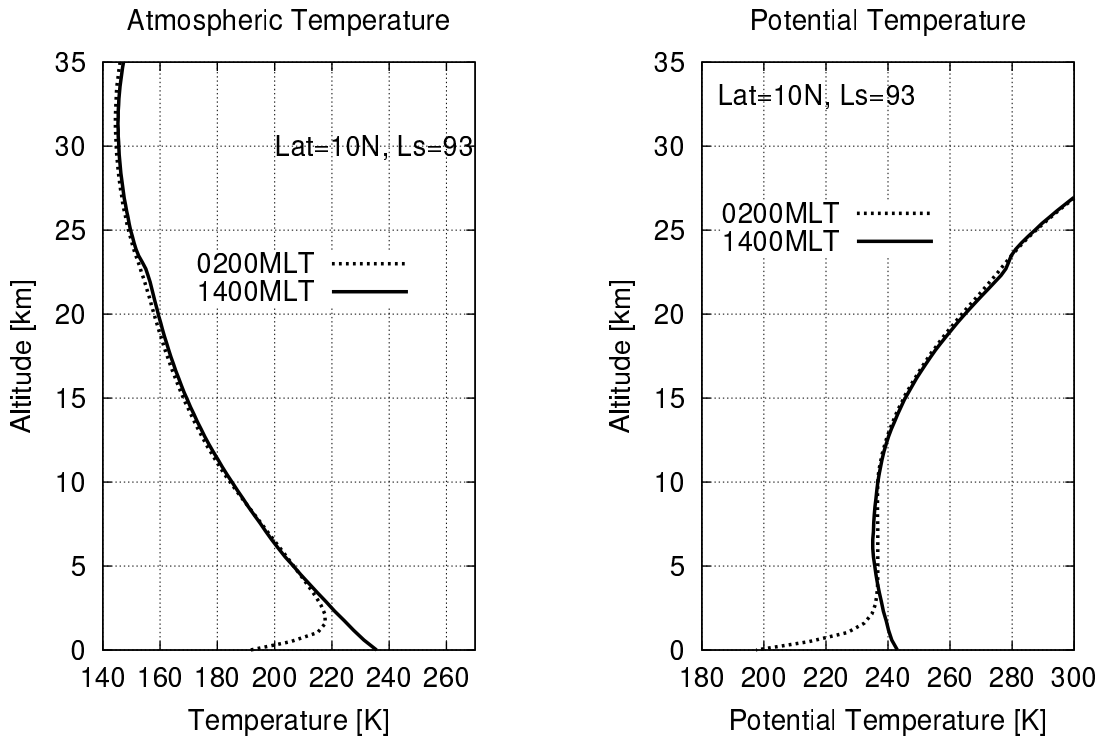

Figure 2.3: Samples of atmospheric thermal structure.

On Mars, the atmosphere is too thin for molecular scattering to be of great importance; it has too little ozone or water vapor for either to influence solar or thermal radiation very strongly, while these constituents play dominant roles to the temperature structure in the Earth's stratosphere and troposphere, respectively. Also for the same reason, the latent heat exchanges of CO_2 and water are not dominant except in the polar night where the latent heating of CO_2 is important. Hence, radiation is the primary source of diabatic heating and cooling of the atmosphere. When present, suspended dust is the dominant absorber and scatterer of sunlight in the atmosphere. In a clear atmosphere, CO_2 is the main instead. In the thermal infrared, dust and CO_2 are again the dominant sources of opacity.

Such significant influences of airborne dust can be recognized, for example, in the fact that the observed Viking Lander data were warmer and more isothermal than predicted by a radiative-convective one-dimensional model without the effects of aerosols. The situation is more apparent in dustier condition, i.e., southern summer. From a different viewpoint, we can expect that if we take these radiative effects of aerosols into account, energy balance models will produce a reliable temperature profile of the atmosphere: indeed, *Pollack et al.* [1979] succeeded it in the lower atmosphere.

Figure 2.3 depicts samples vertical profiles of the atmospheric temperature and the potential temperature[1] for the northerly tropics (10°N) at 0200MLT and 1400MLT in a northern summer

[1]The definition of potential temperature is

$$\Theta = T\left(\frac{P}{P_0}\right)^{-R/c_\mathrm{p}}, \tag{2.1}$$

where R and c_p are the gas constant and the specific heat for a constant pressure, respectively, for CO_2 gas.

solstice ($L_s = 93°$) obtained from our preliminary calculation [*Nakakushi et al.*, 2002b] with a one-dimensional energy balance model based on *Narumi* [1994, 2000]; *Flasar and Goody* [1976]; *Blumsack et al.* [1973]. There exists a inversion by radiative cooling from the ground at midnight, and in the daytime the (dry) adiabatic lapse rate[2] is realized below ∼10-15km, which is regarded as the troposphere. This situation is more distinct in the potential temperature profile (Figure 2.3, the right panel).

While atmospheric water vapor does not have significant influence to thermal structure, the situation is different with respect to water ice clouds. Suspected CO_2 ice particles in polar hoods are similar. The clouds can indirectly affect atmospheric cooling by scavenging suspended dust and lowering its vertical distribution in the ice particle condensation [e.g., *Clancy et al.*, 1996; *Zurek et al.*, 1992]; a direct effect of the clouds is the radiative heating and/or cooling of the atmosphere and surface. Although the latter effect may not be significant for large-scale motions except the optically thick extended polar hoods, it can affect local temperature profiles. It has been suggested that local inversions, such as in the Mars Pathfinder (MPF) descent profile [*Magalhães et al.*, 1999], may be generated by radiative cooling by water ice clouds [e.g., *Haberle et al.*, 1999; *Colaprete and Toon*, 2000].

Most of our knowledge of the Martian atmospheric thermal structure, and the consequent climate models, had been based on the "successful" Viking missions in the 1970s, although we should not have easily rely on the data as the constant condition because there may be some interannual variations. However, the Viking *de facto* standard model of the Martian atmosphere may not be trustworthy even for the Viking period. *Wilson and Richardson* [2000] present evidence for a positive bias in the Viking IRTM (Infrared Thermal Mapper) 15μm radiances due to an unaccounted contamination from surface emission, which leads to substantial contribution from diurnal and latitude-dependent surface emission of Mars. The differences between the suggestions in 1990s claiming a more colder and clearer condition as the normal state [e.g., *Clancy et al.*, 1996; *Richardson*, 1998] and the previous Viking model were substantially reduced by *Wilson and Richardson* [2000] reanalysis of the Viking 15μm radiances. On the contrary, from an intercomparison of these observations by *Clancy et al.* [2000], the entire 1997-1999 period of observations by MGS TES (Thermal Emission Spectrometer) and millimeter measurements (1.3 and 2.6mm rotational spectra of Mars atmospheric CO, see *Clancy et al.* [1996] and references therein, for details) are 10-20K colder than have been inferred from Mars Pathfinder (on July 4, 1997, 19.17°N, 33.21°W [*Golombek et al.*, 1997], 0400MLT, $L_s = 143°$)[3], as well as the uncorrected Viking data.

2.2 Atmospheric Aerosols and Clouds

Martian cloud can have one of two forms: condensed volatile (or white) clouds and dust (or yellow) clouds.

2.2.1 Suspended Dust and "Yellow" Clouds

Dust has a profound impact on the Martian atmosphere. It is both an effective absorber of solar radiation and an effective emitter/absorber of thermal infrared radiation, as seen in the previous

[2]The dry adiabatic lapse rate is defined by:

$$\Gamma = \frac{g}{c_{\mathrm{p}}} \tag{2.2}$$

with the gravitational acceleration rate g on Mars.

[3]The intercomparison by *Clancy et al.* [2000] state that the MPF descent was at 0400MLT and $L_s = 143°$, while *Schofield et al.* [1997] state that it was at 0300MLT and $L_s = 142°$. In any case, this is too tiny a difference.

sections. Consequently, the amount and distribution of dust in the atmosphere significantly affects atmospheric heating rates and hence the circulation.

Actually, dust storm, which have been known since the last century, is the most impressing feature in the southern summer, which corresponds to the perihelion period. Several successful spacecraft encountered, and sometimes suffered from global dust storms. Such situations, especially those of the spacecraft, led many researchers to pay (or concentrate) their attention to dust activity. Further, dust had been treated as if it were the only dominant to the Martian climate, in particular, since the Viking missions succeeded, and so had it been even in the subsequent theoretical studies, too.

This conventional view of suspended dust as if it were the one and only important substance in the role of climate was challenged by *Clancy et al.* [1996] (and several meeting papers thereafter).

2.2.2 Condensate Particles and "White" Clouds

Of course, dust surely has a profound impact on the Martian atmosphere, as seen in the previous sections. However, dust is not the only aerosol in the atmosphere. Water ice and CO_2 ice particles also form in the atmosphere.

Martin et al. [1992] stated: "More common than yellow clouds are these Martian 'white' or 'blue' clouds." Actually, telescopic observations from at least as early as 1796 have shown the presence of "white" or "bluish" features in the Martian atmosphere (cited by *Tamppari et al.* [2000]), however, the history may have begun earlier: *Pearl et al.* [2001] introduced a similar story by citing *Herschel* [1784]. Anyway, these clouds have also been observed through most of the recorded history of telescopic observations.

Studying Martian "white" clouds is old and new. Although its history is old, the importance of condensate clouds, water ice clouds in particular, had gradually fade away because of the realistic amount of water on Mars and the realistic pressure of the atmosphere. While the role played by water is surely one of the most intriguing aspects of the past-to-present epochal evolution of Mars, at present, the atmosphere contains only minute amounts of water, liquid water is unstable everywhere. The present Martian climate is thus distinctly different from the terrestrial climate, which is decisively driven by phase changes of water; so different as to keep areophysicists away from atmospheric water in the post-Viking years.

The extensive work of *Clancy et al.* [1996], which suggested that water may play an essential role in the present climate of Mars, made various activities of water focused again. They proposed the interactive and interdependent mechanism between water activity/cycle and the north-to-south asymmetry of climate due to the seasonal temperature structure, and thus atmospheric dynamics. Since then, water ice clouds have been observed by spacecraft at Mars and telescopes on Earth or in orbit around it (e.g., the Hubble Space Telescope, HST). Actually, such recent studies show the importance of water ice clouds/hazes and water vapor in terms of Martian climatology. Investigation of present water activity hence gets more and more importance because water ice/vapor can be referred to as a dominant and/or subdominant atmospheric constituent, or an "indicator" subject to the background atmospheric and climatic/meteorologic condition.

Several types of condensate clouds have been observed. They may show up as diffuse and widespread hazes or as well-delineated discrete clouds. Morphological features and optical characteristics of Martian condensate clouds, mainly water ice clouds, have been secured by several techniques (Table 2.2), and as many morphological categorizations for clouds have been proposed. *Slipher* [1962] and *Martin et al.* [1992] summarize the morphological features of clouds

Table 2.2: Cloud Observations (Some Examples).

Visual observations	*Miyamoto* [1965, 1968, 1974]
Imaging observations	
Earth based	*Slipher* [1962], *Martin and Baum* [1969], *Smith and Smith* [1972], *Martin and Mckinney* [1974], *Hattori and Akabane* [1974], *Akabane et al.* [1980, 1987, 1995]; *Parker et al.* [1999]
Mariner 9	*Leovy et al.* [1972, 1973], *Curran et al.* [1973], *Briggs and Leovy* [1974]
Viking 1, 2	*Briggs et al.* [1977], *Pickersgill and Hunt* [1981], *French et al.* [1981], *Christensen and Zurek* [1984]
HST†	*James et al.* [1994, 1996], *Wolff et al.* [1999]
Polarimetric observations	*Dollfus* [1961], *Dollfus et al.* [1984, 1996], *Lee et al.* [1990]

† Hubble Space Telescope.

observed by ground-based telescopes. Cloud motions and morphology observed from spacecraft have greatly contributed to our understanding of "meteorological" scale phenomena (i.e., synoptic scale, or mesoscale in some cases) which cannot be detected by ground-based telescopes, as well as to inference of characteristics of the large-scale circulation and atmospheric stability.

Some condensed clouds may consist of CO_2 ice particles, but most of them in low to mid latitudes in northern summer are considered to be water ice clouds [e.g., *Smith and Smith*, 1972]. Hereafter, statements on condensate clouds without further notes imply water ice clouds (an example of the exceptions is the case of polar hoods, appearing in the next subsection). In addition to condensates, many of these clouds may also contain dust and are often seen in association with dust clouds [e.g., *Martin*, 1976]. Discrete white clouds may appear either singly or in groups. Most discrete clouds remain relatively stationary for days at a time, but those in dust storms display rapid movement.

The following are brief descriptions of the rather common things on condensate clouds, along morphological types of clouds.

2.2.2.1 Polar hoods

Condensate clouds and hazes known as polar hoods have been observed to cover both polar regions during winter. They also are often seen around the periphery of the polar caps, especially the north cap [e.g., *James et al.*, 1987]. Clouds also form a southern autumn polar hood, with strongest brightenings in the Hellas and Argyre basins [*James et al.*, 1996]. The polar hoods may contain CO_2 ice particles.

From the visibility of the "Lowell band," a dark marking (streak) in north polar cap, *Erard* [2000] reported that the northern polar hood dissipated by $L_s \sim 55^\circ$ in the 1994-1995 apparition. Furthermore, from the timing of the polar hood dissipation and the appearance limb clouds in

tropics, he suggested a migration of clouds from polar latitudes to the equator.

2.2.2.2 Sub-polar clouds

One of the regional and seasonal groups that water ice clouds occur predominantly is the northern sub-polar region during winter [e.g., *Akabane et al.*, 1995]. They also occur in the southern sub-polar region during southern winter, but are much less common than in the north [e.g., *Akabane et al.*, 2001]. Unique images of mesoscale spiral cloud structures, resembling the cloud forms in terrestrial polar cyclones, have been observed near the periphery of the summer residual north polar cap [e.g., *Snyder and Moroz*, 1992, Fig. 11].

2.2.2.3 Hazes, fogs, and small clouds

Using Mariner 9 and Viking imaging data, *French et al.* [1981] systematically cataloged cloud features as various types, including fogs, plumes, streaky clouds, cloud streets, wave clouds and lee waves; they then examined the spatial and seasonal variability of these types. Wave clouds, particularly lee waves, are common in the sub-polar regions and during morning hours in the tropical regions. Streaky and patchy cloud forms of uncertain origin appear in both regions. *Kahn* [1984] rebuilt this catalog, using all Mariner 9 and Viking Orbiter images and adding three categories of thin, moderate and thick haze; mosaics were used to define the context of features in individual images. Kahn then used this data base to constrain winds, static stability and, of course, humidity.

Fogs (i.e., very low lying clouds) may not have sufficient thermal contrast to be detected even by instruments aboard spacecraft using thermal emissions (e.g., IRTM on Vikings, and TES on MGS) and may often be outside the daytime window examined in many works [e.g., *Tamppari et al.*, 2000]. Although ground fogs are difficult to detect, their presence have been predicted, for example, by one-dimensional energy balance model [e.g., *Flasar and Goody*, 1976]. The radiative cooling of the ground surface throughout the nighttime may probably form them. Such ground fogs may form earlier hours [e.g., *Nakakushi et al.*, 2002b], which may contribute the high brightness (and opacity) of morning clouds (see the next).

HST observed a predawn cloud viewed near the morning limb of Mars on February 24, 1995, the altitude of which was estimated to be $\sim$ 8km [*James et al.*, 1996]. The predawn cloud was probably not orographic in nature. The cloud altitudes of 5-10km are consistent with the study of *Clancy et al.* [1996], which will be repeatedly cited many times in this thesis along the discussion of the low-latitude seasonal cloud belt (see Section 2.3.3). Judging from the estimated altitude of the predawn cloud, the cloud may belong to the same category as the cloud belt, although the result from one particular cloud can not be conclusive. Most recently, the Mars Pathfinder camera (Imager for Mars Pathfinder, IMP) observed predawn bluish clouds [*Smith et al.*, 1997]. In addition, the presence of a thin, diffuse ice haze (i.e., $\tau \sim 0.01 - 0.02$) have been suggested [e.g., *Kahn*, 1984].

2.2.2.4 Morning and evening clouds

Mars displays limb and/or terminator hazes much of the time that are occasionally small but may be generally quite extensive, both north-south along the planet's edge, as well as extending out onto the bright disk.

They are generally called "morning clouds" and "evening clouds" according to their appearing hours. Morning and evening clouds in early stages are often recognized simply as regional limb clouds, which appear at $L_s = 50°$-$60°$ [e.g., *Erard*, 2000]. Some orogenic clouds may be

included [*Akabane et al.*, 2002]. However, the on-image place of appearance of those clouds is rather stationary regardless of Mars rotation, so that morning/evening clouds may not always consist of orographic clouds. Morning/evening clouds, whether orogenic clouds may be there or not, gradually increase their brightness and dimension during northern spring [e.g., *Akabane et al.*, 2002, Fig. 2].

As will be introduced in Section 2.3.3 in spring to summer of the northern hemisphere, these low-latitude water ice clouds form a seasonal cloud belt, which encircles the planet in spring to summer of the northern hemisphere [*Clancy et al.*, 1996]. Relationship between this seasonal cloud belt and morning/evening clouds is one of the foci of this thesis.

2.2.2.5 Orographic clouds

White condensate clouds have also been observed in the tropics during the northern summer (already appearing by $L_s \sim 50°$, typically), particularly over the Tharsis and Elysium uplands, and during the afternoon [e.g., *Smith and Smith*, 1972; *Leovy et al.*, 1973; *Briggs et al.*, 1977; *James et al.*, 1994; *Clancy et al.*, 1996; *Akabane et al.*, 2000; *Erard*, 2000; *Akabane et al.*, 2002].

Akabane et al. [2002] argued: "Owing to those (Table 2.2) and other observations it is known that three types of cloud appear in low latitudes of both hemispheres and mid latitudes of the northern hemisphere in northern spring to summer. They are morning, evening, and afternoon clouds. Regions in which all of the three types of orographic cloud appear are restricted to two large orogenic areas in northern low latitudes: Elysium and Tharsis." Their "morning" and "evening" clouds may be defined somewhat differently from those introduced in the previous section because theirs are orographic clouds, in their context. In their definitions, the "afternoon clouds" on Elysium Mons is as bright as those on Olympus Mons, but "morning" and "evening clouds" in Elysium are much less active than those in Tharsis.

The clouds in Tharsis are bright and conspicuous, and have been morphologically studied. This characteristic cloud over Tharsis Mons consists of the discrete clouds associated with the Tharsis volcanoes and Valles Marineris. This cloud system has been historically called "W" clouds due to their appearance in an inverted telescope image [e.g., *Slipher*, 1962; *Akabane et al.*, 1987]. The term "W" clouds was applied by E. C. Slipher to a group of clouds he observed while in Chile during 1907. The "W" clouds were prominent in the $L_s = 60°$ images acquired in both 1991 *James et al.* [1994] and 1995 *James et al.* [1996].

The morning, evening, and afternoon orogenic clouds in Tharsis repeat significant diurnal variation for a long period in northern spring to summer, and the relative intensities of the components of the "W" complex are known from ground-based astronomy to shift from year to year; data relevant to day-to-day variations with fixed local time are not common, but ground-based images suggest that such changes occur slowly, if at all [e.g., *Slipher*, 1962; *Smith and Smith*, 1972; *Briggs et al.*, 1977]. During the 1981-82 apparition, *Akabane et al.* [1987] measured the optical thickness of an Olympus Mons cloud. They determined that it had a peak value of about 0.5 near 1400MLT. Their recent work have shown that the optical thickness of the Tharsis morning cloud was more than 1 in the early morning and reduced to ~ 0.2 around noon in 1995, and that those of the Olympus afternoon cloud reached ~ 0.7 in the early afternoon in 1997.

Some combination of these clouds has been observed many times over the years. The same pattern may persist for several weeks. The regular appearance of clouds in the cycle of a day, as shown by *Akabane et al.* [2002], may suggest that meteorological conditions repeat in the same period. However, in a more closer view, the configuration may different during each apparition it is observed and may change from one day to the next, and the relative sizes and brightness of individual clouds may vary. The importance of these difference depends on scale of the

phenomena, and thus what to be discussed.

Interannual variation is most likely responsible for differences in the clouds observed in HST images acquired at $L_s = 60^\circ$ in 1991 and 1995; in 1991 the clouds near Alba Patera and the western portion of Valles Marineris (i.e., Tithonius Chasma) were the most prominent components, while in 1995 the cloud to the west of Ascreus Mons was considerably brighter than the Alba cloud. The Olympus Mons cloud was brighter than in 1995 than it was in 1991. The locations of the clouds to the west of the major topographical highs is consistent with the predictions of circulation models which predict topographically induced positive vertical velocities in these regions *Haberle et al.* [1993]. Some of them are over or displaced slightly from the great volcanic shields of Tharsis and/or Olympus Mons (Slipher's "W" did not include Olympus). Other clouds have associations with more subtle topographic features such as Alba Patera or smaller features; but some may not relate to topography at all.

2.3 Dynamics

2.3.1 Atmospheric Waves, and Thermal Tides

Waves in the atmosphere are loosely separated into two parts by their forcings: dynamical and thermal. Observations, both remotely sensed and *in situ*, have revealed the presence of various large-scale wave motions in Mars' atmosphere. Numerical modeling has predicted that other types of such motions are almost certainly present as well, awaiting detection in future data. Such waves are important in several contexts: one of the most important aspects is the role of atmospheric waves in the horizontal and vertical transport of heat, momentum, and suspended dust, water ice/vapor, and other atmospheric constituents. Large-scale waves are generated by atmospheric instabilities and spatially asymmetric "external" forcings. They are traveling baroclinic waves, thermal tides, free mode waves, forced quasi-stationary waves, and other transient waves.

In general, *tides* of the atmosphere of a planet are those produced in two very different ways by (a) the gravitational forces of the satellite(s) and/or the sun, and (b) the thermal action of the sun, i.e., differential heating. The latter is the forcing of what is called a *thermal tide*, which is a large component of the total longitudinal and temporal variability, primarily because of the strong daily varying solar heating (per unit mass). In the summer hemisphere in particular, strong winds due to thermal tides are expected to be prominent because of weaker winds due to the global circulation. On the other hand, gravitational tides are negligible on Mars, of course, because of the small satellites. As it has been expected and reported, the latest observations by MGS TES revealed that the time-independent wave modes of integral wave number in longitude (globally coherent stationary waves) and wave modes varying with a frequency of an exact multiple of 1 sol^{-1} (solar thermal tides) are prominent, and more prominent is those of lower order (i.e., of smaller wavenumber) [e.g., *Banfield et al.*, 2000; *Smith et al.*, 2001].

Here we express the oscillating thermal structure as below [e.g., *Chapman and Lindzen*, 1970; *Banfield et al.*, 2000]:

$$T = \Re e \left\{ \sum T^{\sigma,s}(\theta, z) e^{i(\sigma t + s\phi)} \right\} + T^{\mathrm{secular}}(\theta, z)(t - t_0) \tag{2.3}$$

where

T	temperature
θ	latitude
z	altitude
t	time
ϕ	east longitude
σ	frequency (wavenumber in time)
s	(zonal) wavenumber
$T^{\sigma,s}(\theta, z)$	the complex amplitude of a particular wave mode
$T^{\text{secular}}(\theta, z)$	the amplitude of the secular drift mode
t_0	a reference time, the mean value of t

and σ is positive by convention.

When we deal with only the most prominent modes above-mentioned, the limited combinations of σ and s are allowed. For the globally coherent modes, the limited frequences are those of $s = 0, 1, 2, \ldots$. Note that when we only consider integer values of σ, then we can treat time as periodic with period 1 sol (except for with the secular term). Essentially, this is an echo of the fact that most of our interests are in wave modes that vary repeatably over exactly a sol. The stationary modes all have no time variation, that is, $\sigma = 0$. The solar tidal modes have a phase speed equal to that of the sun,

$$c_{\text{sun}} = -1 = c_{\text{phase}} = -\frac{\sigma}{s},$$

which leads to $s = \sigma$. Finally, the tidal modes produced from interactions between the sun-following tides (of longitudinal wavenumber $s_0 = \sigma$) and longitudinal variations in heating or topography (of longitudinal wavenumber m) can be expressed as the sum of terms with $s = s_0 \pm m$ This leaves us with three groups of modes, in addition to the secular term:

(1)	The stationary modes	$\sigma = 0,\ s = 0, 1, 2, \ldots$
(2)	The sun-following tidal modes	$\sigma = 1, 2, 3, \ldots,\ s = \sigma$
(3)	The longitudinal variation forced tidal modes	$\sigma = 1, 2, 3, \ldots,\ s = \sigma \pm m$ (for $m = 1, 2, 3, \ldots$)

On both Earth and Mars, the properties of the predicted thermal tides are [*Lindzen*, 1966; *Zurek*, 1980];

(1) the *semidiurnal tide* ($\sigma = 2, s = 2$) has a long vertical wavelength and responds efficiently elevated and vertically extended heating sources. On Mars, such a heating source occurs only during the periods of greatest dust opacity (i.e., global dust storms) and is temporary.

(2) the *diurnal tide* ($\sigma = 1, s = 1$) has a short vertical wavelength and its vertical propagation is likely disturbed by destructive interference. In a relatively clear atmosphere, the forcings are trapped near the ground because the large daily variation produced in the ground temperature generates a thermotidal drive by the convective heat flux in the daytime and by radiative exchange between the atmosphere and ground during both day and night, so that the diurnal mode becomes prominent.

These studies of the waves present in Mars atmosphere have put useful but limited constraints on atmospheric models.

2.3.2 The General Circulation

The term "general circulation" denotes the large-scale aspects of the atmospheric circulation, thermal structure and pressure distribution, particularly when averaged longitudinally and/or when averaged over periods long enough to remove variations associated with daily fluctuations and with individual weather systems, but still short compared to seasonal variations, usually with emphasis on the region above the boundary layer. At all scales, much of our current understanding has come from modeling studies of various types; although the current meteorological data of Mars on observational bases have been accumulated, their temporal and spatial particularities do not allow the general circulation to be defined diagnostically. Even so, the available data can still provide insights into many aspects of the general circulation.

Presence of a zonal-mean circulation of the Martian atmosphere have been inferred from observations [e.g., *Zurek et al.*, 1992]. For example; (1) the large excess of winter mid-latitude temperatures above their radiative equilibrium values, (2) the few wind directions determined from cloud drifts and morphology [*Kahn*, 1984], (3) the zonal winds derived from latitudinal temperature gradients, (4) the observed distribution of so-called "Type I(b)" bright streaks and their orientation, (5) the intense polar warmings during great dust storms observed at the Viking Landers.

Of course the Martian general circulation can have several complicated structures. Among them, the greatest interest for this thesis lies in the well-known cross-equatorial Hadley circulation, which is commonly predicted by numerical experiments [e.g., *Haberle et al.*, 1993]. Models indicate that, in solstitial seasons, the rising branch should be in the spring/summer hemisphere and the descending branch should be in the fall/winter hemisphere. Near equinox there may be two overturning cells, with rising air near the equator and sinking air a few tens of degrees poleward in both hemispheres; there may also be a brief transition from one summer pattern to the opposite hemisphere's spring pattern. The equinoctial 2-cell pattern can be said to resemble that in the Earth' troposphere, in which these upwelling and downwelling belts create the cloud and rain characteristic of the equatorial rain forests, and the dry, clear atmosphere over the subtropical deserts. On the contrary, the solstitial cross-equatorial Hadley circulations (and the atmospheric backgrounds) are comparable to those in the Earth's stratosphere.

On Mars, the solstitial cells are not equal intensity or extent. The dominant southern summer Hadley cell is roughly twice as intense as that of the northern summer [e.g., *Haberle et al.*, 1993]. Very similarly to the explanations for the north-south Martian divide (Section 2.1.1), this is also firstly (but partly) due to the eccentricity of the Martian orbit and the consequential asymmetry of the solar radiative heating. It has been recently suggested that the topographic asymmetry may be another cause [*Gierasch*, 2002; *Richardson and Wilson*, 2002]. The problem is a very difficult one, however. The interaction of topography with atmospheric motions is not well understood even in the Earth's atmosphere.

2.3.3 The Low-Latitude Cloud Belt

In spring to summer of the northern hemisphere, clouds in low latitudes form a seasonal cloud belt, which encircles the planet [e.g., *Clancy et al.*, 1996].

Northern summer corresponds to the aphelion period: some papers refer this cloud belt as "aphelion cloud belt" [e.g., *Wolff et al.*, 1999], accordingly. It is also referred to as "equatorial cloud belt" [e.g., *James et al.*, 1996], "low-latitude cloud belt" [e.g., *Clancy et al.*, 1996], "tropical cloud belt" [e.g., *Pearl et al.*, 2001], and so on. In this thesis we mainly use the term "low-latitude cloud belt," or simply "the cloud belt."

While the low-latitude cloud belt has already been well-known as one of the most significant characteristics in northern summer, it is by *Slipher* [1962] that "Weather bands" and streaks of haze were first noted.

The most well-described but concise, and the latest summary of historical records of the cloud belt may be that by *Pearl et al.* [2001]. According to their summary and results, added to some reports of others', we can state on the cloud belt, as below;

- Ground-based visual and photographic observers did not report equatorial cloud bands for the oppositions of 1969 or 1975, although coverage of the northern spring and summer seasons was obtained. However, such bands were observed in the apparitions of 1978, 1980, 1982, and 1984, being most evident in 1980 and 1982.

- No tropical clouds were detected spectroscopically in 1969 at $L_s = 199°$ and $L_s = 200°$ by the Mariner 6 and 7 Infrared Spectrometer (IRS) experiments.

- Viking observations, however, showed them to be quite evident from 1976 to 1979 during the northern spring and summer seasons. According to the reanalyzed the Viking dataset by *Tamppari et al.* [2000], limited coverage in 1976 showed moderate tropical cloudiness present during the $L_s = 80°$-$125°$ season, apparently most concentrated in the general area of Tharsis. In 1978 the aphelion belt was significant during $L_s = 65°$-$80°$ but most prominent in the eastern hemisphere. Additionally, although no such bands were considered to be detected in southern spring or summer seasons [e.g., *Beish and Parker*, 1990], their reanalyzed Viking results showed some possibilities that there might have been some cloud bands in the southern tropics during the southern summer behind/within the veil of dust.

- More recent observations show the cloud bands between 10°S and 30°N quite consistently: at $L_s = 64°$ and $L_s = 94°$ in the opposition of 1992, for $L_s = 63°$-$135°$ in 1995, and $L_s = 45°$-$145°$ for 1996-1997 [*James et al.*, 1996; *Wolff et al.*, 1999].

- Ground-based observations showed the cloud bands between $L_s = 50°$ and $L_s = 120°$ in 1997, reaching a maximum at $L_s = 105°$ [*Parker et al.*, 1999].

- The most active period of the cloud belt is late spring to early summer and the cloud belt disappears by early autumn [*Wolff et al.*, 1999; *Tamppari et al.*, 2000].

However, the total mechanism about it as a distinct global and seasonal phenomenon was first given by *Clancy et al.* [1996], although contribution of the low-latitude northern summer cloud system to Mars atmospheric conditions had been recognized in some preceding papers.

The altitude of water ice cloud formation, as characterized by water vapor saturation, is a function of the atmospheric thermal structure. The present eccentricity of the orbit of Mars and the occurrence of aphelion during late northern spring radiatively leads to colder temperatures during northern spring and summer. Lower temperatures normally result in lower condensation level. Under the assumption of uniform water and dust vertical distributions, lower clouds simply have more water from which to form and condensation nuclei around which to do so, resulting in larger atmospheric opacity. In addition to these optimum saturation conditions, the $L_s = 60°$-$100°$ season corresponds to maximum upward advecting velocities in the solstice Hadley circulation. The formation of these clouds causes gravitational settling of ice particles in the rising branch of a cross-equatorial Hadley circulation, which then limits water to the northern hemisphere. The effectiveness of this trapping of water is amplified by the simultaneous scavenging of atmospheric dust, which keeps atmospheric temperatures low by removal of the

radiatively active dust. While aspects of this hypothesis are still being debated and investigated, orbital eccentricity is clearly a potent mechanism for possible climate change, past and present, since it suggests that the "wet" hemisphere will be the one with aphelic summer whenever the orbit is significantly elliptical.

There has been proposed another point of view. Several papers, including our preliminary report based on the ground-based observations in 1999, have suggested that the formation of the cloud belt is due to the combination of the midday remainder or extension of the activated morning clouds and the evening clouds [e.g., *Nakakushi et al.*, 1999a, b; *Akabane et al.*, 1997, 1999, 2002]. This idea may not necessarily contradict the hypothesis of *Clancy et al.* [1996]. Some additional discussions on this point are presented in Appendix C.

These, and other factors, indicate the importance of studies of the characteristics and structure of the low-latitude cloud belt in order to improve our understanding of it and its effects on global climate changes.

Chapter 3

Observations

This chapter describes the observations and the images used in the analyses in Part III and IV.

3.1 Sites, Telescopes and Filters

This study is based on blue-filtered images taken in 1997, 1999, and 2001. The telescopes we used were the 65cm refractor at Hida Observatory, Japan (in 1997 and 1999), the Steward Observatory Mt. Lemmon 60″ (in 1999) and Catalina 61″ (in 1999 and 2001) reflectors in Arizona, U.S.A. Image pixel sizes range from 0.08 to 0.18 arcsec. Table 3.1 gives the observational information.

3.2 Image Reduction

The first-order image reductions (bias subtraction and flat fielding) were performed using the astronomical standard Image Reduction and Analysis Facility (IRAF). IRAF is distributed by National Astronomy Observatories (NOAO), which is operated by the Association of Universities for Research in Astronomy, Inc., under contract to the National Science Foundation.

Blue light images were grouped into bins separated by no more than 5-min intervals to minimize the effects of Mars' rotation. In this thesis we refer to these as "image sets," which contain 6-30 images. We selected two to five comparatively sharp and clear images from each set and employed them for the analyses.

Table 3.1: Observational Equipment.

Site[a]	Teles.[b]	λ, Å	FWHM[c], Å	arcsec/pixel	pixel size, μm	f[d], m
H	65cm(R)	4362	156	0.09	9	20.7
L	60″(L)	4266	64	0.18	24	28.0
C1999	61″(L)	4400	100	0.14	14	20.9
C2001	61″(L)	4446	61	0.08	24	20.9

[a] H: Hida Obs., L: Mt. Lemmon site, and C1999, C2001: Catalina site in 1999 and 2001, respectively.
[b] R: refractor and L: reflector.
[c] Full width at half maximum.
[d] Equivalent focal length.

Within these directly image-handling processes (and some small calculations related) after the bias subtraction and the flat fielding with IRAF, the greater part of the analyses which directly handle the images was performed using Interactive Data Language (IDL).

Part II

Multiple Light Scattering

Chapter 4

Discrete Ordinate Method (DOM)

In this chapter we give a complete description on our estimation algorithm of the optical thickness of water ice clouds, which had not yet been given elsewhere.

In order to solve the radiative transfer equations and to derive the optical depths, we employed the modified discrete ordinate method (modified δ-M DOM). The DOM was introduced by *Chandrasekhar* [1960], developed by *Liou* [1973], and modified by many others [e.g., *Stamnes and Swanson*, 1981; *Stamnes and Dale*, 1981; *Stamnes et al.*, 1988, 2000]. The modified δ-M DOM we adopted here is fundamentally based on *Stamnes and Swanson* [1981] and *Stamnes and Dale* [1981] with phase functions approximated by means of the δ-M method [*Wiscombe*, 1977] under the assumption of a non-emitting plane parallel homogeneous (i.e., one-layered) atmosphere illuminated by direct sunlight. A prototype of our modified δ-M DOM is briefly described in *Akabane et al.* [1987]. The developed way described here is the essential basis of the analyses presented in *Nakakushi et al.* [2001a, 2002a]. *List of Symbols* is given in Appendix A.

4.1 Basic Equations

The equation of radiation transfer, the basic equation describing the diffuse intensity of solar radiation can be written as [*Chandrasekhar*, 1960]

$$\begin{aligned} \mu \frac{\partial I(\tau,\mu,\phi)}{\partial \tau} &= I(\tau,\mu,\phi) - \frac{1}{4\pi}\int_0^{2\pi}\int_{-1}^{+1} p(\mu,\phi;\mu',\phi') I(\tau,\mu',\phi') d\mu' d\phi' \\ &\quad -\frac{1}{4} F_0 p(\mu,\phi;-\mu_0,\phi_0) e^{-\tau/\mu_0}, \end{aligned} \tag{4.1}$$

where

I	diffuse intensity
τ	normal optical thickness
μ	cosine of the emergent angle
μ_0	cosine of the solar zenith angle
ϕ	emergent azimuth angle
ϕ_0	solar azimuth angle
p	scattering phase function
πF_0	solar incident flux.

The phase function p can be expanded in Legendre polynomials P_l consisting of $2n-1$ terms as

$$\begin{aligned} p(\cos\Theta) &= \sum_{l=0}^{2n-1} \varpi_l P_l(\cos\Theta) && (4.2a)\\ \varpi_l &= (2l+1)\chi_l \varpi_0 && (4.2b)\\ \chi_l &= \frac{1}{2}\int_0^{\pi} p(\cos\Theta) P_l(\cos\Theta) d\Theta, && (4.2c) \end{aligned}$$

where ϖ_0 is the single-scattering albedo. The phase function p is normalized so that

$$\frac{1}{4\pi}\int_{4\pi} p(\Omega) d\Omega = \varpi_0. \tag{4.3}$$

From the spherical geometry, the relationships between the scattering angle Θ, the cosine of zenith angles μ, μ', and the azimuth angles ϕ, ϕ' can be derived:

$$\begin{aligned} \cos\Theta &= \cos\theta\cos\theta' + \sin\theta\sin\theta'\cos(\phi-\phi')\\ &= \mu\mu' + (1-\mu^2)^{\frac{1}{2}}(1-\mu'^2)^{\frac{1}{2}}\cos(\phi-\phi'). \end{aligned} \tag{4.4}$$

Hence, by the addition theorem of spherical harmonics, i.e.,

$$\begin{aligned} P_l(\cos\Theta) &= P_l(\cos\theta)P_l(\cos\theta') + 2\sum_{m=1}^{l}\frac{(l-m)!}{(l+m)!}P_l^m(\cos\theta)P_l^m(\cos\theta')\cos m(\phi-\phi')\\ &= P_l(\mu)P_l(\mu') + 2\sum_{m=1}^{l}\frac{(l-m)!}{(l+m)!}P_l^m(\mu)P_l^m(\mu')\cos m(\phi-\phi'), \end{aligned} \tag{4.5}$$

the phase function in Eq. (4.1) can be expanded in a cosine series in azimuth. For the phase function in the integral,

$$\begin{aligned} p(\mu,\phi;\mu',\phi') &= \sum_{l=0}^{2n-1}(2-\delta_{0,m})\sum_{m=0}^{l}\varpi_l^m P_l^m(\mu)P_l^m(\mu')\cos m(\phi-\phi')\\ &= \sum_{m=0}^{2n-1}(2-\delta_{0,m})\sum_{l=m}^{2n-1}\varpi_l^m P_l^m(\mu)P_l^m(\mu')\cos m(\phi-\phi')\\ l &= m,\ldots,2n-1, \quad 0\leqslant m\leqslant 2n-1 \end{aligned} \tag{4.6}$$

with

$$\varpi_l^m = \varpi_l\frac{(l-m)!}{(l+m)!}, \quad \delta_{0,m} = \begin{cases} 1, & \text{if } m=0\\ 0, & \text{otherwise} \end{cases}, \tag{4.7}$$

where $P_l^m(\mu)$ is the associated Legendre polynomial. For the source term (the solar incident beam),

$$\begin{aligned} p(\mu,\phi;-\mu_0,\phi_0) &= \sum_{m=0}^{2n-1}(2-\delta_{0,m})\sum_{l=m}^{2n-l}\varpi_l^m P_l^m(\mu)P_l^m(-\mu_0)\cos m(\phi_0-\phi)\\ l &= m,\ldots,2n-1, \quad 0\leqslant m\leqslant 2n-1. \end{aligned} \tag{4.8}$$

Expansion of the intensity in a $2n-1$-term Fourier cosine series in azimuth can be represented in the relevant forms

$$I(\tau,\mu,\phi)=\begin{cases}\sum_{m=0}^{2n-1} I^m(\tau,\mu)\cos m(\phi-\phi') & \text{, in the integral}\\ \sum_{m=0}^{2n-1} I^m(\tau,\mu)\cos m(\phi-\phi_0) & \text{, for the other terms.}\end{cases} \tag{4.9}$$

Thus, inhomogeneous differential equation for a given m is obtained as

$$\begin{aligned}\mu\frac{\partial I^m(\tau,\mu)}{\partial\tau} &= I^m(\tau,\mu)-\frac{1}{2}\sum_{l=m}^{2n-1}\varpi_l^m P_l^m(\mu)\int_{-1}^{+1}P_l^m(\mu')I^m(\tau,\mu')d\mu'\\ &\quad -\frac{1}{4}F_0(2-\delta_{0,m})\sum_{l=m}^{2n-1}\varpi_l^m(-1)^{l+m}P_l^m(\mu)P_l^m(\mu_0)e^{-\tau/\mu_0},\\ &\quad m=0,1,2,\ldots,2n-1.\end{aligned} \tag{4.10}$$

Application of the Gauss-Legendre quadrature to the integral in Eq. (4.10);

$$\int_{-1}^{+1}P_l^m(\mu')I^m(\tau,\mu')d\mu'\simeq\sum_{\substack{j=-n\\ j\neq 0}}^{n}a_jP_l^m(\mu_j)I^m(\tau,\mu_j) \tag{4.11a}$$

and

$$P_{2n}(\mu_j)=0, \tag{4.11b}$$

where a_j's are the weights of Gauss formula (see also Table 4.1);

$$a_j=\frac{1}{P'_{2n}(\mu_j)}\int_{-1}^{+1}\frac{P_{2n}(\mu)}{\mu-\mu_j}d\mu=\frac{(1-{\mu_j}^2)}{2\{nP_{2n+1}(\mu_j)\}^2}. \tag{4.12}$$

From the definition, the quadrature weights a_j are independent on the function in Eq. (4.11a) (see Table 4.1). From Eqs. (4.11a)-(4.12) and (4.10), one obtains for a given μ_i,

$$\begin{aligned}\mu_i\frac{\partial I^m(\tau,\mu_i)}{\partial\tau} &= I^m(\tau,\mu_i)-\frac{1}{2}\sum_{l=m}^{2n-1}\varpi_l^m P_l^m(\mu_i)\sum_{\substack{j=-n\\ j\neq 0}}^{n}a_jP_l^m(\mu_j)I^m(\tau,\mu_j)\\ &\quad -\frac{1}{4}F_0(2-\delta_{0,m})\sum_{l=m}^{2n-1}\varpi_l^m(-1)^{l+m}P_l^m(\mu_i)P_l^m(\mu_0)e^{-\tau/\mu_0}\\ &\quad i=-n,\ldots,+n,\quad i\neq 0,\\ &\quad j=-n,\ldots,+n,\quad j\neq 0,\quad 0\leqslant m\leqslant 2n-1.\end{aligned} \tag{4.13}$$

Only the 0th intensity component I^0, i.e., the azimuth-independent component, contributes to the flux.

Table 4.1: Numerical Quantities for Gauss-Legendre Quadrature.

j	μ_j	a_j
$(-)1$	$(-)0.0198550718$	0.0506142681
$(-)2$	$(-)0.1016667613$	0.1111905172
$(-)3$	$(-)0.2372337950$	0.1568533229
$(-)4$	$(-)0.4082826788$	0.1813418917
$(-)5$	$(-)0.5917173212$	0.1813418917
$(-)6$	$(-)0.7627662050$	0.1568533229
$(-)7$	$(-)0.8983332387$	0.1111905172
$(-)8$	$(-)0.9801449282$	0.0506142681

Note: $\mu_{-j} = -\mu_j$, $a_{-j} = a_j$.

4.2 Discrete Solution

4.2.1 Homogeneous Solution: Matrix Formation, Eigenvalues and Eigenfunctions (W-Functions)

For the mth azimuthal component, omitting the source term, Eq. (4.13) become as

$$\begin{aligned}
\frac{dI_i^m}{d\tau} &= \frac{1}{\mu_i} I_i^m - \frac{1}{\mu_i} \sum_{\substack{j=-n \\ j\neq 0}}^{n} \frac{1}{2} \sum_{l=m}^{2n-1} a_j \varpi_l^m P_l^m(\mu_i) P_l^m(\mu_j) I_j^m \\
&= \frac{1}{\mu_i} I_i^m - \sum_{j=1}^{n} \frac{1}{\mu_i} (C_{i,-j}^m I_{-j} + C_{ij}^m I_j^m) \\
&= \begin{cases} -\left\{ \displaystyle\sum_{j=1}^{n} \frac{1}{\mu_i} (C_{ij}^m - \delta_{ij}) I_j^m + \sum_{j=1}^{n} \frac{1}{\mu_i} C_{i,-j}^m I_{-j} \right\} & \text{for positive } \mu_i \\ -\left\{ \displaystyle\sum_{j=1}^{n} \frac{1}{\mu_i} C_{ij}^m I_j^m + \sum_{j=1}^{n} \frac{1}{\mu_i} (C_{i,-j}^m - \delta_{i,-j}) I_{-j}^m \right\} & \text{for negative } \mu_i, \end{cases}
\end{aligned} \tag{4.14}$$

where $I_i^m = I^m(\tau, \mu_i)$ and

$$C_{ij}^m = \frac{1}{2} \sum_{l=m}^{2n-1} \varpi_l^m P_l^m(\mu_i) P_l^m(\mu_j). \tag{4.15}$$

Below we confine the discussion within the mth component, so that we omit the superscript m.

Here we define the matrices $\boldsymbol{\alpha}$ and $\boldsymbol{\beta}$ so that

$$\begin{aligned}
\alpha_{ij} &= (C_{ij} - \delta_{ij})/\mu_i \\
&= (C_{-i,-j} - \delta_{ij})/\mu_i \qquad (4.16a) \\
\beta_{ij} &= C_{-i,j}/\mu_i \\
&= C_{i,-j}/\mu_i \quad . \qquad (4.16b)
\end{aligned}$$

Using these notations, the system of the homogeneous differential equations for the mth azimuth component [Eq. (4.14)] can be expressed in a matrix form:

$$\begin{bmatrix} \dfrac{d\boldsymbol{I}^-}{d\tau} \\ \\ \dfrac{d\boldsymbol{I}^+}{d\tau} \end{bmatrix} = \begin{bmatrix} \boldsymbol{\alpha} & \boldsymbol{\beta} \\ \\ -\boldsymbol{\beta} & -\boldsymbol{\alpha} \end{bmatrix} \begin{bmatrix} \boldsymbol{I}^- \\ \\ \boldsymbol{I}^+ \end{bmatrix}. \tag{4.17}$$

Seeking the homogeneous solutions in the form of $\boldsymbol{I}^{\pm} = \boldsymbol{g}^{\pm} e^{-k\tau}$ leads to

$$\begin{bmatrix} -\boldsymbol{\alpha} & -\boldsymbol{\beta} \\ \boldsymbol{\beta} & \boldsymbol{\alpha} \end{bmatrix} \begin{bmatrix} \boldsymbol{g}^- \\ \boldsymbol{g}^+ \end{bmatrix} = k \begin{bmatrix} \boldsymbol{g}^- \\ \boldsymbol{g}^+ \end{bmatrix}, \tag{4.18}$$

where k is the eigenvalue and $\boldsymbol{g}^{\pm}$ are the eigenvectors. This can be separated into

$$-\boldsymbol{\alpha}\boldsymbol{g}^- - \boldsymbol{\beta}\boldsymbol{g}^+ = k\boldsymbol{g}^- \tag{4.19a}$$
$$\boldsymbol{\beta}\boldsymbol{g}^- + \boldsymbol{\alpha}\boldsymbol{g}^+ = k\boldsymbol{g}^+. \tag{4.19b}$$

Because of the symmetric form of the matrix in Eq. (4.17), the eigenvalues occurs in pairs $\pm k$ [*Chandrasekhar*, 1960]. To reduce the order and to simplify, adding and subtracting Eqs. (4.19a) and (4.19b) we have

$$-(\boldsymbol{\alpha}+\boldsymbol{\beta})(\boldsymbol{g}^- + \boldsymbol{g}^+) = k(\boldsymbol{g}^- - \boldsymbol{g}^+) \tag{4.20a}$$
$$(-\boldsymbol{\alpha}+\boldsymbol{\beta})(\boldsymbol{g}^- - \boldsymbol{g}^+) = k(\boldsymbol{g}^- + \boldsymbol{g}^+). \tag{4.20b}$$

Substituting Eq. (4.20a) into (4.20b) yields

$$(\boldsymbol{\alpha}-\boldsymbol{\beta})(\boldsymbol{\alpha}+\boldsymbol{\beta})(\boldsymbol{g}^+ + \boldsymbol{g}^-) = k^2(\boldsymbol{g}^- + \boldsymbol{g}^+). \tag{4.21}$$

From Eq. (4.21) we can determine the eigenvalues and the eigenvectors of the reduced system, i.e., k^2 and $(\boldsymbol{g}^+ + \boldsymbol{g}^-)$. Substituting these k's ($k > 0$) to Eq. (4.20a), one can obtain $(\boldsymbol{g}^+ - \boldsymbol{g}^-)$. Subtracting and adding $(\boldsymbol{g}^+ + \boldsymbol{g}^-)$ and $(\boldsymbol{g}^+ - \boldsymbol{g}^-)$ yield the eigenvectors of the original system $(\boldsymbol{g}^{\pm})$.

W-function We can represent the solution of the eigenvalue problem [Eq. (4.18)] by using eigenfunctions $W_j^m(\mu_i)$

$$\boldsymbol{W} = \begin{bmatrix} \boldsymbol{g}^+ & \boldsymbol{g}^- \\ \boldsymbol{g}^- & \boldsymbol{g}^+ \end{bmatrix}, \tag{4.22}$$

where the components $W_{ij} \equiv W_j^m(\mu_i)$ and eigenvalues k_j^m satisfy symmetry relations:

$$W_j^m(\mu_i) = W_{-j}^m(-\mu_i) \tag{4.23a}$$
$$W_{-j}^m(\mu_i) = W_j^m(-\mu_i) \tag{4.23b}$$
$$-k_{-j}^m = k_j^m, \tag{4.23c}$$

In this form [Eq. (4.22)], the subscripts for its rows run from $-i$ to i (up to down), for columns from $-j$ to j (left to right).

4.2.2 Particular Solution: Z-Function

General solutions for the mth azimuthal and the ith discrete component can be formulated as:

$$I^m(\tau,\mu_i) = \left[\sum_{\substack{j=-n\\ j\neq 0}}^{n} L_j^m W_j^m(\mu_i) e^{-k_j^m \tau}\right] + Z_0^m(\mu_i) e^{-\tau/\mu_0}, \tag{4.24}$$

where $Z_0^m(\mu_i)e^{-\tau/\mu_0} \equiv I_p^m(\tau,\mu_i)$ is the particular solution for a parallel beam of sunlight incident on a non-emitting atmosphere since $I(\tau,\mu_i)$ describes the scattered radiation only.

The $Z_0^m(\mu_i)$'s are determined from the following system of linear algebraic equations[1]:

$$\sum_{\substack{j=-n\\ j\neq 0}}^{n} \left[\left(1+\frac{\mu_i}{\mu_0}\right)\delta_{ij} - C_{ij}^m\right] Z_0^m(\mu_i) = \frac{F_0}{4}(2-\delta_{0,m})\left[\sum_{l=m}^{2n-1} \varpi_l^m (-1)^{l+m} P_l^m(\mu_i) P_l^m(\mu_0)\right]. \tag{4.25}$$

4.3 General Solution

The formal solution to Eq. (4.1) is easily obtained as [*Chandrasekhar*, 1960]

$$I(\tau,+\mu) = I(\tau_{\rm N},+\mu)e^{-(\tau_{\rm N}-\tau)/\mu} + \int_{\tau}^{\tau_{\rm N}} J(\tau,+\mu)e^{-(t-\tau)/\mu}\frac{dt}{\mu}, \tag{4.26}$$

where $\tau_{\rm N}$ represents the ground surface, and

$$J(\tau,\mu) = \frac{1}{4\pi}\int_0^{2\pi}\int_{-1}^{+1} p(\mu,\phi;\mu',\phi')I(\tau,\mu',\phi')d\mu' d\phi' - \frac{1}{4}F_0 p(\mu,\phi;-\mu_0,\phi_0)e^{-\tau/\mu_0}. \tag{4.27}$$

In addition to Eq. (4.26), one can also easily obtain the formal solution $I(\tau,-\mu)$ (i.e., downward). However, it is beyond the scope of this study.

Considering the case of a parallel incident beam, it follows that the discrete ordinate approximation to Eq. (4.27) is [see Eq. (4.8)]

$$J^m(\tau,\mu) = \frac{1}{2}\sum_{l=m}^{2n-1}\varpi_l^m P_l^m(\mu)\sum_{\substack{j=-n\\ j\neq 0}}^{n} a_j P_l^m(\mu_j) I^m(\tau,\mu_j) + \frac{1}{4}F_0(2-\delta_{0,m})\sum_{l=m}^{2n-1}\varpi_l^m(-1)^{l+m}P_l^m(\mu)P_l^m(\mu_0)e^{-\tau/\mu_0}. \tag{4.28}$$

[1]The right-hand side of this equation corresponds to X_0 in Eqs. (19) and (20) of *Stamnes and Swanson* [1981], although the manner follows that of *Stamnes and Dale* [1981]. That is,

$$X_0^m(\mu_i) = \frac{F_0}{4}(2-\delta_{0,m})\left[\sum_{l=m}^{2n-1}\varpi_l^m(-1)^{l+m}P_l^m(\mu_i)P_l^m(\mu_0)\right].$$

Using this expression to Eq. (4.13) yields

$$J^m(\tau,\mu_i) = I^m(\tau,\mu_i) - \mu_i \frac{\partial I^m(\tau,\mu_i)}{\partial \tau}. \tag{4.29}$$

Substituting the discrete ordinate solution [Eq. (4.24)] for $I^m(\tau,\mu_i)$ in Eq. (4.29) one readily finds

$$J^m(\tau,\mu_i) = \left[\sum_{\substack{j=-n\\ j\neq 0}}^{n} (1+k_j^m\mu_i) L_j^m W_j^m(\mu_i) e^{-k_j^m\tau}\right] + \left(1+\frac{\mu_i}{\mu_0}\right) Z_0^m(\mu_i) e^{-\tau/\mu_0}, \tag{4.30}$$

which can be extended to an arbitrary angle (replacing μ_i for μ):

$$J^m(\tau,\mu) = \left[\sum_{\substack{j=-n\\ j\neq 0}}^{n} (1+k_j^m\mu) L_j^m W_j^m(\mu) e^{-k_j^m\tau}\right] + \left(1+\frac{\mu}{\mu_0}\right) Z_0^m(\mu) e^{-\tau/\mu_0}. \tag{4.31}$$

Using this expression in the formal solution Eq. (4.26) yields the general solution for any μ as [*Stamnes and Dale*, 1981]

$$I^m(\tau,+\mu) = \sum_{\substack{j=-n\\ j\neq 0}}^{n} L_j^m W_j^m(\mu)\left[e^{-k_j^m\tau} - e^{\{-k_j^m\tau_{\rm N}+(\tau_{\rm N}-\tau)/\mu\}}\right] + Z_0^m(\mu)\left[e^{-\tau/\mu_0} - e^{\{-\tau_{\rm N}/\mu_0+(\tau_{\rm N}-\tau)/\mu\}}\right], \tag{4.32}$$

where $W_i^m(\mu)$ and $Z_0^m(\mu)$ are determined from the basic equations above. To do so, combining Eqs. (4.28) and (4.31), and substituting Eq. (4.24), one can write as

$$\begin{aligned} &\frac{1}{2}\sum_{l=m}^{2n-1} \varpi_l^m P_l^m(\mu) \sum_{\substack{j=-n\\ j\neq 0}}^{n} a_j P_l^m(\mu_j) \left[\sum_{\substack{j'=-n\\ j'\neq 0}}^{n} L_{j'}^m W_{j'}^m(\mu_j) e^{-k_{j'}^m\tau} + Z_0^m(\mu_j) e^{-\tau/\mu_0}\right] \\ &\quad + \frac{1}{4} F_0 (2-\delta_{0,m}) \sum_{l=m}^{2n-1} \varpi_l^m (-1)^{l+m} P_l^m(\mu) P_l^m(\mu_0) e^{-\tau/\mu_0} \\ &= \left[\sum_{\substack{j=-n\\ j\neq 0}}^{n} (1+k_j^m\mu) L_j^m W_j^m(\mu) e^{-k_j^m\tau}\right] + \left(1+\frac{\mu}{\mu_0}\right) Z_0^m(\mu) e^{-\tau/\mu_0}, \end{aligned} \tag{4.33}$$

which comes to

$$\sum_{\substack{i=-n\\ i\neq 0}}^{n}\left[(1+k_i^m\mu)W_i^m(\mu)-\frac{1}{2}\sum_{l=m}^{2n-1}\varpi_l^m P_l^m(\mu)\sum_{\substack{j=-n\\ j\neq 0}}^{n}a_j P_l^m(\mu_j)W_i^m(\mu_j)\right]L_i^m e^{-k_i^m\tau}$$
$$+\left[\left(1+\frac{\mu}{\mu_0}\right)Z_0^m(\mu)-\left\{\frac{1}{2}\sum_{l=m}^{2n-1}\varpi_l^m P_l^m(\mu)Z_0^m(\mu_j)\right.\right.$$
$$\left.\left.+\frac{1}{4}F_0(2-\delta_{0,m})\sum_{l=m}^{2n-1}\varpi_l^m(-1)^{l+m}P_l^m(\mu)P_l^m(\mu_0)\right\}\right]e^{-\tau/\mu_0}$$
$$=0. \quad (4.34)$$

Thus we can obtain

$$W_i^m(\mu) = \frac{1}{1+k_i^m\mu}\sum_{l=m}^{2n-1}\varpi_l^m P_l^m(\mu)\left[\frac{1}{2}\sum_{\substack{j=-n\\ j\neq 0}}^{n}a_j P_l^m(\mu_j)W_i^m(\mu_j)\right] \quad (4.35)$$

and

$$Z_0^m(\mu) = \frac{1}{1+\mu/\mu_0}\sum_{l=m}^{2n-1}\varpi_l^m P_l^m(\mu)$$
$$\times\left[\frac{1}{2}\sum_{\substack{j=-n\\ j\neq 0}}^{n}a_j P_l^m(\mu_j)Z_0^m(\mu_j)+\frac{F_0}{4}(-1)^{l+m}(2-\delta_{0,m})P_l^m(\mu_0)\right]. \quad (4.36)$$

Chapter 5

Boundary Conditions

5.1 Boundary Conditions

Here we derive the boundary conditions to determine the integral constants L_j^m in some detail.

5.1.1 Upper Boundary ($\tau = 0$)

The upper boundary layer must admit this condition:

$$I^m(0, -\mu_i) = 0 \quad \text{for} \quad i = 1, \ldots, n \text{ and } m = 1, \ldots, 2n-1, \tag{5.1}$$

i.e., no downward diffuse intensities at the top of the scattering layer. Substituting $\tau = 0$ into Eq. (4.24), this becomes

$$\sum_{\substack{j=-n \\ j\neq 0}}^{n} L_j^m W_j^m(-\mu_i) + Z_0^m(-\mu_i) = 0, \tag{5.2}$$

that is,

$$\sum_{\substack{j=-n \\ j\neq 0}}^{n} L_j^m W_j^m(-\mu_i) = -Z_0^m(-\mu_i) \quad \text{for} \quad i = 0, \ldots, n. \tag{5.3}$$

5.1.2 Lower Boundary: Ground Surface ($\tau = \tau_{\mathrm{N}}$)

Here we consider the downward diffused intensity at the ground level, $I(\tau_{\mathrm{N}}, -\mu', \phi')$, scattered by the ground surface. The reflected intensity for any emergent angles (μ and ϕ) is denoted by $I_{\mathrm{ref}}(\tau_{\mathrm{N}}, \mu, \phi)$. Considering the solar incident flux πF_0 with the incident angle θ_0 yields to [*Liou*, 1980]

$$I_{\mathrm{ref}}(\tau_{\mathrm{N}}, \mu, \phi) = \frac{1}{\pi} \int_0^{2\pi} \int_0^{+1} R(\mu, \phi; \mu', \phi') I(\tau_{\mathrm{N}}, -\mu', \phi') \mu' d\mu' d\phi' + F_0 \mu_0 R(\mu, \phi; -\mu_0, \phi_0) e^{-\tau_{\mathrm{N}}/\mu_0}, \tag{5.4}$$

where $R(\mu, \phi; \mu', \phi')$ is the reflection function. Because only the azimuth-independent component, i.e., $I^{m=0}$, contributes to the flux, the lower boundary conditions can be expressed as

$$I^m(\tau_{\rm N}, \mu) = 0 \quad \text{for } m \neq 0 \tag{5.5}$$

$$I^0(\tau_{\rm N}, \mu) = \frac{1}{\pi}\int_0^{2\pi}\int_0^{+1} R(\mu, \phi; \mu', \phi') I^0(\tau_{\rm N}, -\mu') \mu' d\mu' d\phi' + F_0 \mu_0 R(\mu, \phi; -\mu_0, \phi_0) e^{-\tau_{\rm N}/\mu_0}$$
$$\text{for } m = 0 \tag{5.6}$$

We assumed that the reflection function R can be expressed in the Minnaert's law,

$$\begin{aligned} R(\mu, \phi; \mu', \phi') &= R(\mu, \mu') \\ &= A_{\rm M} (\mu\mu')^{k_{\rm M}-1}, \end{aligned} \tag{5.7}$$

so that we can carry out the integral for ϕ' in Eq. (5.6),

$$I^0(\tau_{\rm N}, \mu) = A_{\rm M}\left[2\int_0^{+1} I^0(\tau_{\rm N}, -\mu') \mu'^{k_{\rm M}-1} \mu^{k_{\rm M}} d\mu' + F_0 \mu_0^{k_{\rm M}} \mu^{k_{\rm M}-1} e^{-\tau_{\rm N}/\mu_0}\right]. \tag{5.8}$$

We apply the Gauss-Legendre quadrature to Eq. (5.8), which leads to

$$I^0(\tau_{\rm N}, \mu) = A_{\rm M}\left[2\sum_{i'=1}^{n} a_{i'} \mu'^{k_{\rm M}}_{i'} \mu^{k_{\rm M}-1} I^0(\tau_{\rm N}, -\mu'_{i'}) + F_0 \mu_0^{k_{\rm M}} \mu^{k_{\rm M}-1} e^{-\tau_{\rm N}/\mu_0}\right], \tag{5.9}$$

where

$$I^0(\tau_{\rm N}, -\mu_{i'}) = \sum_{\substack{j=-n \\ j\neq 0}}^{n} L_j^0 W_j^0(-\mu_{i'}) e^{-k_j^0 \tau_{\rm N}} + Z_0^0(-\mu_{i'}) e^{-\tau_{\rm N}/\mu_0}. \tag{5.10}$$

Note that only the upward components ($\mu_{i'} > 0$) contribute to the summation in Eq. (5.9). one can then write down the lower boundary relation for ith discrete component:

$$\begin{aligned} I^0(\tau_{\rm N}, \mu_i) &= \sum_{\substack{j=-n \\ j\neq 0}}^{n} L_j^0 W_j^0(-\mu_i) e^{-k_j^0 \tau_{\rm N}} + Z_0^0(-\mu_i) e^{-\tau_{\rm N}/\mu_0} \\ &= A_{\rm M}\left[2\sum_{i'=1}^{n} a_{i'} \mu_{i'}^{k_{\rm M}} \mu_i^{k_{\rm M}-1} I^0(\tau_{\rm N}, -\mu_{i'}) + F_0 \mu_0^{k_{\rm M}} \mu_i^{k_{\rm M}-1} e^{-\tau_{\rm N}/\mu_0}\right]. \end{aligned} \tag{5.11}$$

Substituting Eq. (5.10) into Eq. (5.11) leads to

$$\begin{aligned} &\sum_{\substack{j=-n \\ j\neq 0}}^{n} L_j^0 W_j^0(-\mu_i) e^{-k_j^0 \tau_{\rm N}} + Z_0^0(-\mu_i) e^{-\tau_{\rm N}/\mu_0} \\ &\qquad = A_{\rm M}\left[2\sum_{i'=1}^{n} a_{i'} \mu_{i'}^{k_{\rm M}} \mu_i^{k_{\rm M}-1} \left\{\sum_j L_j^0 W_j^0(-\mu_{i'}) e^{-k_j^0 \tau_{\rm N}} + Z_0^0(-\mu_{i'}) e^{-\tau_{\rm N}/\mu_0}\right\}\right. \\ &\qquad\qquad \left. + F_0 \mu_0^{k_{\rm M}} \mu_i^{k_{\rm M}-1} e^{-\tau_{\rm N}/\mu_0}\right]. \end{aligned} \tag{5.12}$$

After manipulating about L_j^0, one can obtain

$$\sum_j L_j^0 \left\{ W_j^0(\mu_i) - 2A_{\rm M} \sum_{i'} a_{i'} \mu_{i'}^{k_{\rm M}} \mu_i^{k_{\rm M}-1} W_j^0(-\mu_{i'}) \right\} e^{-k_j^0 \tau_{\rm N}}$$
$$= - \left\{ Z_0^0(\mu_i) - 2A_{\rm M} \sum_{i'} a_{i'} \mu_{i'}^{k_{\rm M}} \mu_i^{k_{\rm M}-1} Z_0^0(-\mu_{i'}) - A_{\rm M} F_0 \mu_0^{k_{\rm M}} \mu_i^{k_{\rm M}-1} \right\} e^{-\tau_{\rm N}/\mu_0}. \quad (5.13)$$

This can be expressed as below;

$$\sum_{\substack{j=-n \\ j\neq 0}}^{n} L_j^0 \beta_j^0(\mu_i) = -\epsilon^0(\mu_i), \quad (5.14)$$

where

$$\beta_j^0(\mu_i) = \left\{ W_j^0(\mu_i) - 2A_{\rm M} \sum_{i'} a_{i'} \mu_{i'}^{k_{\rm M}} \mu_i^{k_{\rm M}-1} W_j^0(-\mu_{i'}) \right\} e^{-k_j^0 \tau_{\rm N}} \quad (5.15)$$

and

$$\epsilon^0(\mu_i) = \left\{ Z_0^0(\mu_i) - 2A_{\rm M} \sum_{i'} a_{i'} \mu_{i'}^{k_{\rm M}} \mu_i^{k_{\rm M}-1} Z_0^0(-\mu_{i'}) - A_{\rm M} F_0 \mu_0^{k_{\rm M}} \mu_i^{k_{\rm M}-1} \right\} e^{-\tau_{\rm N}/\mu_0}. \quad (5.16)$$

The Minnaert albedo $A_{\rm M}$ is not exactly "constant" [e.g., *Hapke*, 1981], so that we assumed it to be

$$A_{\rm M} = A_n \Phi(\alpha). \quad (5.17)$$

A_n, α, and $\Phi(\alpha)$ are the ground normal albedo, the phase angle (the sun - Mars - Earth), and the ground phase function, respectively. The phase function is normalized: $\Phi(\alpha = 0) = 1$.

5.2 Determining Equations for the Coefficients

Firstly we derive the determining equations for the $m = 0$ component. Hereafter we omit the superscript 0 (zero) for a while.

Adding Eqs. (5.3) and (5.14) yields

$$\sum_{\substack{j=-n \\ j\neq 0}}^{n} L_j \left\{ W_j(-\mu_i) + \beta_j(\mu_i) \right\} = - \left\{ Z_0(-\mu_i) + \epsilon(\mu_i) \right\}. \quad (5.18)$$

The left-hand side of this equation is manipulated as

$$\begin{aligned}
&\sum_{\substack{j=-n\\ j\neq 0}}^{n} L_j \left\{ W_j(-\mu_i) + W_j(\mu_i)e^{-k_j\tau_{\rm N}} - 2A_{\rm M}\sum_{i'} a_{i'}\mu_{i'}^{k_{\rm M}}\mu_i^{k_{\rm M}-1}W_j(-\mu_{i'})e^{-k_j\tau_{\rm N}} \right\} \\
&= \sum_{j=-n}^{-1} L_j \left\{ W_j(-\mu_i) + W_j(\mu_i)e^{-k_j\tau_{\rm N}} - 2A_{\rm M}\sum_{i'} a_{i'}\mu_{i'}^{k_{\rm M}}\mu_i^{k_{\rm M}-1}W_j(-\mu_{i'})e^{-k_j\tau_{\rm N}} \right\} \\
&\quad + \sum_{j=1}^{n} L_j \left\{ W_j(-\mu_i) + W_j(\mu_i)e^{-k_j\tau_{\rm N}} - 2A_{\rm M}\sum_{i'} a_{i'}\mu_{i'}^{k_{\rm M}}\mu_i^{k_{\rm M}-1}W_j(-\mu_{i'})e^{-k_j\tau_{\rm N}} \right\} \\
&= \sum_{j=1}^{n} \left[L_{-j} \left\{ W_{-j}(-\mu_i) + W_{-j}(\mu_i)e^{-k_{-j}\tau_{\rm N}} - 2A_{\rm M}\sum_{i'} a_{i'}\mu_{i'}^{k_{\rm M}}\mu_i^{k_{\rm M}-1}W_{-j}(-\mu_{i'})e^{-k_{-j}\tau_{\rm N}} \right\} \right. \\
&\quad \left. + L_j \left\{ W_j(-\mu_i) + W_j(\mu_i)e^{-k_j\tau_{\rm N}} - 2A_{\rm M}\sum_{i'} a_{i'}\mu_{i'}^{k_{\rm M}}\mu_i^{k_{\rm M}-1}W_j(-\mu_{i'})e^{-k_j\tau_{\rm N}} \right\} \right].
\end{aligned}$$

Using the symmetry relations of W_j and k_j [Eqs. (4.23b)-(4.23c)] one can transform Eq. (5.18) as

$$\begin{aligned}
&\sum_{j=1}^{n} \left[L_{-j} \left\{ W_j(\mu_i) + W_j(-\mu_i)e^{k_j\tau_{\rm N}} - 2A_{\rm M}\sum_{i'} a_{i'}\mu_{i'}^{k_{\rm M}}\mu_i^{k_{\rm M}-1}W_j(\mu_{i'})e^{k_j\tau_{\rm N}} \right\} \right. \\
&\qquad \left. + L_j \left\{ W_j(-\mu_i) + W_j(\mu_i)e^{-k_j\tau_{\rm N}} - 2A_{\rm M}\sum_{i'} a_{i'}\mu_{i'}^{k_{\rm M}}\mu_i^{k_{\rm M}-1}W_j(-\mu_{i'})e^{-k_j\tau_{\rm N}} \right\} \right] \\
&\qquad\qquad = -\left\{ Z_0(-\mu_i) + \epsilon(\mu_i) \right\}. \qquad (5.19)
\end{aligned}$$

This can be reformed as

$$\sum_{j=1}^{n} \left[M_j \left\{ W_j(-\mu_i) + W_j(\mu_i)e^{-k_j\tau_{\rm N}} - A_{1j} \right\} + N_j A_{2j} \right] = -\left\{ Z_0(-\mu_i) + \epsilon(\mu_i) \right\}, \qquad (5.20)$$

where

$$\begin{aligned}
M_j &= L_j + L_{-j}e^{k_j\tau_{\rm N}} \\
N_j &= L_j - L_{-j}e^{k_j\tau_{\rm N}}
\end{aligned}$$

and

$$\begin{aligned}
A_{1j} &= A_{\rm M}\sum_{i'} a_{i'}\mu_{i'}^{k_{\rm M}}\mu_i^{k_{\rm M}-1} \left\{ W_j(\mu_{i'}) + W_j(-\mu_{i'})e^{-k_j\tau_{\rm N}} \right\} \\
A_{2j} &= A_{\rm M}\sum_{i'} a_{i'}\mu_{i'}^{k_{\rm M}}\mu_i^{k_{\rm M}-1} \left\{ W_j(\mu_{i'}) - W_j(-\mu_{i'})e^{-k_j\tau_{\rm N}} \right\}.
\end{aligned}$$

Subtracting Eqs. (5.3) and (5.14) yields

$$\sum_{\substack{j=-n\\ j\neq 0}}^{n} L_j \left\{ W_j(-\mu_i) - \beta_j(\mu_i) \right\} = -\left\{ Z_0(-\mu_i) - \epsilon(\mu_i) \right\}. \qquad (5.21)$$

Similar manipulations yields

$$\sum_{j=1}^{n}\left[M_j A_{1j} + N_j\left\{W_j(-\mu_i) - W_j(\mu_i)e^{-k_j\tau_{\rm N}} - A_{2j}\right\}\right] = -\left\{Z_0(-\mu_i) - \epsilon(\mu_i)\right\}. \tag{5.22}$$

After the coefficients M_j and N_j is calculated from Eqs. (5.20) and (5.22), one can obtain L_j and L_{-j} from

$$L_j = \frac{1}{2}(M_j + N_j) \tag{5.23a}$$

$$L_{-j} = \frac{1}{2}(M_j - N_j)e^{-k_j\tau_{\rm N}}. \tag{5.23b}$$

The above discussion is confined within the $m = 0$ component. These expressions for $m = 0$ can be formally applied to the $m \neq 0$ components by treating $A_{\rm M}$ as zero.

We can now express the equations to determine the coefficients L_j^m (and L_{-j}^m) as below:

$$\sum_{j=1}^{n}\left[M_j^m\left\{W_j^m(-\mu_i) + W_j^m(\mu_i)e^{-k_j^m\tau_{\rm N}} - A_{1j}^m\right\} + N_j^m A_{2j}^m\right] = -\left\{Z_0^m(-\mu_i) + \epsilon^m(\mu_i)\right\} \tag{5.24a}$$

$$\sum_{j=1}^{n}\left[M_j^m A_{1j}^m + N_j^m\left\{W_j^m(-\mu_i) - W_j^m(\mu_i)e^{-k_j^m\tau_{\rm N}} - A_{2j}^m\right\}\right] = -\left\{Z_0^m(-\mu_i) - \epsilon^m(\mu_i)\right\} \tag{5.24b}$$

$$\epsilon^m(\mu_i) = \begin{cases} \left\{Z_0^0(\mu_i) - 2A_{\rm M}\sum_{i'=1}^{n} a_{i'}\mu_{i'}^{k_{\rm M}}\mu_i^{k_{\rm M}-1}Z_0^0(-\mu_{i'}) - A_{\rm M}F_0\mu_0^{k_{\rm M}}\mu_i^{k_{\rm M}-1}\right\}e^{-\tau_{\rm N}/\mu_0} & \text{for } m = 0 \\ Z_0^m(\mu_i)e^{-\tau_{\rm N}/\mu_0} & \text{for } m \neq 0 \end{cases} \tag{5.25}$$

$$M_j^m = L_j^m + L_{-j}^m e^{k_j^m\tau_{\rm N}} \tag{5.26a}$$

$$N_j^m = L_j^m - L_{-j}^m e^{k_j^m\tau_{\rm N}} \tag{5.26b}$$

$$A_{1j}^m = \begin{cases} A_{\rm M}\sum_{i'=1}^{n} a_{i'}\mu_{i'}^{k_{\rm M}}\mu_i^{k_{\rm M}-1}\left\{W_j^m(\mu_{i'}) + W_j^m(-\mu_{i'})e^{-k_j^m\tau_{\rm N}}\right\} & \text{for } m = 0 \\ 0 & \text{for } m \neq 0 \end{cases} \tag{5.27a}$$

$$A_{2j}^m = \begin{cases} A_{\rm M}\sum_{i'=1}^{n} a_{i'}\mu_{i'}^{k_{\rm M}}\mu_i^{k_{\rm M}-1}\left\{W_j^m(\mu_{i'}) - W_j^m(-\mu_{i'})e^{-k_j^m\tau_{\rm N}}\right\} & \text{for } m = 0 \\ 0 & \text{for } m \neq 0 \end{cases} \tag{5.27b}$$

$$L_j^m = \frac{1}{2}(M_j^m + N_j^m) \tag{5.28a}$$

$$L_{-j}^m = \frac{1}{2}(M_j^m - N_j^m)e^{-k_j^m\tau_{\rm N}}. \tag{5.28b}$$

Chapter 6

Treatment of Phase Functions

6.1 Inclusion of Modeled Martian Atmosphere

In this article, we modeled the Martian atmosphere as consists of these three components: CO_2 atmosphere, dust, and water ice cloud (WIC). The phase functions for the respective components are described in Chapter 7, and thus we just state the treatment of them here. The three components are abbreviated as R (="Rayleigh scatterer"), D (="dust"), and H (="H_2O crystal"). The subscript s and e represent scattering and extinction, respectively. Rewritten with the normalized scattering phase functions ψ, Eq. (4.2b) comes to

$$p(\cos\Theta) = \varpi_0\psi(\cos\Theta) = \varpi_0 \sum_{l=0}^{2n-1} \omega_l P_l(\cos\Theta), \tag{6.1a}$$

$$\varpi_l = \varpi_0\omega_l, \quad \omega_0 = 1, \tag{6.1b}$$

$$\frac{1}{4\pi}\int_{4\pi} \psi(\Omega)d\Omega = 1. \tag{6.1c}$$

Then the scattering phase functions for all the atmospheric components, $p_{\rm R}$, $p_{\rm D}$, and $p_{\rm H}$ are similarly expanded.

$$p_{\rm R}(\cos\Theta) = \varpi_0^{\rm R}\psi_{\rm R}(\cos\Theta) = \varpi_0^{\rm R} \sum_{l=0}^{2n-1} \omega_l^{\rm R} P_l(\cos\Theta) \tag{6.2a}$$

$$p_{\rm D}(\cos\Theta) = \varpi_0^{\rm D}\psi_{\rm D}(\cos\Theta) = \varpi_0^{\rm D} \sum_{l=0}^{2n-1} \omega_l^{\rm D} P_l(\cos\Theta) \tag{6.2b}$$

$$p_{\rm H}(\cos\Theta) = \varpi_0^{\rm H}\psi_{\rm H}(\cos\Theta) = \varpi_0^{\rm H} \sum_{l=0}^{2n-1} \omega_l^{\rm H} P_l(\cos\Theta), \tag{6.2c}$$

where $\psi_{\rm R}$, $\psi_{\rm D}$, and $\psi_{\rm H}$ are the normalized phase functions for the respective atmospheric components, and

$$\omega_0^{\rm R} = \omega_0^{\rm D} = \omega_0^{\rm H} = 1, \tag{6.3a}$$

$$\frac{1}{4\pi}\int_{4\pi} \psi_{\rm R}(\Omega)d\Omega = \frac{1}{4\pi}\int_{4\pi} \psi_{\rm D}(\Omega)d\Omega = \frac{1}{4\pi}\int_{4\pi} \psi_{\rm H}(\Omega)d\Omega = 1. \tag{6.3b}$$

When all the atmospheric components are homogeneously mixed, i.e., the particle distributions are independent on altitudes, we can represent the scattering phase functions ψ as the weighted mean of those of all the components as below:

$$\psi(\cos\Theta) = \frac{\psi_{\mathrm{R}}(\cos\Theta)\tau_{\mathrm{R}} + \psi_{\mathrm{D}}(\cos\Theta)\tau_{\mathrm{D},s} + \psi_{\mathrm{H}}(\cos\Theta)\tau_{\mathrm{H},s}}{\tau_{\mathrm{R}} + \tau_{\mathrm{D},s} + \tau_{\mathrm{H},s}}. \tag{6.4}$$

Here the subscript s for τ indicates the scattering optical depth. We then define that the single-scattering albedo ϖ_0 is a ratio of the scattering coefficient β_s to the extinction coefficient β_e, that is,

$$\varpi_0 = \beta_s/\beta_e, \quad \varpi_0^{\mathrm{D}} = \beta_{\mathrm{D},s}/\beta_{\mathrm{D},e}, \quad \varpi_0^{\mathrm{H}} = \beta_{\mathrm{H},s}/\beta_{\mathrm{H},e}, \quad \varpi_0^{\mathrm{R}} = \beta_{\mathrm{R},s}/\beta_{\mathrm{R},e} = 1. \tag{6.5}$$

The extinction coefficient β_e and the scattering coefficient β_s are also assumed to be independent on altitude. Then

$$\tau_{\mathrm{D},s} = \varpi_0^{\mathrm{D}}\tau_{\mathrm{D}}, \quad \tau_{\mathrm{H},s} = \varpi_0^{\mathrm{H}}\tau_{\mathrm{H}}, \quad \tau_{\mathrm{N},s} = \varpi_0\tau_{\mathrm{N}}, \tag{6.6a}$$

$$\tau_{\mathrm{N},s} = \tau_{\mathrm{R}} + \tau_{\mathrm{D},s} + \tau_{\mathrm{H},s} \tag{6.6b}$$

$$\tau_{\mathrm{N}} = \tau_{\mathrm{R}} + \tau_{\mathrm{D}} + \tau_{\mathrm{H}}. \tag{6.6c}$$

Hence the single-scattering albedo ϖ_0 and the normalization factors ω_l can be respectively expressed as

$$\varpi_0 = \frac{\tau_{\mathrm{R}} + \varpi_0^{\mathrm{D}}\tau_{\mathrm{D}} + \varpi_0^{\mathrm{H}}\tau_{\mathrm{H}}}{\tau_{\mathrm{R}} + \tau_{\mathrm{D}} + \tau_{\mathrm{H}}} \tag{6.7a}$$

$$\omega_l = \frac{\omega_l^{\mathrm{R}}\tau_{\mathrm{R}} + \omega_l^{\mathrm{D}}\tau_{\mathrm{D},s} + \omega_l^{\mathrm{H}}\tau_{\mathrm{H},s}}{\tau_{\mathrm{R}} + \tau_{\mathrm{D},s} + \tau_{\mathrm{H},s}}. \tag{6.7b}$$

6.2 δ-M Method

Applying the DOM described above to particles such as H_2O ice crystals and dust particles which have strong forward scattering peaks, the intensity distribution is not still stable for the discrete streams (i.e., μ_i). To avoid this problem, the δ-M method [*Wiscombe*, 1977] is employed. We give some description for our calculation.

The scattering phase function $p(\cos\Theta) = \varpi_0\psi(\cos\Theta)$ is approximated by

$$\begin{aligned} p^*(\cos\Theta) &= \varpi_0\psi^*(\cos\Theta) \\ &= \varpi_0\left[2f\delta(1-\cos\Theta) + (1-f)\sum_{l=0}^{2n-1}(2l+1)\chi_l^* P_l(\cos\Theta)\right], \end{aligned} \tag{6.8}$$

where f is a "truncation fraction" and $\delta(x)$ is Dirac's δ-function, and where the coefficients χ_l^* are determined by matching the moments of $\psi^*(\cos\Theta)$ to those of $\psi(\cos\Theta)$ (i.e., χ_l):

$$\begin{aligned} \chi_l &= \frac{1}{2}\int_0^\pi \psi^*(\cos\Theta)P_l(\cos\Theta)d\Theta \\ &= \begin{cases} f + (1-f)\chi_l^*, & l \leqslant 2n-1 \\ f, & m \geqslant 2n, \end{cases} \end{aligned} \tag{6.9}$$

which can be solved uniquely for χ_l^*,

$$\chi_l^* = \frac{\chi_l - f}{1-f} \tag{6.10}$$

(note that $\chi_0^* = 1$ because $\chi_0 = 1$) and non-uniquely for f:

$$f = \chi_l, \quad l \geq 2n. \tag{6.11}$$

The truncation fraction f can be arbitrarily determined as far as it satisfies Eq. (6.11). However, for consistency with the δ-Eddington approximation (i.e., the case of $n = 1$ in Eq. (6.8)), and for less importance of higher order moments than lower one, the least l is employed. That is,

$$f = \chi_{2n} = \frac{1}{2(2n)+1} \cdot \frac{\varpi_{2n}}{\varpi_0}, \tag{6.12}$$

so that

$$\chi_l^* = \frac{1}{1-f}\left[\frac{1}{2l+1} \cdot \frac{\varpi_l}{\varpi_0} - f\right]. \tag{6.13}$$

The δ-function has the following Legendre polynomial expansion:

$$\delta(x-y) = \sum_{l=0}^{\infty} \frac{1}{2}(2l+1)P_l(x)P_l(y) \tag{6.14}$$

Using this expansion, one can represent the difference between the exact and approximate phase functions as

$$\psi(\cos\Theta) - \psi^*(\cos\Theta) = \sum_{l=2n+1}^{\infty} (2l+1)(\chi_l - \chi_{2n})P_l(\cos\Theta). \tag{6.15}$$

It is shown that this difference usually tends to diminish as ψ becomes increasingly asymmetric [*Wiscombe*, 1977].

The equations which are obtained by substituting Eq. (6.8) into previously discussed phase functions p are equivalent to those by replacing as below [*Akabane et al.*, 1987]:

$$\varpi_0^* = \frac{(1-f)\varpi_0}{1-\varpi_0 f} \tag{6.16a}$$

$$\varpi_l^* = (2l+1)\chi_l^*\varpi_0 \quad (l = 1, 2, \ldots, 2n-1) \tag{6.16b}$$

$$\tau^* = (1-\varpi_0 f)\tau \tag{6.16c}$$

$$\chi_l^* = \frac{\chi_l - f}{1-f} \tag{6.16d}$$

$$f = \chi_{2n} \tag{6.16e}$$

Then the moments ω_l needed for calculation of $I(\tau, \mu_i)$ are

$$\omega_l = \varpi_0^*\omega_l^* \tag{6.17}$$

6.3 Estimation of Water Ice Opacities

Optical depths of water ice clouds are of interest in this article. At first, the intensity components which comes from the surface of the atmosphere can be derived from Eq. (4.32) by substituting $\tau = 0$:

$$I^m(0,+\mu) = \sum_{\substack{j=-n \\ j\neq 0}}^{n} L_j^m W_j^m(\mu)\left[1 - e^{(\mu^{-1}-k_j^m)\tau_N}\right] + Z_0^m(\mu)\left[1 - e^{(\mu^{-1}-\mu_0^{-1})\tau_N}\right], \tag{6.18}$$

The total intensity can thereby be calculated from Eq. (4.9):

$$I(0,+\mu,\phi) = \sum_{m=0}^{2n-1} I^m(0,+\mu)\cos m(\phi-\phi_0) \tag{6.19}$$

The above algorithm is primarily for calculating the intensity ($I(0,+\mu,\phi)$) by assuming the total optical depth ($\tau_{\rm N}$). What we need here is the water ice opacity at a certain point of interest, which we call here a "data point" (DP). We can obtain the total intensity at the DP ($I_{\rm DP}$) from Eq. (6.19). However, a single $I_{\rm DP}$ does not directly yield any optical depths (i.e., $\tau_{\rm N,\,DP}$) because we can not expose any reference stars for calibration by the same way for Mars due to their incomparably great difference in brightness.

We thus select from the image of Mars a "reference point" (RP), which is located in a near-noon region and at which we can assume $\tau_{\rm H,\,RP} \approx 0$. We adopt the total intensity of the RP ($I_{\rm RP}$) for calibration. By assuming the opacities of the other atmospheric components at both the data and reference points, and also assuming $\tau_{\rm H,\,RP} \approx 0$, we can theoretically retrieve intensity ratios $I_{\rm DP}/I_{\rm RP}$ as a function of $\tau_{\rm H,\,DP}$. We can finally obtain the water ice opacity which yields the observed intensity ratio $I_{\rm DP}/I_{\rm RP}$ by interpolation [see also Eq. (6.6c)].

Even if the uncertainties within the above-mentioned algorithm may be negligible, yet there should be some artificial errors/uncertainties due to the identification of topography and the seeing condition. A statistical procedure that extract "regional-mean" values in order to reduce the errors/uncertainties will be presented in Sections 9.2 and 9.3.

Chapter 7

Scattering Properties of Aerosols

"So, how do we observe Mars?" — This chapter gives the backbone of the observations. Described are the scattering properties of the three constituents within the modeled atmosphere introduced in Section 6.1 (water ice particles, dust particles, and CO_2 atmosphere), and the related optical properties of the ground surface.

7.1 Water Ice Clouds

The clouds composed of water ice crystals appear more prominent at shorter wavelengths because, for reasonable particle size distributions, their reflectance is relatively independent of wavelength compared to that of the surface, which is dominated by minerals containing oxidized iron which are highly absorbing short of 500 nm.

In visible wavelengths, we can safely considered that water ice particles of a moderate order (for the Martian atmosphere, of course) have uniform and high single-scattering albedo, $\varpi_0 = 1$. Such scattering properties of water ice particles can be readily, roughly but sufficiently estimated with model calculations of the classical Mie scattering theory. An example of such calculations are presented in Appendix B.

Choice of a scattering phase function of water ice clouds largely affects the values themselves of the derived optical thicknesses. As the scattering phase function of the clouds, we employed that of *Sassen and Liou* [1979] in Part III [*Nakakushi et al.*, 2001a] and that of *Clancy and Lee* [1991] in Part IV [*Nakakushi et al.*, 2002a]. The Sassen & Liou's phase function was produced at the wavelength of 640nm in a laboratory for ice particles of mean size of 3.5μm. The Clancy & Lee's phase function was derived in mid-latitudes from the Viking Orbiters' observations. The reason why we adopted the different phase functions is that we took into account the areophysical "trend" that the Clancy & Lee's phase function have recently seemed widely accepted, although we cannot and must not easily judge whether results from spacecraft or those from laboratory experiments is more appropriate because spacecraft do not always provide proper data [e.g., *Wilson and Richardson*, 2000]. The difference between them will be discussed in Chapter 10. A closer comparison is also presented in *Akabane et al.* [2002].

7.2 Ground Surface

McCord and Westphal [1971] reported their results from narrow-band spectrophotometric observations which covered the spectral region from 0.3 to 2.5μm with a resolution of 0.02-0.07μm. Their Fig. 6 shows the important one of their results on the surface geometric albedo spectrum.

Geometric albedo is defined to be the ratio of the brightness of a body at zero phase angle to the brightness of a Lambert disk (i.e., a perfectly reflecting, perfectly diffusing screen) of the same angular diameter as the body and oriented perpendicularly to the solar rays.

In the figure, the "bright" areas, so called due to their visibility (both in the literature and at present), are Arabia, Moab, and Area 59/74, and the "dark" areas are the four rests (Meridiani Sinus, Iapygia, Mare Acidalium, and Syrtis Major).

Martian bright areas are very red in color, reaching a maximum geometric albedo of 0.42 in the near-infrared; dark areas are less red. Although their mutual difference is greater in longer wavelengths, the more important for our observation is the less difference of albedo in shorter wavelengths. In blue regions (say, $\lambda < 4500$Å) there are no significant difference of albedos, so that we can safely assume no albedo surface features in those wavelengths.

7.3 CO_2 Atmosphere

The scattering properties of the CO_2 Atmosphere is rather simple in the visible wavelengths of our interest because no absorption can safely be assumed in this band, and because the "particle" size is so small that the scattering processes can be considered as Rayleigh scattering. The single-scattering albedo can thus be fixed to $\varpi_0 = 1$, i.e, a conservative case of perfect scattering. The phase function appeared in Section 6.1 is formulated with the well-known Rayleigh scattering phase function:

$$p_{\mathrm{R}}(\cos\Theta) = \frac{3}{4}(1 + \cos^2\Theta) \tag{7.1}$$

Of course this phase function is normalized to unity (this is equivalent to $\varpi_0 = 1$).

Some CO_2 ice clouds are suspended in the Martian atmosphere. Such CO_2 clouds are, however, restricted within the winter polar region (i.e., the polar hoods). Our interest is the tropical region: there are no airborne CO_2 ice (at least in daytime, only which can be observed from the Earth).

7.4 Dust

Many studies of dust optical properties, mostly by spacecraft, have been accumulated because of the importance of suspended dust particles to atmospheric phenomena. One of the successful Mars missions is the Mars Pathfinder mission. The lander has a camera onboard (IMP). The camera observed the distribution of brightness in the Martian sky at wavelengths from 444 to 965 nm at various times of day and various locations relative to the sun throughout its ~ 3 months of operation on the surface of Mars.

Tomasko et al. [1999] estimated the single scattering albedo of dust particles using some sets of images of the sky of Mars taken with the IMP camera. Their Figure 22 shows one of their important results. Although it has not been asserted that their results represent the most *exact* condition, the features are very common: the single-scattering albedo decreases in shorter wavelengths in accordance with the steep increase of the imaginary part of the refractive index (i.e., the absorption coefficient).

The dust phase function used in the analyses in this thesis is given by the empirical formula of *Pollack and Cuzzi* [1980].

Part III

The Cloud Effect: Contribution to Blue Clearing

Chapter 8

Blue Clearing, Past to Present

In addition to the phenomena discussed in the previous sections, there are a number of interesting features that show up on the Earth-based images and do not have obvious explanations in spite of the Viking, MPF, and MGS observations. These include the classical and unsolved problem of the "blue haze" and its counterpart "blue clearing" which annoyed almost all Mars observers in the history.

8.1 The Mystery: Historical Background

8.1.1 The "Blue Haze"

The "red" planet is not simply red. Images of Mars taken in ordinary light usually show, of course, surface detail and the distinction between bright and dark areas.

However, as the wavelength in which the images are taken is decreased, surface detail becomes increasingly obscured by what appears to be, and so had been long believed to be, a planet-wide haze. This "blue haze" is (was) already "quite apparent" at 4500Å, the extinction increasing rapidly towards shorter wavelengths. It should be emphasized that the haze is not *itself* blue; since it extinguishes the blue it probably would appear reddish. Mars is much less bright in the blue than in the red.

The standard explanation of the blue haze was a high-altitude layer in the Martian atmosphere which should cause extinction of solar blue light reflected from the surface, but which should be transparent at longer wavelengths.

In later years, the most extended theoretical explanation of the blue haze had been in terms of a layer of ice crystals of particle diameter of the order of 0.3 microns [e.g., *Kuiper*, 1952; *Hess*, 1958]. The extinction in the blue is explained by strong forward scattering of blue light by such particles, so that little light is reflected, and the haze is dark in the blue. At longer wavelengths the haze is transparent.

8.1.2 Blue Clearing and Blue Haze

Slipher [1937] discovered that on occasion the blue haze dissipates, and familiar surface details can be discerned. Such large dark features as Syrtis Major and/or Mare Acidalium sometimes can be seen in shorter (bluer) wavelengths. For the researchers in the years, this phenomenon must appear to be ascribed to "clearing" of the blue haze. This defines the classical "blue clearing" phenomena found in the literature: blue clearings were defined as occasional periods

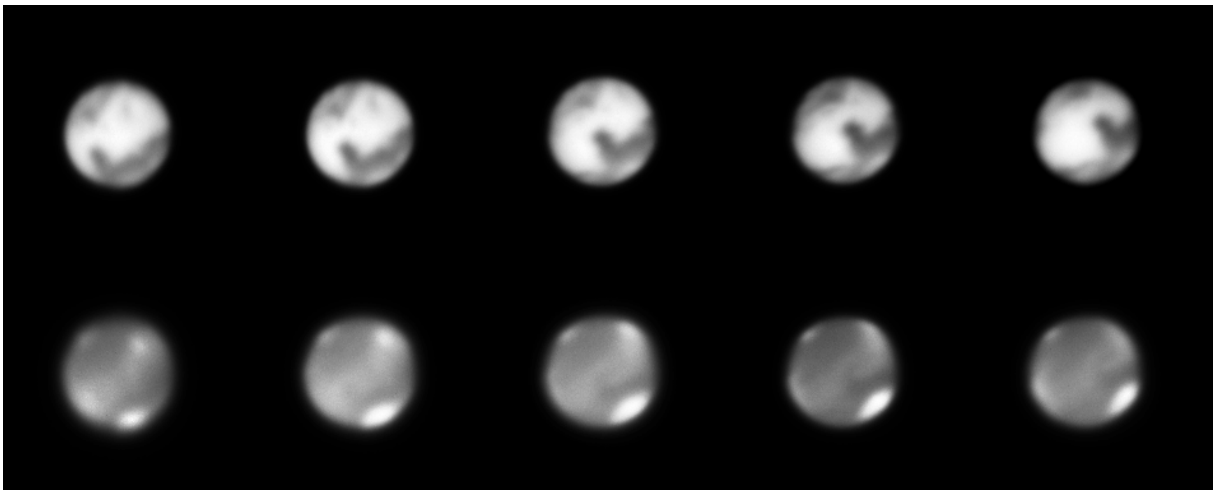

Figure 8.1: Images taken on April 20, 1999. Images in the same column were taken at the same time, images in the top row were taken with a red filter, and images in the bottom row were taken with a blue filter. The images in the left end correspond to the morning of Syrtis Major.

of a few days when a supposed blue or violet haze layer dissipated and allowed surface contrast to be seen at wavelengths below 4500Å.

Most of the more dramatic cases of blue clearing have been observed near favorable oppositions. There is an obvious observational selection, since Mars is most thoroughly investigated during favorable oppositions. Nevertheless, de Vaucouleurs has found, from a study of Lowell Observatory plates taken chiefly by E. C. Slipher during the 30 year interval ending in 1956, that when the effects of observational selection are removed there is still remains a correlation of blue clearing with favorable opposition [e.g., *de Vaucouleurs*, 1954]. Cases are also known of blue clearings at unfavorable oppositions [e.g., *de Vaucouleurs*, 1954], of blue clearings several months from opposition [*Richardson and Roques*, 1959], and of local blue clearings on small topographical scales down to the limit of resolution (cited by *Kellog and Sagan* [1961]). *Slipher* [1962] reached the following conclusions from the statistical study of more than 60,000 photos accumulated during the period from 1922 through 1960: Blue clearing is observed slightly more often around longitude 280°W, usually but not always near opposition, and frequently far from opposition.

Any explanation of the blue haze must have explain these highly erratic time variations in opacity. However, and of course from the recent standpoint, any in vain. Concepts of the "blue haze" as the counterpart for "blue clearing" had thereby dissipated more completely than the "blue haze."

8.2 Blue Clearing without "Blue Haze"

As Slipher showed, blue clearings seem to relate to oppositions, and to the relative positions of Mars, Earth and the sun (i.e., the phase angle), to some extent but not totally.

Then, how and why?

Syrtis Major is Mars' most prominent and therefore first known dark albedo feature. *Boyce and Thompson* [1972] showed that the degree of blue clearing at Syrtis Major in 1969 was the

strongest around opposition but decreasing as phase angle increases. This may be a typical appearance of blue clearing for the Syrtis Major case.

As a possibility next to the "blue haze" concepts, it is supposed that the lowering contrast of Martian features at short wavelengths may be due to a surface phenomenon and has nothing to do with a "blue haze" [e.g., *Thomas and Veverka*, 1986]. The lack of blue contrast is now known to be intrinsic to the Martian ground surface [e.g., *McCord and Westphal*, 1971]. *Boyce and Thompson* [1972] also concluded that blue clearing is due to variations in the bright areas, not the dark ones, and that it is a contrast enhancement occurring at all visible wavelengths. However, the difference in ground albedos between bright and dark areas is very small in blue light, and the brightness ratio is usually near unity [*Baum*, 1974]. Nevertheless, *Baum* [1974] proposed that a little change of the relative brightness should cause features to appear and/or disappear in blue light.

The key is the mechanism to explain how and why the surface contrast changes. The candidate of it was the opposition effect. Mars shows opposition effect for all visible wavelengths [e.g., *Thorpe*, 1982]. The idea of the opposition effect can readily and completely explain the dependence in blue clearings on phase angles. Therefore opposition effect should be taken into account in study of blue clearing. It seemed as if the mysterious phenomena of blue clearings was completely revealed.

Akabane et al. [1990] revealed from Earth-based observations that the degree of the blue clearing at Syrtis Major in the 1982 apparition showed dual components of variations: the phase-dependent component and the diurnal one. They did not succeed in "separation" of these two component literally, but did succeed in "treating" them separately. They then showed that the phase-dependent part increased as Mars approached the opposition, and that the diurnal component reaches a maximum near local noon at Syrtis Major. From those results, they suggested that the blue clearing phenomena in the Syrtis Major region in the 1982 apparition were caused by two processes: the opposition effect and the effect by water ice clouds. The latter is apparent contrast enhancement due to the low-latitude cloud belt. In that context, these two effects may not occur simultaneously; however, coincidence of those will make the blue clearing more prominent. Actually, the observed degree of blue clearing varies from year to year (see section 11.1) because the existence of the tropical cloud belt depends on the areocentric longitude of the sun L_s, while the opposition effect depends on the phase angle α. These facts contain great importance in a sense that the facts have brought blue clearings from an observational mystery up to observable phenomena which involve some (or many) *climatological* processes.

The goal of this part is to measure the contribution of the aphelion cloud belt to the blue clearing in the Syrtis Major region based on our recent ground-based observations. We start with the descriptions of our 1997 and 1999 observations and of image data used here. This is followed by the techniques and parameters we adopted in order to calculate the optical depths. Then we introduce the degree of blue clearing D and discuss our results of diurnal variations of D and those of the optical depth. Finally, we summarize the cloud effect and examine the identification of the most contributing region out of the three regions: Arabia, Syrtis Major, and Isidis.

The results in this part are presented in *Nakakushi et al.* [2001a].

Chapter 9

Analyses

9.1 Observations

Imaging observations were performed in the March 1997 and April 1999 apparitions, when Mars was in the northern summer and was at (or near) the opposition. The opposition dates were March 17, 1997, and April 24, 1999. The 60-inch reflector of Steward Observatory Mt. Lemmon Station was used in 1999 with a blue filter, and the 65-cm refractor of Hida observatory was used in 1997, also with a blue filter (see Table 9.1 and also Table 3.1).

In both apparitions the aphelion cloud belt was very active, especially the morning clouds, and the blue clearing in the Syrtis Major region was not observed as prominently as expected. However, we did observe the phenomenon on March 5, 1997, and April 20, 1999, during the first half of the observation hours on April 21, 1999, and during the last half of the observation hours on April 25, 1999. Figure 8.1 shows the sample images taken on April 20, 1999, in sequence of time.

Table 9.1: Observational Facts for Part III.

Date	L_s	α^a	d^b	LON_{SE} ^{c}	Images^d
March 5, 1997	87	10	13.7	273 - 7	23
April 20, 1999	127	4	15.9	257 - 337	94
April 21, 1999	127	3	16.0	260 - 313	60
April 24, 1999	129	1	16.1	216 - 275	55
April 25, 1999	129	1	16.1	209 - 284	74

[a] Phase angle.
[b] Apparent diameter of Mars.
[c] West longitude of the sub-Earth point.
[d] Total number of image analyzed.

9.2 Apparent Brightness

The primary foci of our analyses are the apparent brightnesses and the optical depths of these four regions: Syrtis Major (SM), adjacent Arabia (AR) and Isidis (IS), and the midlatitude cloud-free region near the central meridian. Hereafter, we refer to bright and dark regions according to their reflectances in red light, where surface contrasts are most pronounced. According to this nomenclature, Syrtis Major is a dark region, and Arabia and Isidis are bright regions. All of these are the northern tropical regions overcast by the aphelion cloud belt.

Our analyses started off by determining the position of the image disk center and the radius of the image disk. However, accuracy in these measurements depends largely on the seeing conditions. The high contrast of the bright H_2O clouds can distort the location of the apparent limb, especially near the polar caps and the equatorial limb regions. Moreover, in the measurements of apparent brightnesses the choice of Martian points is artificial, so that there may be selection bias. In order to reduce these errors which are caused by the identifications of both the topographic and on-image coordinates, the measurements of apparent brightnesses were performed as follows. Five data points (DPs) for each region were selected from the Arabia, Syrtis Major, and Isidis regions. The topographic coordinates of these DPs are (315° W±5° , 10° N±5°) in Arabia, (290° W±5° , 10° N±5°) in Syrtis Major, and (270° W±5° , 20° N±5°) in Isidis. Hereafter, the term "local time" implies the local time at the central point of these five DPs in the region concerned.

Our optical depth calculation code requires the apparent brightnesses of cloud-free reference points under normal surface conditions. *Clancy et al.* [1996] and *James et al.* [1996] reported that the latitudinal range of the aphelion cloud belt is 10°S-30°N. According to *Hansen et al.* [1999], the boundary of the north polar cap is 74.5°N at $L_s = 199.5°$. In terms of the images used in this paper, the boundary of the north polar cap should be at latitudes higher than 74.5°N because it was northern summer, while the south polar cap edge should be at 55°-60°S [e.g., *Iwasaki et al.*, 1989; *James et al.*, 1987, 1996]. Therefore the region which is cloud-free and above which the atmospheric pathlength is small is restricted to the midlatitudinal region near the central meridian. And so we selected five reference points (RPs) of common topographic coordinates to all images within an image set from there in order to accomplish the radiative transfer calculations. Pixel values of DPs and RPs were extracted (binned by 9 pixels) around each point.

Our calculation schemes employ ratios or differences of optical properties (apparent brightnesses and optical depths) between two points in pairs of regions concerned. Also, our analyses and discussions (see Chapters 10 and 11) are based on "regional-mean" ratios and differences. Because there are five selected points for each region and two to five images for each image set, these ratios or differences can be produced from 50-125 combinations of DP-DP or DP-RP; therefore we can obtain as many calculated values. The outline of this "regional-mean" method is described in Figure 9.1. The results presented in this paper are the averages over all 50-125 values, with 2σ rejection. We assumed that these averaged values were confident enough to allow us to neglect the measurement uncertainties and the errors due to the selection bias, whereas standard errors due to this statistical procedure should remain.

9.3 Estimation of the Optical Depths

The adopted phase functions for CO_2, dust, and H_2O crystal are that of Rayleigh scattering, *Pollack and Cuzzi* [1980], and *Sassen and Liou* [1979], respectively. For the single-scattering albedos ϖ_0 of CO_2 and H_2O crystal, we approximated that only scattering by these particles

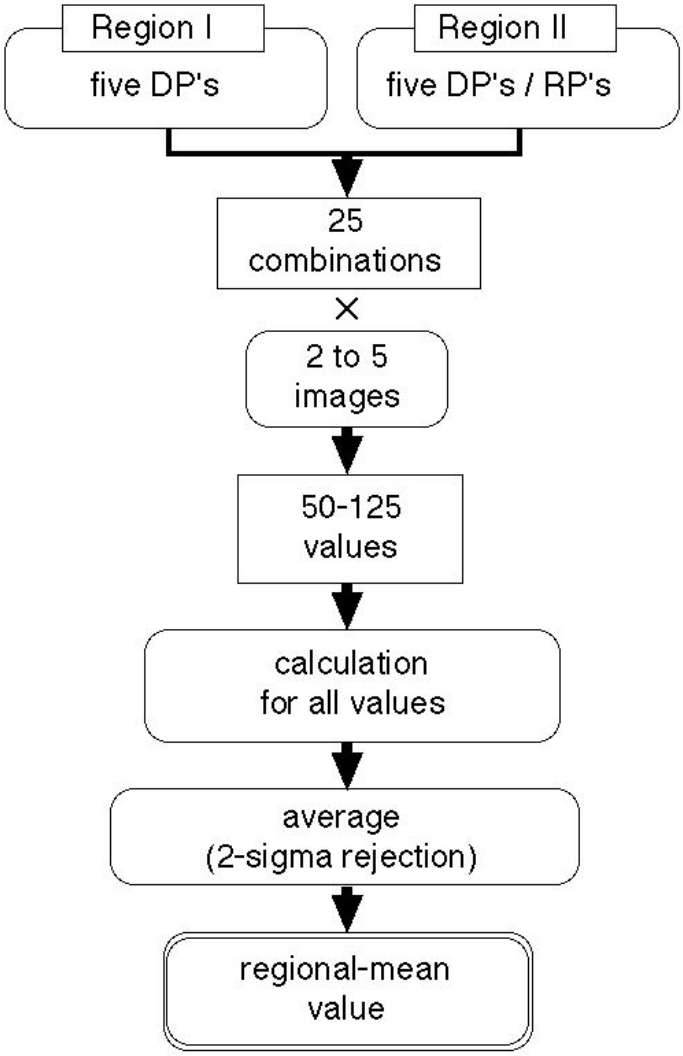

Figure 9.1: Statistical procedure employed to derive the "regional-mean" values.

should contribute to extinction and that there are no contributions of absorption, i.e., $\varpi_0 = 1$. For the dust single-scattering albedo for our observation wavelengths ($\lambda \sim 4300$Å), we adopted $\varpi_0 = 0.730$, which was derived from the refractive index of $n = 1.5 - 0.009i$ [*Pollack et al.*, 1977, 1979].

Dust distribution varies with time and places; however, we assumed a constant dust opacity of $\tau_{\rm D} = 0.15$ [*Lumme et al.*, 1981] and also assumed a constant CO_2 atmosphere opacity of $\tau_{\rm R} = 0.01$ [*Wells*, 1979]. Our preliminary calculations using the MPF results about dust properties ($\varpi_0 = 0.72$, Im$(n) = 0.018$, $\tau_{\rm D} = 0.45$ [*Smith and Lemmon*, 1999; *Tomasko et al.*, 1999]) have shown almost the same results as will be presented later (in Section 10). Our dust opacity is 1/2-1/3 of the Viking/Pathfinder values for this period. However, it has been revealed that at least Viking IRTM data should be corrected [*Wilson and Richardson*, 2000]. On the other hand, it is suggested by *Clancy et al.* [2000] that Mars Pathfinder may be there in unusually dusty and warm Mars years. From this viewpoint, dust opacity in northern late spring/early summer is likely to be ~ 0.2 in the case without dust storms in the vicinity of the points of interest (as in

Figure 10 of *Clancy et al.* [2000], although the figure is a comparison of visible dust opacities). In any case, dust opacity affects the estimated intensity value itself but has little effect on the ratio of intensity $I_{\rm DP}/I_{\rm RP}$, which our codes require. Using the same codes, *Akabane et al.* [2002] examined the difference of $\tau_{\rm H}$ between the two cases of $\tau_{\rm D} = 0.5$ and $\tau_{\rm D} = 0.2$: the cloud opacity increased about 10% on morning and evening sides and decreased about 10% around local noon in the case of $\tau_{\rm D} = 0.5$ compared to the case of $\tau_{\rm D} = 0.2$.

For the ground reflectance function we employed the well-known Minnaert's function with the index of $k_{\rm M} = 0.5$ and with the ground albedo in blue of $A_n = 0.07$.

Using this model and assuming no cloud scattering over the RPs, that is, $\tau_{\rm H,RP} = 0$ (subscript H implies H_2O ice clouds), we can derive the surface brightness ratio of DP to RP as a function of $\tau_{\rm H,DP}$. We estimated $\tau_{\rm H,DP}$ that gives the observed surface brightness ratio for every combination of DP and RP included in one image. Then we extracted the "true" $\tau_{\rm H,DP}$ for an image set by averaging over all the estimated $\tau_{\rm H,DP}$ values through 2σ rejection.

Chapter 10

Results

10.1 Optical Depth of Water Ice Clouds

We estimated the optical depths of H_2O ice clouds (τ_H) in the Arabia, Syrtis Major, and Isidis regions along the methods described in Part II. It is found empirically that Minnaert's reflectance function approximately describes the variation of brightness of many surfaces over a limited range of angles. We limited the range to where both the incident and the emergent angles are $< 60^\circ$, which corresponds to the time range from 0800 to 1600MLT because our imaging observations were near the oppositions.

Figures 10.1, 10.2, and 10.3 show the derived diurnal variations of τ_H. The standard errors, defined as $\sqrt{V/N}$, where V is the unbiased variance and N is the total number of calculated values, are < 0.019. Some recent analyses have reported smaller cloud opacities than ours; for example, by factors of 2/3–1/2 [*James et al.*, 1996], and 1/2–1/3 [*Wolff et al.*, 1999]. This is attributed to the choice of phase functions. Our preliminary calculation results using a multilayered model instead of the one-layered model did not show any significant differences from the results presented here. Another preliminary calculation using the H_2O crystal phase function presented by *Clancy and Lee* [1991] and *James et al.* [1994] instead of that of *Sassen and Liou* [1979] results in smaller values of τ_H than presented here by a factor of $\sim 2/3$, which are considered to be within a range of consistence with the recent reports, and also results in the time-dependent features still being the same. Determination of the "best" phase function is the goal of a future study.

10.2 Degree of Blue Clearing

Blue clearing is a phenomenon of "apparent" visibility, in a sense. For scientific purposes, we have to quantify its degree. Here we define the degree of blue clearing D as the quantitative indicator, which is

$$D = \frac{B_b - B_{SM}}{B_b} \times 100, \tag{10.1}$$

where B is the apparent brightness and the subscripts b and SM are abbreviations for the adjacent bright area (Arabia or Isidis) and Syrtis Major, respectively. From this definition, D implies a kind of apparent contrast between Syrtis Major and its neighboring bright regions. Figures 10.4 and 10.5 show the diurnal variations of D. The standard errors are <4.80. The time ranges are limited when the local times of the central DPs of both regions concerned were within 0800–1600MLT. Increases before local noon and decreases in the afternoon can be found

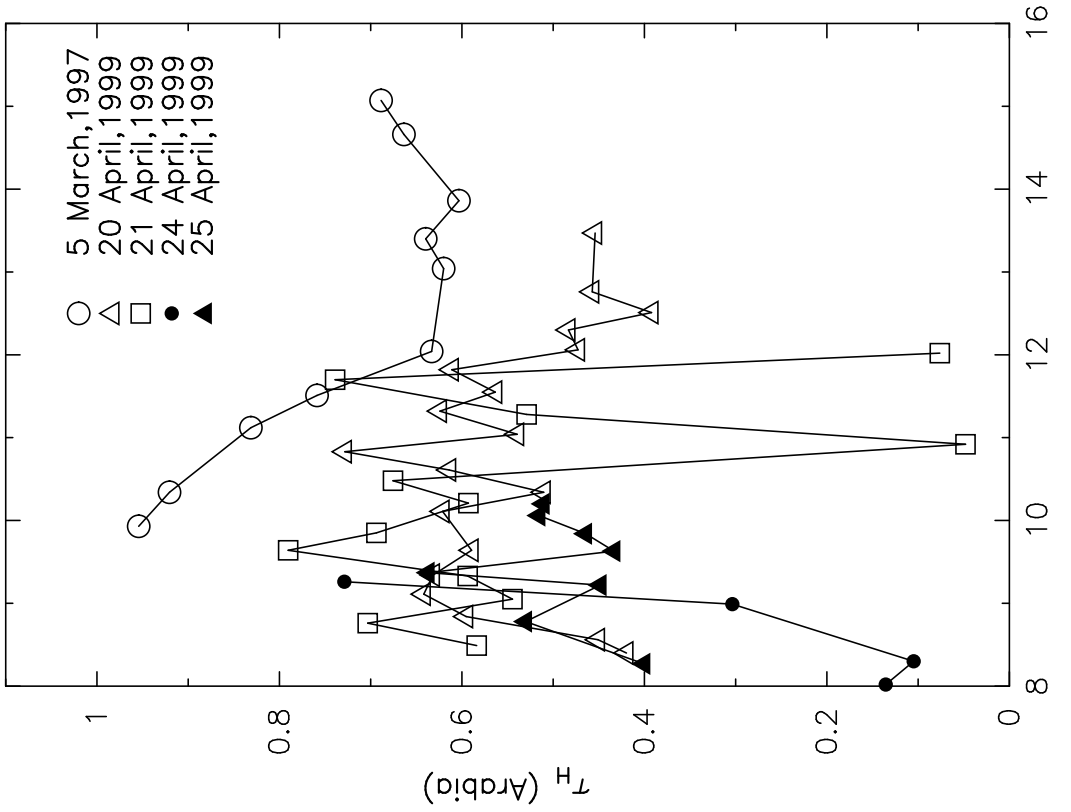

Figure 10.1: Diurnal variation of τ_H at Arabia. The abscissa is local time (hour). Local noon is 1200MLT.

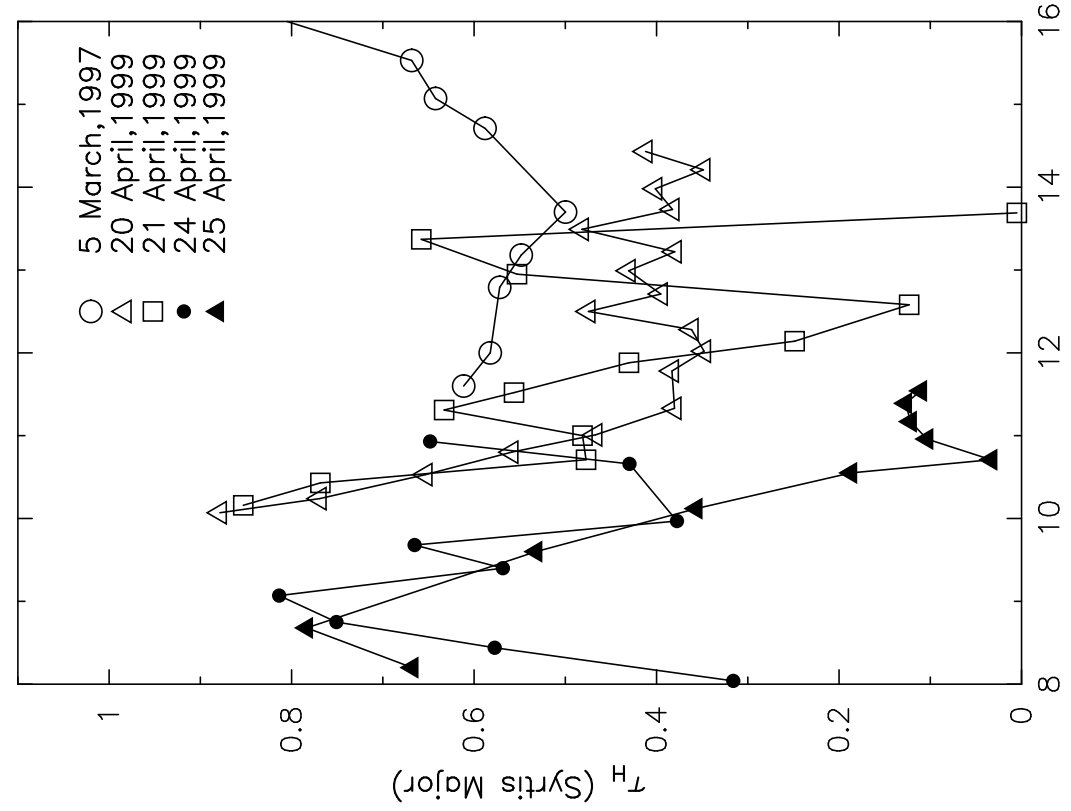

Figure 10.2: Diurnal variation of τ_H at Syrtis Major.

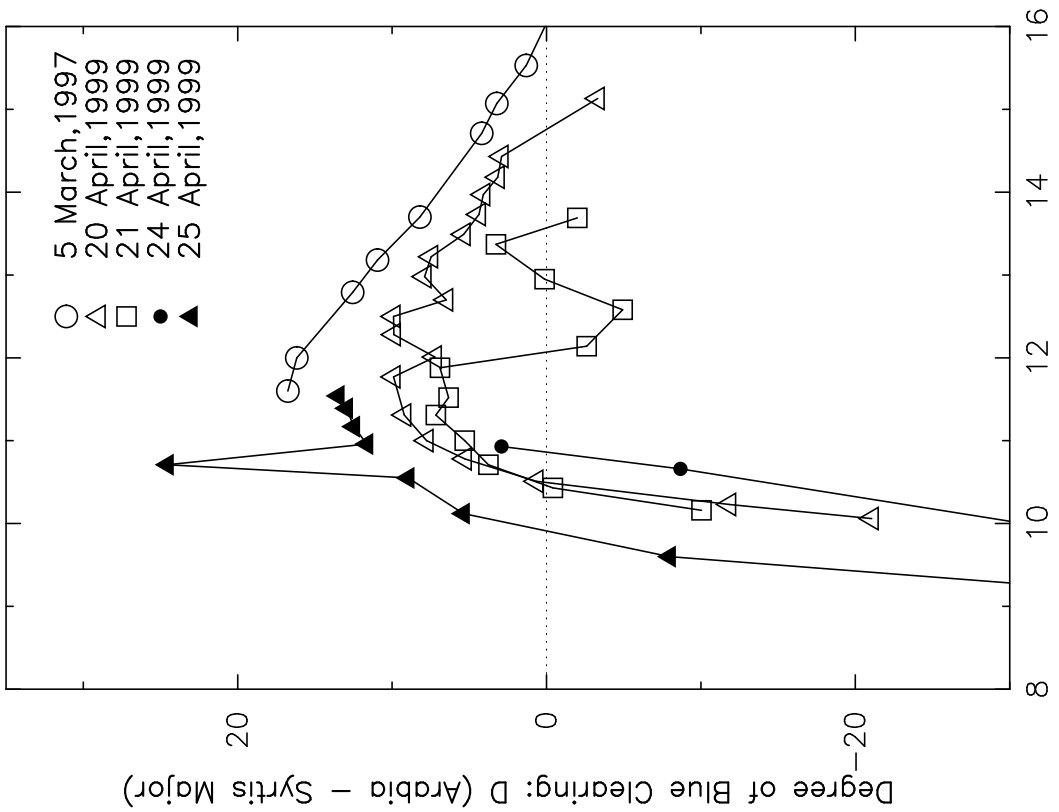

Figure 10.4: Diurnal variation of D between Syrtis Major and Arabia.

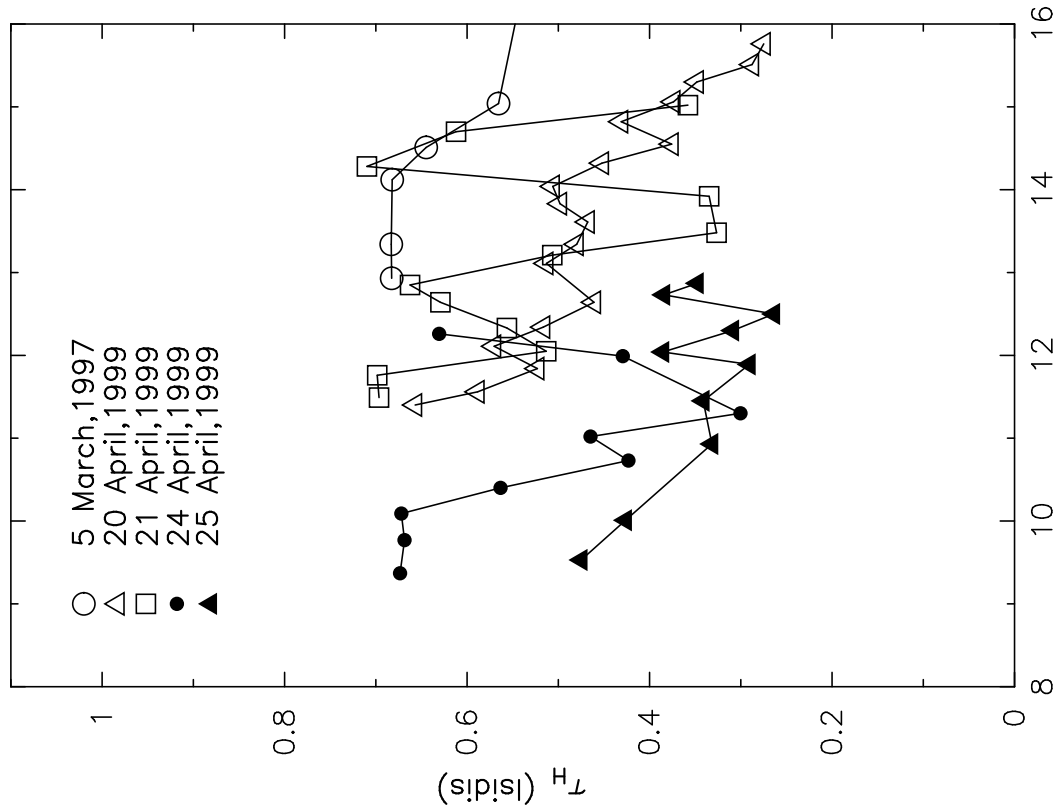

Figure 10.3: Diurnal variation of $\tau_{\rm H}$ at Isidis.

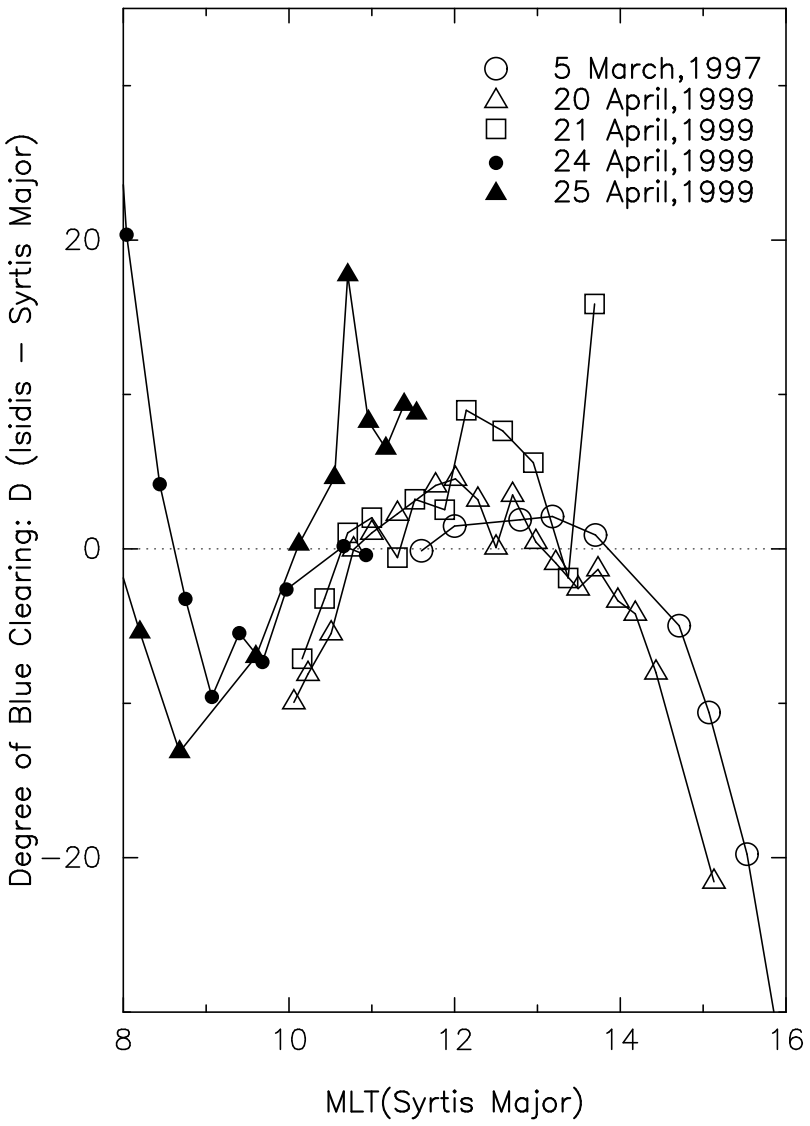

Figure 10.5: Diurnal variation of D between Syrtis Major and Isidis.

in the general features. In our visual inspections of images, the blue clearing was identified when $D \geq 5$.

The degree of blue clearing D has an increasing trend from 0900MLT to local noon and becomes $D \geq 0$ at about 1000–1100MLT. In Figures 10.4 and 10.5 the inclinations of the increase are mostly constant in each figure regardless of the observation dates, which are steep in Figure 10.4, while the D value in Figure 10.5 for each day has a local minimum at about 0900MLT. These features can be regarded as reflections of the fact that Syrtis Major lay then under the thickest and brightest part of the morning clouds, which is consistent with $\tau_{\mathrm{H,SM}}$ reaching a local maximum at about ∼0900MLT in Figure 10.2. In addition, Figures 10.1 and 10.3 both show that τ_{H} indicates a larger value at ∼0900MLT in each region than at other times. The morning clouds are therefore most activated at around 0900MLT, that is, 45° east of the longitude of the sub-solar point. This is consistent with the results of *Wolff et al.* [1999, e.g., Plate 2].

Contrary to the features before local noon, D values have a decreasing trend in the afternoon.

These decreasing trends are less steep than the increase before local noon and have no distinct difference for the observation dates, so that the times that D becomes negative differ for the dates. Figure 10.4 shows larger variations and larger peak values than Figure 10.5, which implies that the blue clearing phenomena were observed more prominently in the Arabia–Syrtis Major cases than in the Isidis–Syrtis Major cases.

Chapter 11

Remarks

11.1 Cloud Effect

Here we define the difference of the optical depths $\Delta\tau_{\rm H}$ as

$$\Delta\tau_{\rm H} = \tau_{\rm H,b} - \tau_{\rm H,SM}, \tag{11.1}$$

where the subscripts are similar to those in Eq. (10.1). Figures 11.1 and 11.2 are the derived diurnal curves of $\Delta\tau_{\rm H}$ as a function of MLT in the Syrtis Major region. The time spans are the same as D. The standard errors are $\sim$0.025.

From the comparisons of Figure 10.4 with Figure 11.1 and of Figure 10.5 with Figure 11.2, all examples show strong correlations between $\Delta\tau_{\rm H}$ and D, or in other words, $\Delta\tau_{\rm H}$ varies concurrently with D. This relationship can be explained as this. Large values of $\tau_{\rm H}$ indicate that H_2O ice clouds there are optically thick, while H_2O ice clouds are observed bright in blue, so that those regions of large $\tau_{\rm H}$ values should be observed bright. According to the definition of $\Delta\tau_{\rm H}$ [Eq. (11.1)], larger $\Delta\tau_{\rm H}$ implies larger excess of $\tau_{\rm H}$ in the bright region (i.e., Arabia or Isidis) over that in the dark Syrtis Major region. Therefore the apparent contrast, i.e., the degree of blue clearing D, should be large when $\Delta\tau_{\rm H}$ is large. In other words, the region-to-region "positive difference" of the optical depths results in the apparent contrast enhancement. In conclusion, the correlation between $\Delta\tau_{\rm H}$ and D as mentioned above suggests that the diurnal variation of $\Delta\tau_{\rm H}$, possibly attributed to the (difference of the) geographical and/or topographical features, should cause the synchronized variation of D. This is what we call here the "cloud effect."

Previously observed D values have differed from year to year, as seen in Table 11.1. The aphelion cloud belt seems to be present mostly between $L_s = 60^\circ$ and 150° and to be strongest from 100° to 120°. Thus blue clearing in 1969 and 1971 apparitions should be mainly due to the opposition effect, and the differences of these D values can be ascribed to the interannually varying state of surface regolith, unless it was due to seeing conditions. Needless to say, cloud activity also differs from year to year. Among various situations, some cloud conditions can be expected to reduce the apparent contrast, for instance, the case of extremely activated (therefore very opaque) clouds in higher altitudes. As *Clancy et al.* [1996] pointed out, warmer climate will lead to higher water saturation altitudes. Such clouds may conceal the surface contrast, and the diurnal activity variation of such clouds may depend less on the geographical and/or topographical features. The small D value in 1967 may be attributed to such a condition.

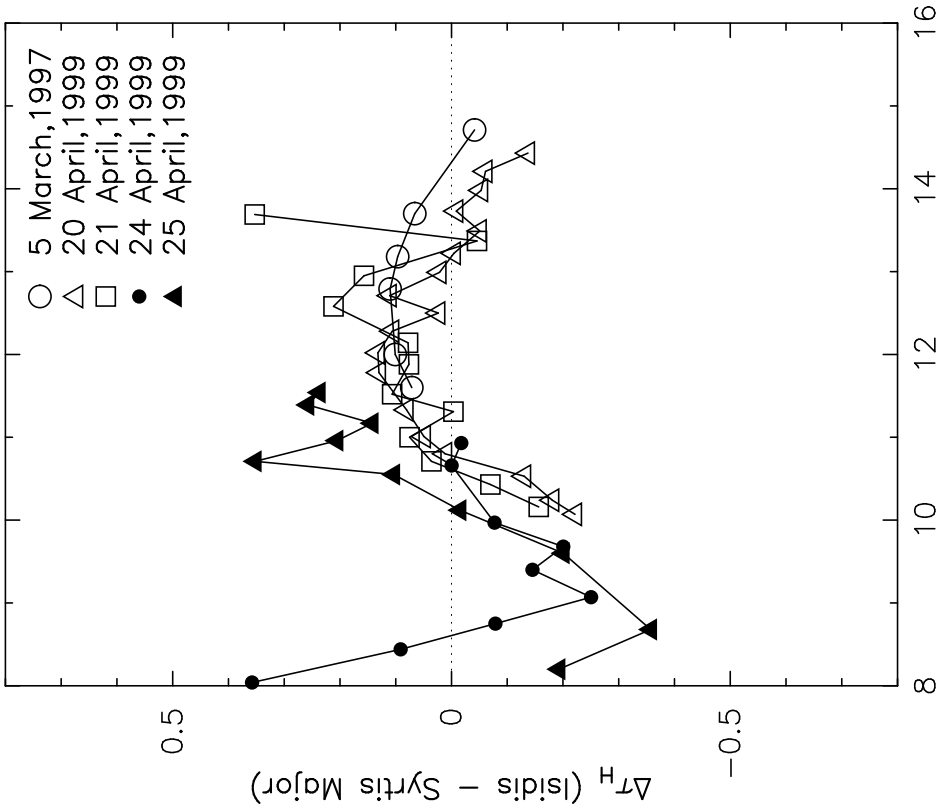

Figure 11.2: Diurnal variation of $\Delta\tau_{\rm H}$ (Isidis–Syrtis Major).

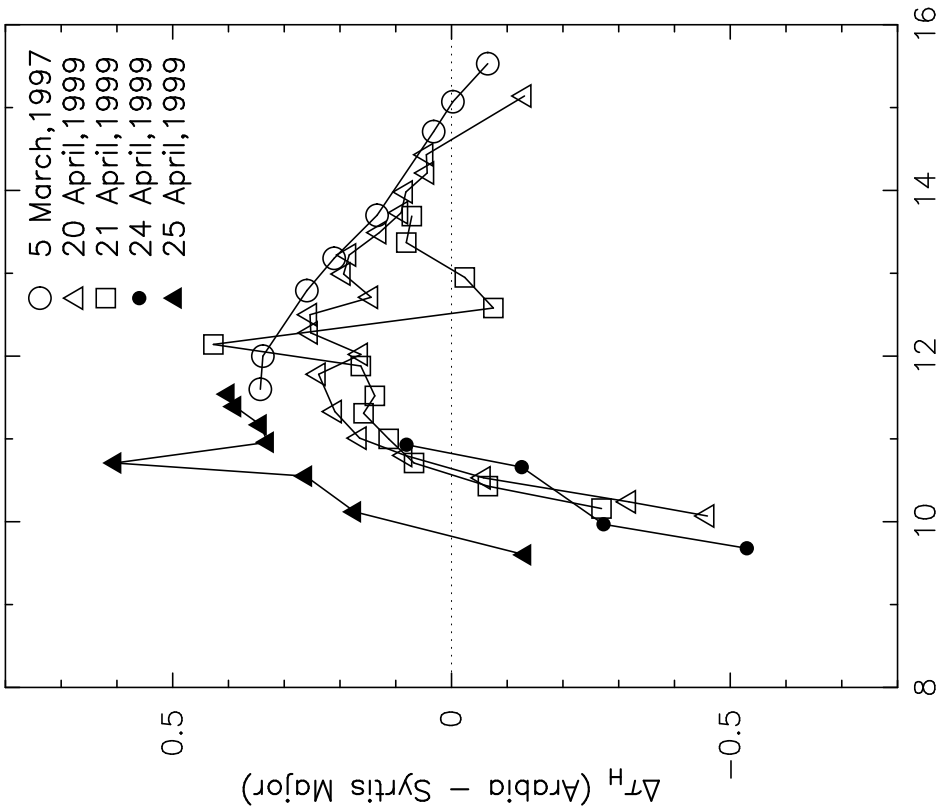

Figure 11.1: Diurnal variation of $\Delta\tau_{\rm H}$ (Arabia–Syrtis Major).

Table 11.1: Records of D for Arabia–Syrtis Major.

Year	D^*	$\alpha^\dagger$	L_s	λ, μm	Reference
1967	4	6	122	0.40	*McCord et al.* [1971]
1969	18	0	166	0.43	*Boyce and Thompson* [1972]
1969	13	5	162	0.40	*McCord et al.* [1971]
1971	6	5	233	0.43	*Thompson* [1973]
1982	16	2	105	0.40	*Akabane et al.* [1990]
1997	17	10	87	0.44	this study
1999	13(24)‡	1	129	0.43	this study

* Degree of blue clearing for Arabia–Syrtis Major. See section 10.2 of the text.
† Phase angle in degrees (negative values indicate before opposition).
‡ The parentheses imply an anomalous value which seems to be due to extraordinarily good seeing.

11.2 Correlations Between D and $\tau_{\rm H}$

In the previous sections, we showed that D values are strongly subject to the optical depths. The further question is, which region has the dominant effect on D: Arabia, Syrtis Major, or Isidis?

Here we assume the plotted points of $D \geq 0$ to be in the state of blue clearing, or just before or after. Figures 11.3, 11.4, 11.5, and 11.6 are the scatter diagrams for D versus $\tau_{\rm H}$ in the state of $D \geq 0$. We examined regression analyses using the simple linear regression model to these scatter diagrams, which means investigating the correlations between the values of D and $\tau_{\rm H}$ themselves without taking temporal dependence into account. We assumed the standard errors to be negligible here and did not take into account the weights by the total number of data used in averaging. The dashed lines in the scatter diagrams indicate the regression lines of D to $\tau_{\rm H}$, defined as

$$D = c_0 + c_1 \tau_{\rm H}.$$

Derived regression coefficients c_0 and c_1, variances V_e, and sample correlation coefficients r are shown in Table 11.2. The variance V_e is defined as

$$V_e = \frac{1}{N-2} \sum_{i=1}^{N} \Big[D_i - (c_0 + c_1 \tau_{\rm H,i}) \Big]^2,$$

where N is the total number of plotted points. We did not perform regression analyses for the cases on April 24, 1999, because of the insufficient plotted points (too small N).

Roughly said, $\tau_{\rm H,AR,\ or\ IS}$ and $\tau_{\rm H,SM}$ have positive and negative correlations to D, respectively. This is consistent with the correlations between D and $\Delta\tau_{\rm H}$ shown in the previous section (see equation (11.1)). The sample correlation coefficients for six cases surpass the threshold of the confidence coefficient of 95% (see Table 11.3): the $D_{\rm AR\text{-}SM}$–$\tau_{\rm H,AR}$ cases for March 5, 1997, and April 20, 1999; the $D_{\rm AR\text{-}SM}$–$\tau_{\rm H,SM}$ case for April 25, 1999; and the $D_{\rm IS\text{-}SM}$–$\tau_{\rm H,SM}$ cases for April 20, 21, and 25, 1999. However, there still remain 10 cases that cannot be explained by a dependence on single $\tau_{\rm H,SM,\ or\ b}$. This can first attributed to there being few data points on the scatter plots, which leads to larger thresholds. Second, the essence of the cloud effect is the

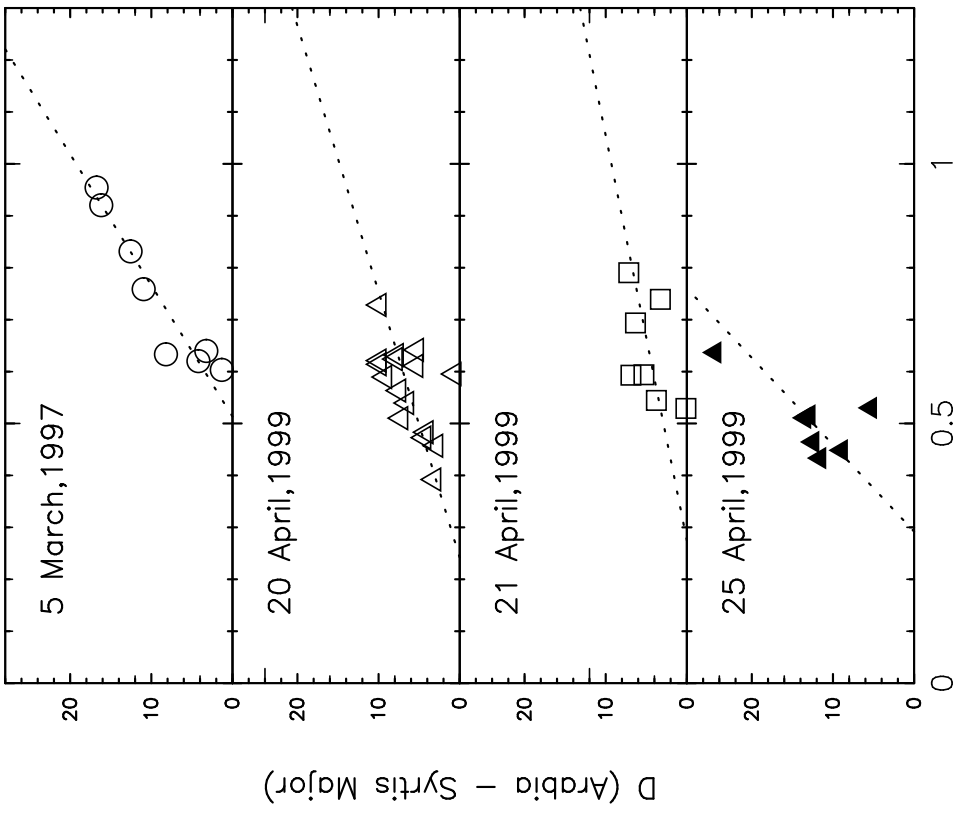

Figure 11.3: Scatter diagrams of τ_H (Arabia) versus D (Arabia–Syrtis Major).

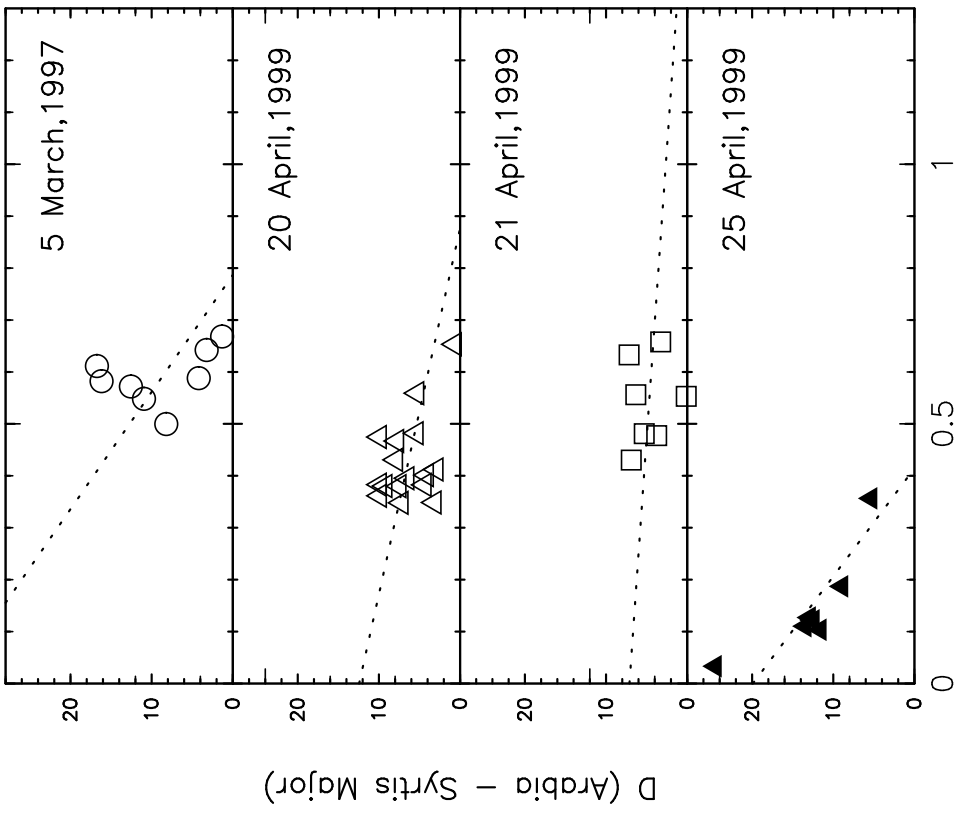

Figure 11.4: Scatter diagrams of τ_H (Syrtis Major) versus D (Arabia–Syrtis Major).

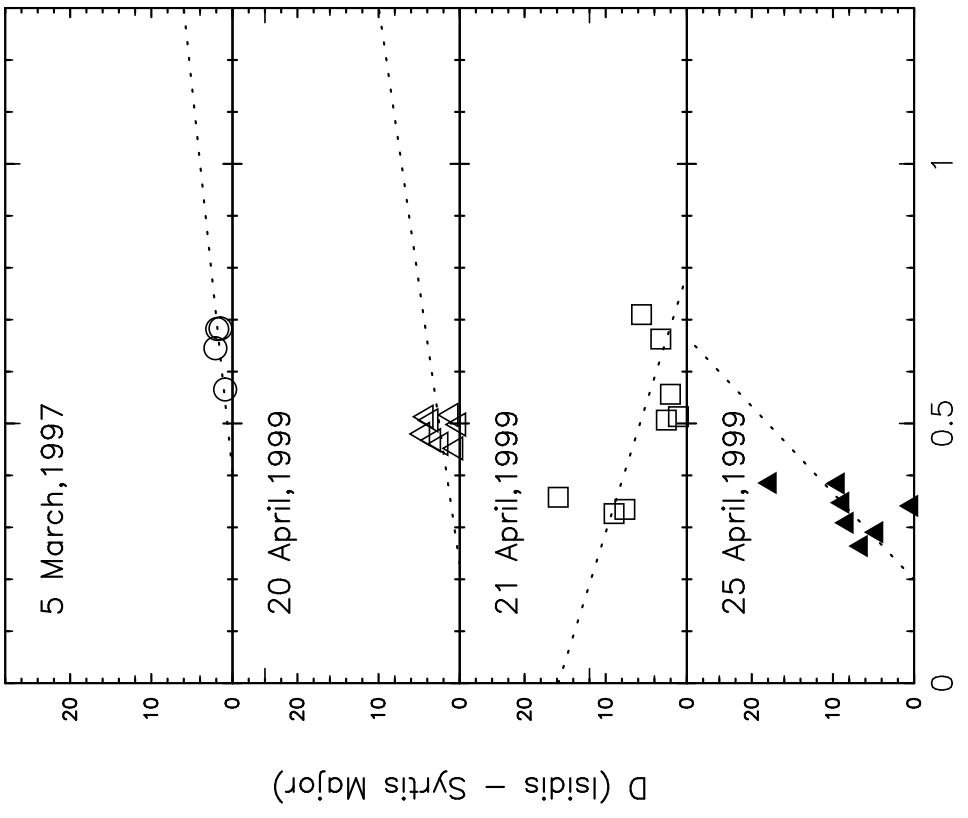

Figure 11.5: Scatter diagrams of τ_H (Isidis) versus D (Isidis–Syrtis Major).

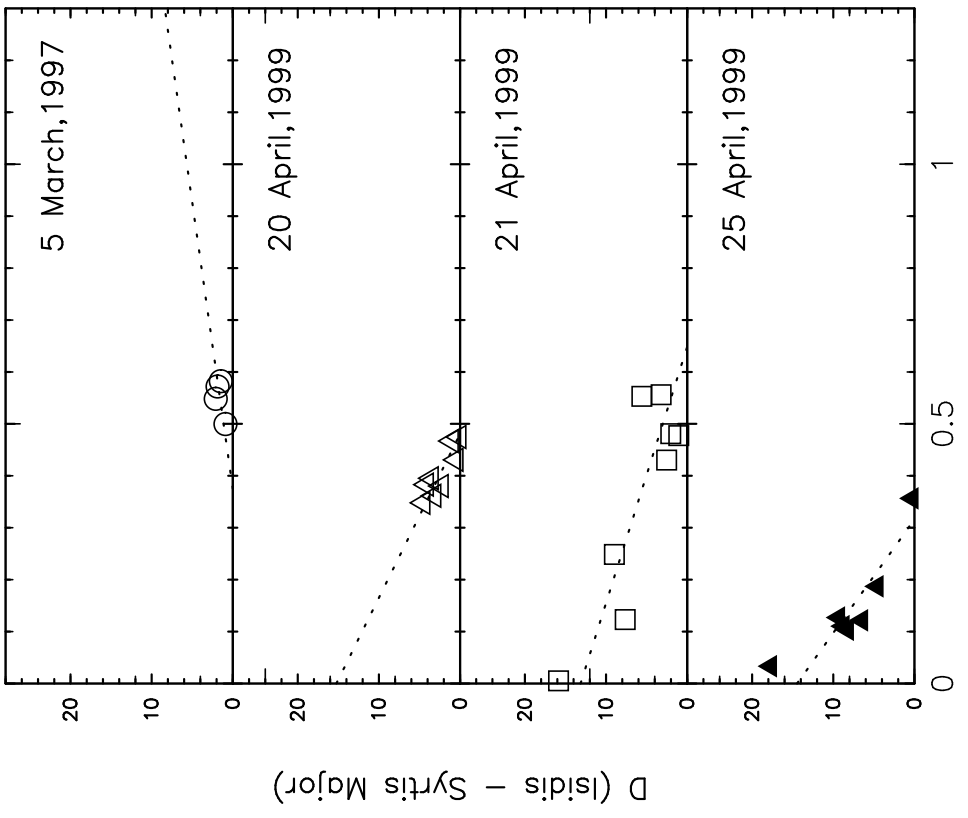

Figure 11.6: Scatter diagrams of τ_H (Syrtis Major) versus D (Isidis–Syrtis Major).

Table 11.2: Results from the Regression Analyses.

D	$\tau_{\rm H}$	Date	n	c_0	c_1	V_e	r
AR−SM	AR	March 5, 1997	8	−20.33	39.59	3.690	0.9535
		April 20, 1999	16	−4.725	19.53	5.434	0.5961
		April 21, 1999	7	−3.524	12.83	5.555	0.5156
		April 25, 1999	7	−17.44	59.77	21.84	0.6924
AR−SM	SM	March 5, 1997	8	34.89	−43.66	5.866	−0.2886
		April 20, 1999	16	12.43	−14.19	6.959	−0.4177
		April 21, 1999	7	7.121	−4.481	7.398	−0.1499
		April 25, 1999	7	19.92	−48.05	13.00	−0.8307
IS−SM	IS	March 5, 1997	4	−2.744	6.729	0.2102	0.7042
		April 20, 1999	8	−2.135	9.304	3.327	0.1361
		April 21, 1999	8	15.84	−20.12	17.95	−0.6021
		April 25, 1999	7	−11.96	59.98	24.86	0.5199
IS−SM	SM	March 5, 1997	4	−3.399	9.061	0.2504	0.6317
		April 20, 1999	8	15.23	−31.70	0.7670	−0.8796
		April 21, 1999	8	13.15	−20.27	7.371	−0.8592
		April 25, 1999	7	14.77	−46.01	7.524	−0.8827

differential variation of $\tau_{\rm H}$, so that these 10 cases imply equivalent contributions of $\tau_{\rm H,SM}$ and $\tau_{\rm H,b}$. On the other hand, the extracted six cases that actually indicate a dependence on single $\tau_{\rm H}$ consist of two cases for $\tau_{\rm H}$ of the adjacent areas and four cases for $\tau_{\rm H}$ of Syrtis Major. This result that $\tau_{\rm H,SM}$ values have significant correlations in more cases than for $\tau_{\rm H,b}$ suggests conclusively that the leading region of the cloud effect should be Syrtis Major.

Table 11.3: Thresholds of Correlation Coefficients with Confidence Coefficient of 95% .

N	r
4	0.950
7	0.754
8	0.707
16	∼0.5

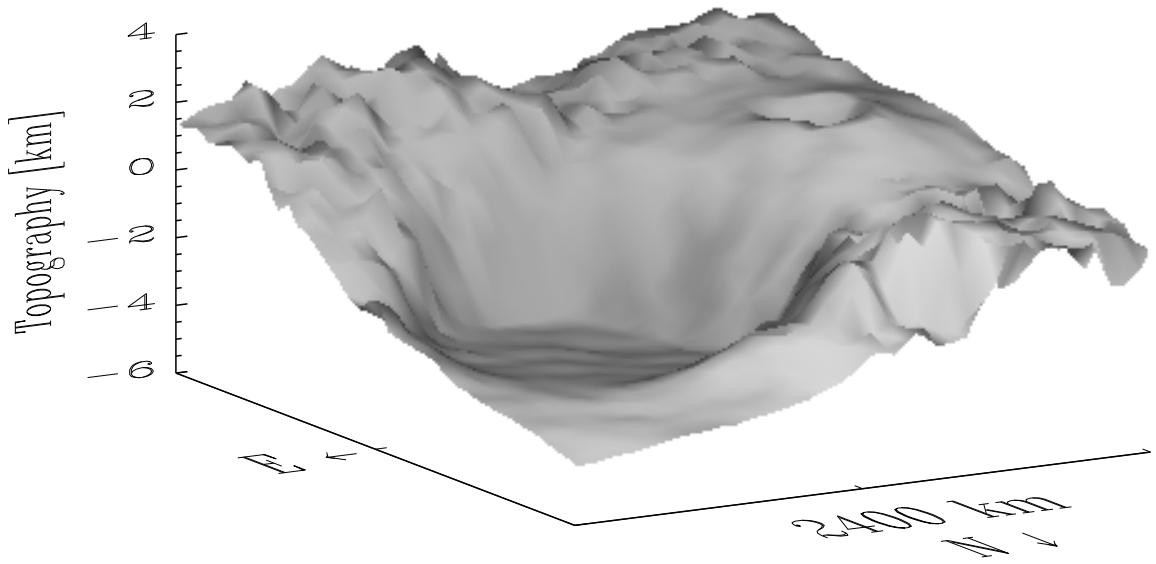

Figure 11.7: Local topography in the east of Syrtis Major (10°S-30°N and 260°W-300°W), viewed from the northeast. The dataset is the same as Figure 2.1. The horizontal length of 40° there corresponds to $\sim$ 2400km, because the areoid radius near the center of this area (9.5°N, 279.5°W) is 3395.81km.

11.3 Particularity in the Syrtis Major Region

The particularity in the Syrtis Major region may be interpreted as interactions with the topography. The maps of the daytime (1400MLT) spatial distribution of water ice cloud opacity by MGS TES, averaged over the northern summer (Plate 4 of *Smith et al.* [2001] for L_s = 104°-140° and Plate 2a of *Pearl et al.* [2001] for L_s = 106°-141°), shows a cloud absence forming a "triangle" centered at around 280°W in the cloud belt. Comparing that with Figure 2.1, we find that the location corresponds to a topographical lowland (basin) of Isidis Planitia. Our Figures 10.1-10.3 also show somewhat less cloudiness and less MLT-dependence of WIC opacity in Isidis. In addition, *Pearl et al.* [2001] stated in the caption for the plate: "An additional local cloud concentration is present in Syrtis Major Planitia, southwest of the lowlands of Isidis Planitia." Their results apparently contradict the cloud effect. However, the concepts is not necessarily inconsistent because (1) the MGS TES maps describes the clouds at single local time (1400MLT), (2) the cloud effect requires a differential variation of water ice cloud opacity.

Arabia is known as one of "thermal continents"; i.e., vast regions of high ground that have relatively high surface albedo and relatively low thermal inertia. The highland of Arabia includes (the westside part of) Syrtis Major, and the east rim of it makes a rather steep cliff along the limb of the eastern adjacent Isidis basin (see Figure 11.7).

On Mars, the horizontally variable thermal forcing can be produced by elevation differences, in that heat transferred from the ground has a larger effect on the thinner atmosphere above high ground. At lower levels, upland (lowland) regions are warm (cool) and have low (high) pressure, making rising (sinking) motion with adiabatic cooling (heating) [e.g., *Webster*, 1977; *Zurek et al.*, 1992]. The MGS TES opacity maps may probably reflect this mechanism. However, the situation is not so simple about diurnal variation problems. Because Syrtis Major is the

highest among the three region of interest, the atmospheric response is expected to be rapidest there. This effective response and the great cliff between Syrtis and Isidis will have nonlinear topographical effects on the diurnal variation.

Part IV

Dissipating Behavior of the Cloud Belt

Chapter 12

Paucity in Previous Studies

By analogy with Earth, planetary-scale cloud patterns on Mars are expected to reflect background meteorological/climatological phenomena. *Tamppari et al.* [2000] argued that there are "at least three types" of dynamical phenomena:

1. Global overturning of air known on Earth as the Hadley circulation should give cloudy (clear) zones in regions where solar heating of the surface and atmosphere produce rising (sinking) motion and its attendant adiabatic cooling (warming).

2. Orographic features like the Tharsis volcanoes and Olympus Mons can generate clouds as their greatly elevated terrain preferentially heats the atmosphere and draws air upslope, producing adiabatic cooling. Similar effects can also occur when air is forced upslope by regional weather.

3. Cold air masses that form in the wintertime middle and high latitudes are often marked by extensive cloudiness.

Revolutionary development of observation techniques/devices (including spacecraft) in the latter half of the 20th century allowed us to examine the appearance and activated behavior of the cloud belt. Few of the observational reports, however, have discussed its dissipating behavior.

Mars Global Surveyor was, fortunately, the most successful in the post-Viking missions mainly because of its lifetime. Among the instruments on board, the Thermal Emission Spectrometer (TES) made huge amount of unprecedented data, which contribute the atmospheric and surface environment. The "few" observation-based reports which discuss the dissipation of the cloud belt certainly include (and mostly consist of) MGS TES reports [e.g., *Pearl et al.*, 2001; *Smith et al.*, 2001]. Even the "most successful" reports could not avoid suffering from the orbital limitation; the observations were confined at certain local times (around 0200 and 1400 MLT) due to its orbit, in particular, after the aerobraking phase. Their accumulated data are lack of longitudinal information.

Although (few) HST observation reports also contribute to this issue [e.g., *James et al.*, 1994; *Wolff et al.*, 1999], they also have a fatal fault: the limit on the frequency of observations due to the small amount of time which can be allocated to any one project on the facility. HST may be able to observe with sufficient temporal constancy to monitor interseasonal and interannual changes. On the contrary, for the above-mentioned reason, the temporal continuity

which is necessary for monitoring a certain "intra-seasonal" event (regional dust storms, near-pole fronts/cyclones, large-scale cloud formation/dissipation processes, and more) cannot be sufficient.

Hence, our knowledge about the dissipating behavior has come mostly from theoretical methods. Most of their discussion is, however, based only on the meridional mean structure.

The paucity of reports on this dissipating event prompted us to investigate it, based on observations.

"So, how about ground-based observers? What have they made?"

There also is another cause of this paucity in ground-based observations. The spacecraft epoch had long been taking away the scientific "rights" from the ground-based planet observers, mainly because of the lower resolution, until the invention of CCD (charge-coupled device). Ground-based CCD photometry can have been the most suitable and realistic way and thus could have yielded considerable results. Why haven't? It is quite simple: the 2001 apparition was the first chance to observe the northern summer-to-autumn period of Mars after the birth of CCD and its accompanying technique (i.e., digital image processing on computers) became common, because of the 15 to 17-year periodicity to meet a particular Martian season.

The first half of the 2001 apparition corresponded to the northern late summer/early autumn on Mars. It was suitable for studying the dissipating behavior, and especially for studying the latitudinal coverage of the cloud belt, because we could observe Mars from "equator-on" views, that is, the sub-Earth point was almost on the equator in this apparition.

The results in this part are presented in *Nakakushi et al.* [2002a].

Chapter 13

Analyses and Results

13.1 Images

The analyses in this part concern the spatial distribution, appearance and disappearance of water ice clouds (WICs). The data of the images included are given in Table 13.1, featuring the visual states of water ice clouds.

Table 13.1: Image Data for Part IV.

Date	L_s	α^*	WIC state‡	Equip.*
1997 February 27	84	−14	*P*	H
1997 March 5	87	−10	*P*	H
1997 March 24†	95	6	*P*	H
1997 April 1	98	13	*P*	H
1997 April 12	103	20	*P* or *L*	H
1999 February 28†	104	−32	*P* or *L*	H
1999 March 16	111	−26	*P* or *L*	H
1999 April 20	127	−4	*P*	L
1999 April 27†	130	2	*L*	C1999
1999 April 30	132	5	*L*	H
2001 June 6	174	−7	*P*	C2001
2001 June 15†	178	3	—	C2001

Images with a dagger (†) are not included in figure 13.3.
* Phase angle in degrees (negative values indicate before opposition).
‡ Apparent states of the low-latitude water ice cloud(s). *P*: planetary encircling, *L*: localized, blank(—): not identified.
* Observational equipment listed in Table 3.1.

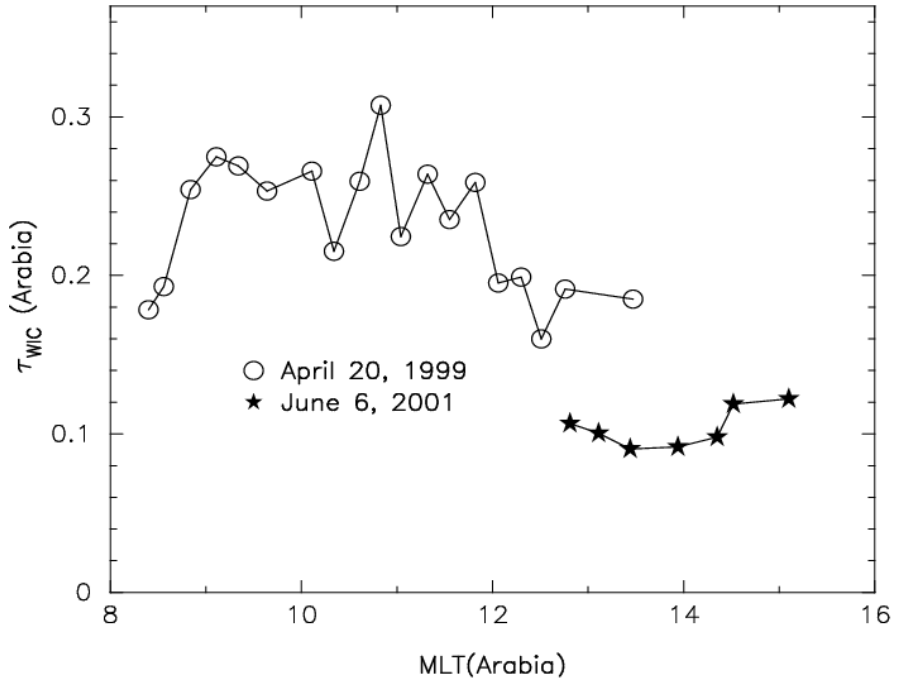

Figure 13.1: Diurnal variations of $\tau_{\rm WIC}$ in 1999 and 2001.

13.2 Seasonal Dependence of the Water Ice Cloud Opacity Diurnal Variations

13.2.1 Phase Functions and Parameters

Our $\tau_{\rm WIC}$-estimation algorithm[1] is based on the "discrete-ordinate" method. Parameters adopted here were as follows; the Minnaert exponent, $k_{\rm M} = 0.53$ [*Erard*, 2000, for small phase angles]; the ground normal albedo, $A_n = 0.06$ [*Akabane et al.*, 1987]; the opacity of CO_2 atmosphere, $\tau_{\rm CO_2} = 0.01$ [*Wells*, 1979]; the dust opacity, $\tau_{\rm dust} = 0.3$ [*Clancy et al.*, 2000; *Akabane et al.*, 2002]. All these values, and also hereafter, were treated as those in blue ($\lambda \simeq 4400$Å) according to our observations. The phase function for water ice particles used here was that of *Clancy and Lee* [1991]. In this paper, the region of interest on this $\tau_{\rm WIC}$-estimation is Arabia, centered at (315°W, 10°N). For further details and other information, the reader may refer to our previous papers, where it was also demonstrated that the constancy of $\tau_{\rm dust} = 0.3$ does not greatly affect the opacity estimation of water ice clouds [e.g., *Nakakushi et al.*, 2001a; *Akabane et al.*, 2002, and references therein].

13.2.2 Retrieved Water Ice Cloud Opacities

We present, in this section, results of measuring the water ice optical thickness in blue light. We define here a cloud "*belt*" as wholly encircling the tropics, and a cloud "*band*" as a cluster of water ice clouds covering broad areas of the tropics.

[1]Hereafter, we change the symbol set for opacities ($\tau_{\rm R}$, $\tau_{\rm D}$, $\tau_{\rm H}$) into ($\tau_{\rm CO_2}$, $\tau_{\rm dust}$, $\tau_{\rm WIC}$). This is only for visual simplicity.

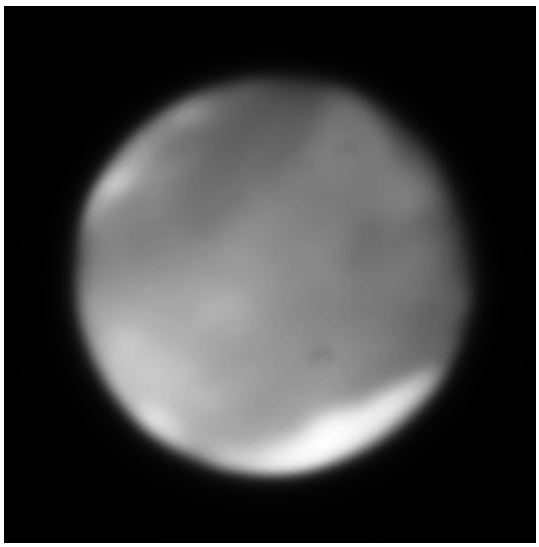

Figure 13.2: Sample image taken on 2001 June 6. A faint, broad cloud band can be seen (the sub-Earth point longitude is 33°W). The contrast is slightly enhanced.

Figure 13.1 depicts the derived diurnal variation of $\tau_{\rm WIC}$ on June 6, 2001 ($L_s = 174°$). Figure 13.2 is a sample image. For comparison, results from similar calculations for April 20, 1999 ($L_s = 127°$) were included in the figure. The WIC band on this day can be seen in Figure 8.1.

The WIC opacities at $L_s = 174°$ in Figure 13.1 are much smaller than at $L_s = 127°$. The factor is $\sim 1/2$ at around 1300MLT. Although these results show that the cloud band was significantly weakened at $L_s = 174°$ in 2001, we emphasize here the existence itself of the cloud band of moderate dimension (as seen in Figure 13.2) with $\tau_{\rm WIC} \approx 0.1$ as late as at $L_s = 174°$. *Smith and Lemmon* [1999] also showed presence of water ice cloud(s) during the Mars Pathfinder mission ($L_s = 142°$-$188°$ in 1997). However, their result doesn't imply the presence of the WIC *belt* (nor *band*) as shown in Figure 13.2. A reanalysis of Viking data sets [*Tamppari et al.*, 2000] also shows evidence for clouds in the equatorial region between $L_s = 110°$-$170°$, though the spatial coverage of the data is not complete.

13.3 Latitudinal Coverage of the Cloud Belt

There have been several works which indicate that the aphelion cloud belt usually covers the tropical zone of 30°N-10°S [e.g., *Clancy et al.*, 1996; *Tamppari et al.*, 2000]. We examined the L_s-dependence of latitudinal distribution of the cloud band using the images obtained in these three apparitions: 1997, 1999, and 2001. The presence of water ice clouds can be discerned in blue (violet)-filtered images. We first obtained the brightness distribution of each image. For this analysis the data points used were confined within 1100-1300MLT (i.e., around the sub-solar point), that is, we neglected the dependence of WIC distribution on topography. The grid-point spacing was 3° by 3°. These brightness data were then longitudinally averaged. The averaged brightness data were plotted as a function of latitude. Finally, we defined the latitude which gave the maximum second-order differential of the brightness curve as the "northern/southern limit latitude."

The obtained L_s-dependence of the northern and southern limit latitudes of the cloud band

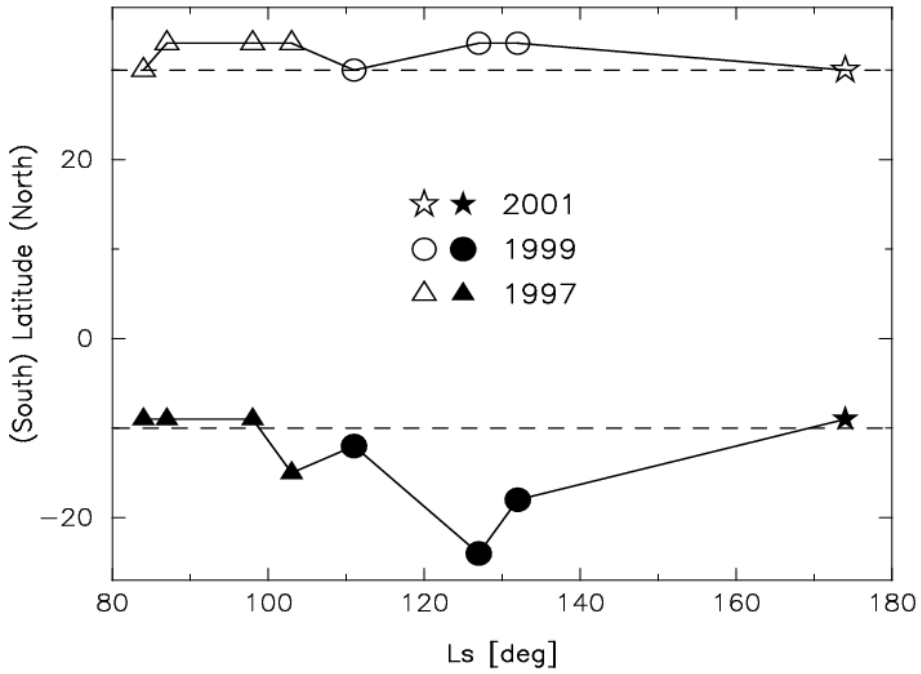

Figure 13.3: Northern and southern limits around local noon versus areocentric solar longitudes (L_s). The dashed lines at 30°N and 10°S show those suggested by *Clancy et al.* [1996].

(belt) is presented in Figure 13.3. The northern limit of the cloud band does not show significant L_s-dependence, while the southern one expands around L_s∼120°-130°. This southern limit expansion, however, may be due to low resolution on the observations, and/or due to the inclination of the Martian rotation axis to Earth, in the 1999 apparition. However, we note that the latitudinal coverage of the band shows no significant "shrinking" toward the dissipation. This suggests that the cloud band has a minimum latitudinal dimension. *Wolff et al.* [1999] suggested that the band's dissipation occurred at $L_s \sim 146°$ in 1997. While they laid it down that the trend is clear, the seasonal distribution of the data in their paper is not well sampled near the equinox. *Smith et al.* [2001] suggested that it occurred near $L_s = 145°$ in 1999. Both saw clouds between 30°N and 10°S. In the 2001 apparition, the public image of Mars taken with HST on June 26 with the 410nm filter apparently suggests that the bands no longer existed by $L_s \sim 185°$ (press-released HST images, including this image of Mars, are available from the World Wide Web server for the Space Telescope Science Institute (STScI) at http://www.stsci.edu/resources/). We could not find any significant low-latitude cloud belt/bands in our images at $L_s = 178°$ (June 15, 2001). Comparison of Figure 13.3 to these solar longitudes of dissipation for each year suggests that the band (belt) had never reduced its dimension to under the 30°N-10°S latitudinal range until its end.

13.4 Longitudinal Division of the Cloud Belt

On April 27, 1999 ($L_s = 130°$), the planetary encircling WIC belt had divided into a "semi-encircling" band (which appears to be "led" by the Elysium orographic cloud) and a discrete cloud centered at around (170°W, 10°N), southwest of Amazonis (see Figure 13.4), whereas some

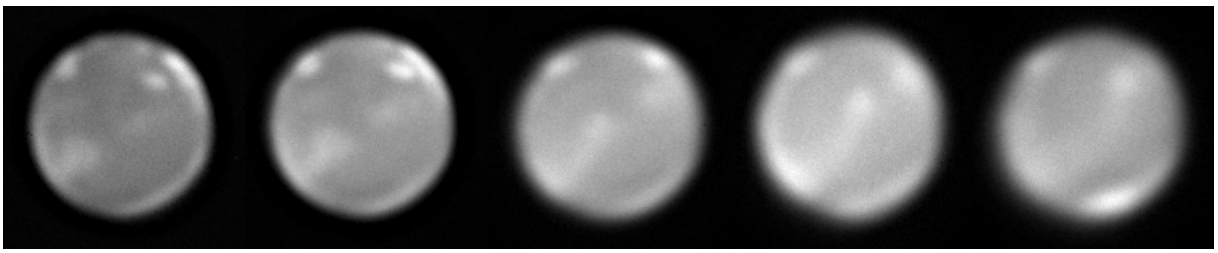

Figure 13.4: Images on April 27, 1999. The upper-left direction is north on Mars. The longitudes of the sub-Earth point (LON_{SE}) are 181°W, 191°W, 212°W, 232°W, and 256°W, respectively (left to right). Within the image of $LON_{SE} = 181°$W, we can see a large orographic cloud over Elysium in the morning side, a large faint cloud near Amazonis on early afternoon (near 180°W), a bright Olympus orographic cloud in the evening, and a bright water-ice-cloudy zone on the dusk limb. The water ice cloud band is (or appears to be) led by the Elysium cloud(s).

orographic clouds were present. Our images taken on February 28, 1999 ($L_s = 104°$), the daytime infrared WIC opacity maps by MGS TES (Plate 2a of *Pearl et al.* [2001] for $L_s = 106°$-$141°$ and Plate 4 of *Smith et al.* [2001] for $L_s = 104°$-$140°$) show a similar situation.

This $L_s = 104°$ period is the time when the cloud belt (or cloud bands) should show its (their) strong (maybe strongest) activity. An HST cylindrical map image [e.g., *Clancy et al.*, 1996] presents the cloud belt in its mature state at $L_s = 68°$ in 1995. We notice less cloudiness around 180°W on the HST map image, though no corrections for cloud limb brightening had been applied to the map. Our images at $L_s = 95°$ (March 24, 1997) also show the mature cloud belt even around the Amazonis area [*Akabane et al.*, 1999, Figure 2]. Plate 3 of *Tamppari et al.* [2000] suggests the presence of the belt/bands/clouds until $L_s \sim 120°$–$140°$. Moreover, though they did discuss clouds associated with topography, their results still need closer investigations in terms of this issue of the WIC division/dissipation behavior. Although we can not apparently identify the bands in our images on June 15, 2001 ($L_s = 178°$) due to their being too faint and/or due to the occurrence of the blue clearing in the Syrtis Major region, there might remain a faint, but modestly large, cloud over Arabia with a similar latitudinal dimension.

Chapter 14

Discussions and Remarks

14.1 Dissipation Process and Local Hadley Cells

The directly inferred dissipating behavior is summarized as follows:

(1) The cloud belt is already in its full-encircling mature state by $L_s = 84°$, and so continues the state until $L_s \sim 100°$.

(2) The belt gradually divides into semi-encircling band(s) and discrete cloud(s) around $L_s \sim 100°$–$110°$.

(3) The clouds/cloud bands fade away towards the equinox without prominent latitudinal shrinkage.

Many theoretical studies have predicted a cross-equatorial Hadley cell from the summer hemisphere to the winter hemisphere in seasons including the solstices [e.g., *Haberle et al.*, 1993]. *Clancy et al.* [1996] suggested that the northern summer ascending branch of this cross-equatorial Hadley cell is embodied in the low-latitude cloud belt (see the next section). Our Figure 13.3 therefore indicates that the Hadley cell keeps its minimum dimension at least while the cloud band is alive. The division (or "discretization") of the cloud band pointed out above may imply localization of the Hadley circulation. Local Hadley cells are also suggested on Earth (Japan Meteorological Agency 2001; see Figure 14.1), though their properties and causes may probably be different from the expected Martian ones, certainly because at present Mars do not have oceans.

Then, what are the local Hadley cells on Mars?

One possible (and somewhat reasonable) interpretation is disturbance by superimposed large-scale thermal tides and waves. However, this thesis do not intend to extend this unpublished idea. Some further insights will be introduced as one of future prospects in Chapter C.

14.2 Suspected Relation with Global Dust Storms

In the 2001 apparition, the cloud belt was alive at $L_s = 174°$ with $\tau_{\mathrm{WIC}} \approx 0.1$, and its end was around $L_s \sim 180°$. This persistence into the northern autumn is later than most observational records. Reportedly, a global dust storm rose from the Hellas Basin just after the belt's/band's dissipation ($L_s \sim 180°$–$190°$) in 2001 [e.g., public GIF images from MGS TES, personal communication with Christensen et al. of Arizona State University]. This seems unusually early for

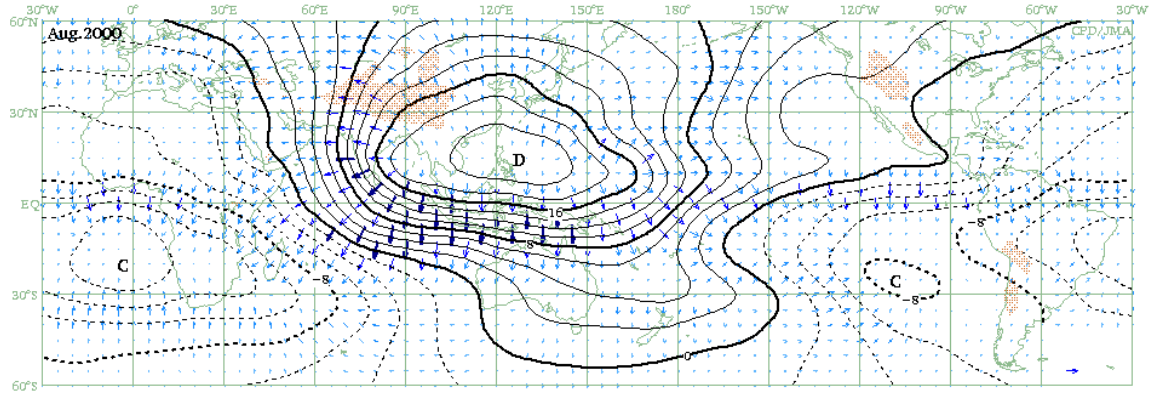

Figure 14.1: Monthly mean (2000 August) 200 hPa velocity potential (contours) and divergent wind vector (blue arrows) on Earth [*Japan Meteorological Agency*, 2001]. The divergence and convergence are represented as "D" and "C", respectively, in units of 10^6 m^2s^{-1}. The longest arrow indicates 4 ms^{-1}. Since the 200 hPa level corresponds to that near the tropopause on Earth, the divergence (convergence) zones can be regarded as the rising (sinking) branches of the Hadley cells.

large-scale dust storms. The storm became the largest in several decades and it wrapped the entire planet for several months. These facts urge us to hypothesize that there is some connection between the strong and long-lasting activity of the WIC bands in the 2001 northern summer and the strong and long-lasting activity of the dust storm. An investigation of this relationship will be a part of future studies in order to clarify the interannual and seasonal variations of the Martian climate.

Part V

Summary

Chapter 15

Concluding Remarks

Water ice clouds on Mars have many aspects. They directly and indirectly affect the Martian climate, as they change themselves in various forms. This thesis is intended to contribute toward our understanding of the various and complicated behaviors of water ice clouds. In this chapter, we summarize the conclusions presented in the previous parts, with some further discussions.

15.1 Opacity Estimation Method

Since *Akabane et al.* [1987], our group has been developing algorithm to solve the radiative transfer equation. Finally we have established the water ice cloud opacity estimation method on our own, which employs the discrete ordinate method [e.g., *Chandrasekhar*, 1960; *Liou*, 1973, 1980], the matrix method [*Stamnes and Swanson*, 1981; *Stamnes and Dale*, 1981; *Stamnes et al.*, 1988, 2000], the δ-M method [e.g., *Wiscombe*, 1977], and the regional-mean method [e.g., *Nakakushi et al.*, 2001a]. The total and close description of it presented in Part II is the first one in history. The regional-mean method (in Sections 9.2 and 9.3, depicted in Figure 9.1) is a significant contribution by the author, which brings ground-based telescopic imaging observations up to a comparable approach to other modern techniques. The author hopes this would help all the Mars observers that are interested in atmospheric phenomena.

We modeled the Martian atmosphere as consist of CO_2 background atmosphere, suspended dust, and water ice clouds. The key points are the reference points (RPs) instead of reference stars for intensity calibration, and the assumption of the constant opacities of all the other atmospheric constituents. Although the constancy of dust opacity in particular might seem questionable, our calculations suggest that the difference in the value of constant dust opacity does not matter significantly. Furthermore, the suppress of atmospheric dust amount by water condensation (i.e., nucleation) within the season of active water ice clouds, which is expected to reduce the dust contribution(s), makes it more acceptable. In addition, if we fix the water ice cloud opacity (in most cases of interest, $\tau_{\rm WIC} \sim 0$) instead of the dust opacity, we can derive the dust opacity through the same algorithm. Moreover, if the region of interest on the Mars surface lies under a "clear" atmosphere, the optical thicknesses of both aerosols can be assumed to be zero, which enables us to investigate surface scattering properties.

There are some places to improve in our modified δ-M DOM. The "regional-mean" method will be improved by a new statistical method known as the "Latin square method." This improvement shall be achieved in the next work. Closer investigations of the dependence of $\tau_{\rm dust}$ on wavelength will give more appropriate value of $\tau_{\rm dust}$ for the assumption of constancy in our modified δ-M DOM. In addition, we will continue finding another place awaiting improvement;

this never-ending progress should promise us more fruitful observations of Mars.

15.2 Blue Clearing

In Part III, this thesis presented a radiative transfer analyses of 1997 and 1999 ground-based Mars violet images, towards a quantitative explanation of the so-called "blue clearing" phenomenon reported intermittently in ground-based telescopic monitoring of Mars.

Normally the surface of Mars has a fairly constant albedo at short wavelengths, but occasionally a dark region such as Syrtis Major "pops out" in contrast to surrounding areas. We derived quantitative estimates of optical depths in Arabia, Syrtis Major, and Isidis, and correlate these with the contrast differences linked to the blue clearing. The image data and radiative transfer employed in this analysis indicate that water ice clouds can contribute substantially to the blue clearing phenomenon.

We regard this diurnal contrast enhancement as a consequence of water ice clouds and also propose their optical effect on the apparent contrast between bright (Isidis and Arabia) and dark (Syrtis Major) surface regions on Mars. It is implied that the recently re-identified low-latitude seasonal cloud belt, which is tied to the aphelion northern summer season, leads to the time-variable nature of blue clearings in the historical record of Mars telescopic observations. In order for a particular region, such as Syrtis, to appear dark, a differential variation of optical depth with time is required, else each area would appear dark as it reached noon local time. Thus we ascribe the diurnal effect to the diurnal variation in the clouds in the seasonal equatorial cloud belt. The manner in which the water ice clouds affect this phenomenon is quantitatively revealed for the first time, and named "cloud effect." Our data, through regression analyses, suggest that a larger decrease in optical depth over Syrtis Major is the culprit.

15.3 Complete Story of the Low-Latitude Cloud Belt

After the appearance of orographic clouds over high mountains in northern spring, morning and evening clouds are formed in the late spring. The morning clouds fade away in the daytime at first. Thereafter, their persistence becomes gradually prominent. The global ascending motion according to the cross-equatorial Hadley circulation will support the persistence, resulting in the full formation of the low-latitude cloud belt which locates in the tropics of 10°S-30°N. The cloud belt keeps its development thereafter, and the belt reaches maximum extent around $L_s = 80°$-$110°$. From the analyses of the degree of blue clearing D and the water ice cloud opacity $\tau_{\rm WIC}$ in 1997 and 1999 (in Part III), we find that the morning clouds are most active around 0900 MLT in this mature state of the cloud belt. Such developing and mature stages have recently been well-documented in contrast to the dissipating phase.

Part IV in this thesis intends to remedy this scientific paucity. We examined the latitudinal and longitudinal structures of the cloud belt and their seasonal variations using the image data obtained in the most recent three apparitions (1997, 1999, and 2001), approaching both from the similar radiative transfer analyses and from the brightness distribution on the images. Our data suggest that the latitudinal coverage of the cloud belt does not reduce until its dissipation. We found that the cloud belt in its dissipating phase divide into some portions, i.e., cloud bands and localized clouds of large dimension. We attribute this cloud division to the localization of the background cross-equatorial Hadley cell. In addition, we observed that the cloud belt in 2001 dissipated unusually late, and just before the reported global-scale dust storm beginning at $L_s \sim 180°$ from the Hellas basin, the beginning of which is considered to be rather early. We suggest

that the unusually late disappearance of the cloud belt and the unusually early appearance of the dust storm may imply a relation between the two global-scale striking phenomena due to irregular Martian climatological conditions like those inferred from the 2001 observations.

On Mars, atmospheric cloud science in the modern manner have been just begun. The presented works in this thesis therefore need to be assured by further investigations via all approaches available, of course. In any case, our observational studies on water ice clouds will provide constraints for theoretical investigations involving cloud microphysics and global circulation models. The impact of these results will lead to more faithful models and a better understanding of the phenomena in Mars' atmosphere.

Appendix A

List of Symbols

The descriptions in Part II follow the notation below. Related equation numbers are also indicated.

Symbol	Meaning	Equation(s)
a_i, a_j	ith or jth weight of Gauss-Legendre quadrature (precedently known)	4.12
A_{M}	Minnaert albedo	5.7, 5.17
A_n	normal albedo	5.17
C_{ij}^m	coefficient	4.15
f	truncation fraction in the δ-M method	6.8
F_0	solar incident flux divided by π	4.1
$\boldsymbol{g}^{\pm}$	eigenvectors	4.18
I	diffuse intensity	4.1
$\boldsymbol{I}^{\pm}$	vectors containing the intensity components $I_i^m = I^m(\tau, \mu_i)$	4.17
I^m	mth Fourier component of intensity I	4.9
J	formal function in Eq. (4.26)	4.27
J^m	discrete component for J	4.28
k, k_j^m	eigenvalues	4.18, 4.23c
k_{M}	Minnaert index (exponent)	5.7
l	expansion index/order	4.2b
L_j^m	coefficient determined by boundary conditions	4.24, 5.28a, 5.28b
m	expansion index, azimuthal order	4.5, 4.9
M_j	constant for manipulation	5.20
n	integer indicating the maximum order in the Legendre expansion	4.2b
N_j	constant for manipulation	5.20
p	scattering phase function	4.1
p^*	approximated scattering phase function	6.8
P_l	Legendre polynomials	4.2b

P_l^m	associated Legendre polynomials	4.5
R	Minnaert reflectance function	5.7, 5.4
$W_j^m(\mu)$	Liou's W-function for an arbitrary angle μ	4.35
$W_j^m(\mu_i)$	ith component of Liou's W-function	4.22
Z_0^m	Z-function for the particular solution	4.24, 4.25
α	phase angle (Earth-Sun-Mars)	5.17
$\boldsymbol{\alpha}$, α_{ij}	coefficient matrix and its component	4.16a, 4.17
$\boldsymbol{\beta}$, β_{ij}	coefficient matrix and its component	4.16b, 4.17
β_j^0	constants for manipulation	5.14, 5.18
β_e	extinction coefficient	6.5
β_s	scattering coefficient	6.5
$\delta_{i,j}$	Dirac's delta	
$\delta(x)$	Dirac's δ-function	
ϵ^m	constants for manipulation	5.14, 5.18, 5.25
θ, θ'	zenith angles	4.4
Θ	scattering angle	4.4
μ	cosine of the emergent angle	4.1
μ_0	cosine of the solar zenith angle	4.1
μ_i	ith discrete ordinate, ith zero-point for Gauss-Legendre quadrature	4.11a
τ	normal optical thickness	4.1
τ_{N}	normal optical depth at the ground surface	4.26, 6.6c
ϖ_l	lth moment of Legendre expansion	4.2c
ϕ, ϕ'	azimuth angle	4.1, 4.4
ϕ_0	solar azimuth angle	4.1
$\Phi(\alpha)$	ground phase function	5.7
χ_l	same as ϖ_l	4.2c
ψ	normalized scattering phase function	6.1a
ψ	approximated and normalized scattering phase function	6.8
ω_l	normalization factor	6.1a

Appendix B

Scattering Properties of Water Ice Particles

B.1 Calculation with Mie Theory

Although the real particles are non-spherical, the classical Mie scattering theory for spherical particles is sufficiently useful in order for us to understand the synoptic optical behavior of water ice particles owing to the particle size parameter of the airborne water ice particles of $X \sim 1$ within the wavelengths under study. The size parameter is so defined as

$$X = \frac{2\pi a}{\lambda}, \tag{B.1}$$

where a is the radius for a spherical particle; for a non-spherical particle a is the equivalent particle radius, defined with its geometric cross section[1] σ as

$$a = \sqrt{\frac{\sigma}{\pi}}. \tag{B.2}$$

With this definition the power absorbed by an optically thick irregular particle is equal to that absorbed by its equivalent sphere.[2]

To calculate the Mie scattering quantities, all we need are the complex index of refraction of the particles of interest,

$$m = n_r - in_i, \tag{B.3}$$

and their differential size distribution function $dn(r)/dr$, in the latter r is the radius of the particles. The function $n(r)$ implies the volume concentration at the radius r. For water ice particles, the modified gamma function [e.g., *Deirmendjian*, 1964] is often applied;

$$n(r) = Cr^{\alpha} \exp\left\{-\frac{\alpha}{\gamma}\left(\frac{r}{r_m}\right)^{\gamma}\right\}, \tag{B.4}$$

[1]The "geometric cross section" depends on the particle orientation. Because we only treat bulk scattering media finally and there are no orientating forces in the situation of interest, in this thesis we always assume that we are dealing with ensembles of particles whose orientations are random. Thus, the geometric cross section σ of a particle is the average area of the geometric shadow cast by the particle as it is oriented at random in all directions.

[2]If the effective radius a for a non-spherical particle is defined to be the radius of a sphere of the same volume as the particle, as appearing in some references, the situation for the absorbed power is different. Please see [*Hapke*, 1993, chap. 6] for detail.

where C is a constant of proportionality, α and γ are adjustable parameters, and r_m is the mode radius of particles. C, α, and γ are positive. This size distribution function $n(r)$ is normalized such that

$$\int_0^\infty n(r)dr = N, \tag{B.5}$$

where N is the total number of particles per unit volume. The constant C is derived from this normalization condition with the gamma function,

$$\Gamma(x) = \int_0^\infty t^{x-1}e^{-t}dt. \tag{B.6}$$

By replacing

$$t = br^\gamma \tag{B.7}$$

and

$$b = \frac{\alpha}{\gamma \cdot {r_m}^\gamma} \tag{B.8}$$

we readily obtain

$$\begin{aligned} N &= \frac{C}{b^{\frac{\alpha+1}{\gamma}}\gamma}\int_0^\infty b^{\frac{\alpha+1}{\gamma}}\gamma \cdot r^\alpha \exp(-br^\gamma)dr \\ &= \frac{C}{b^{\frac{\alpha+1}{\gamma}}\gamma}\int_0^\infty (br^\gamma)^{\frac{\alpha+1-\gamma}{\gamma}} \exp(-br^\gamma)\cdot b\gamma \cdot r^{(\gamma-1)}dr \\ &= \frac{C}{b^{\frac{\alpha+1}{\gamma}}\gamma}\int_0^\infty t^{\frac{\alpha+1}{\gamma}-1}e^{-t}dt \\ &= \frac{C}{b^{\frac{\alpha+1}{\gamma}}\gamma}\Gamma\left(\frac{\alpha+1}{\gamma}\right), \end{aligned} \tag{B.9}$$

and

$$C = \frac{Nb^{\frac{\alpha+1}{\gamma}}\gamma}{\Gamma\left(\frac{\alpha+1}{\gamma}\right)}. \tag{B.10}$$

The total number density N, however, has not been given yet. To estimate the optical properties of our interest here, the constant is not required (but required formally within the calculation program, although all the appearing C are vanished), so that we arbitrarily chose the form which does not depend on N;

$$C' = \frac{b^{\frac{\alpha+1}{\gamma}}\gamma}{\Gamma\left(\frac{\alpha+1}{\gamma}\right)}. \tag{B.11}$$

B.2 Refractive Index and Single-Scattering Albedo

Figures B.1 and B.2 are the input real and imaginary part, respectively, of the refractive index. These numerical data are the improved version complied by W. Wiscombe (this dataset is in public on his FTP site, ftp://climate.gsfc.nasa.gov/pub/wiscombe/) based on the compilation of *Warren* [1984]. Close-up views in the 0.3-1.0μm wavelengths are Figures B.3 and B.4.

The imaginary part n_i, equivalent to the absorption coefficient, varies in a considerably wide range compared to the real part n_r.

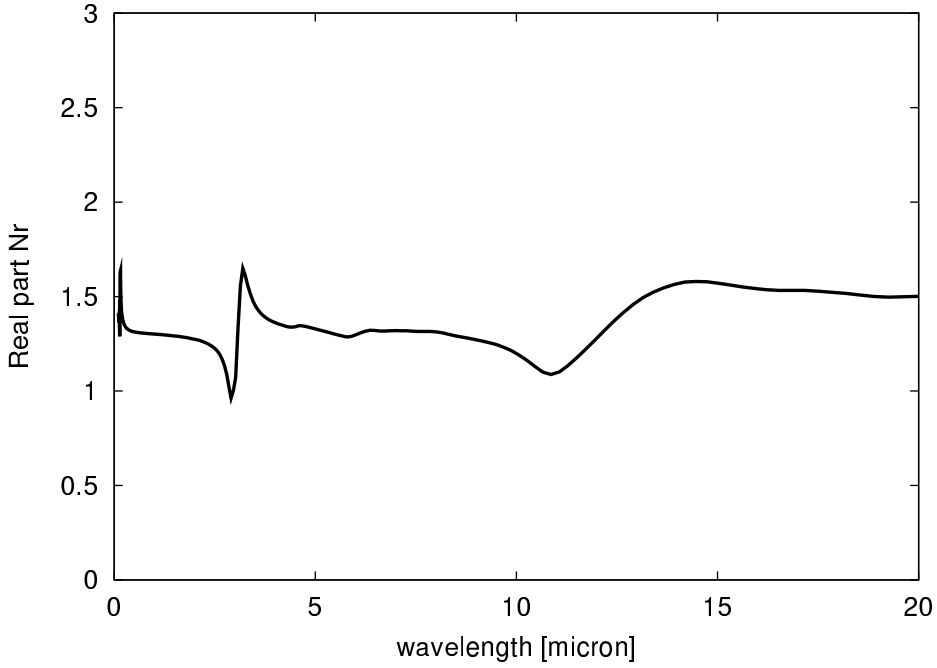

Figure B.1: The real part of the complex refractive index of water ice particles.

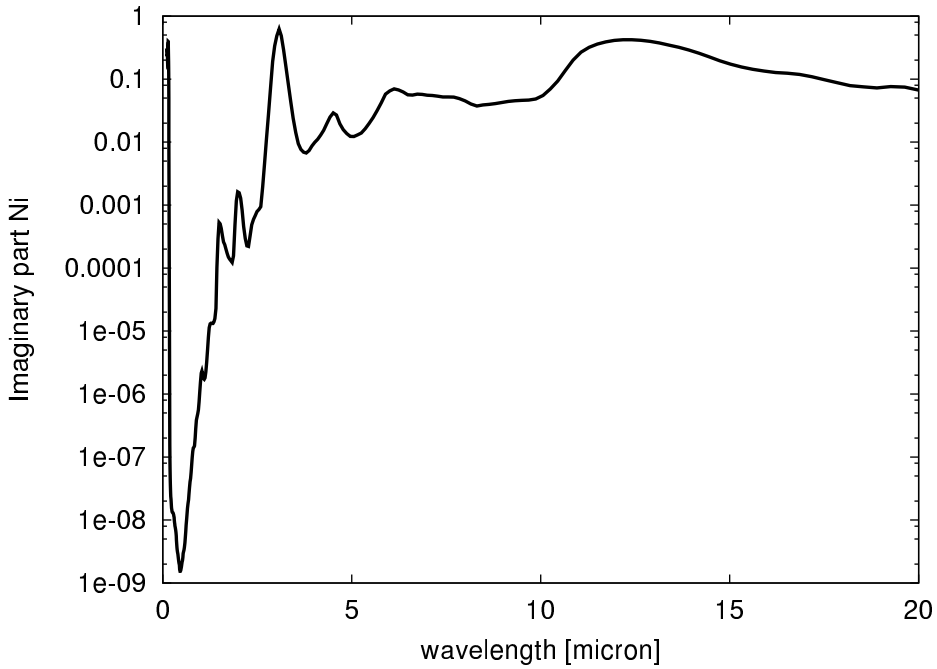

Figure B.2: The imaginary part of the complex refractive index of water ice particles. Note that the vertical coordinate is in log scale.

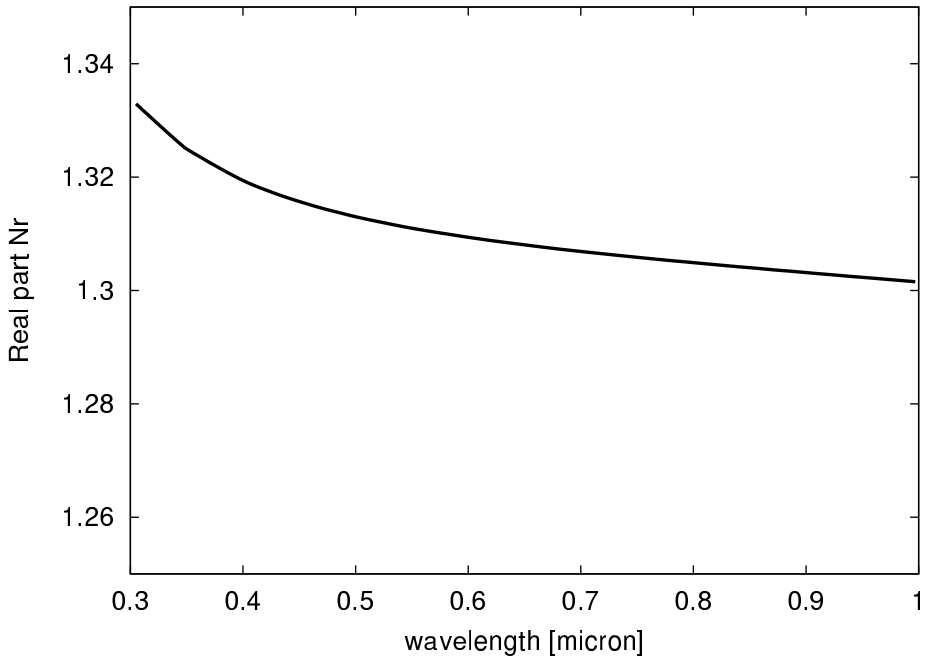

Figure B.3: A close-up view of Figure B.1 for 0.3μm to 1.0μm.

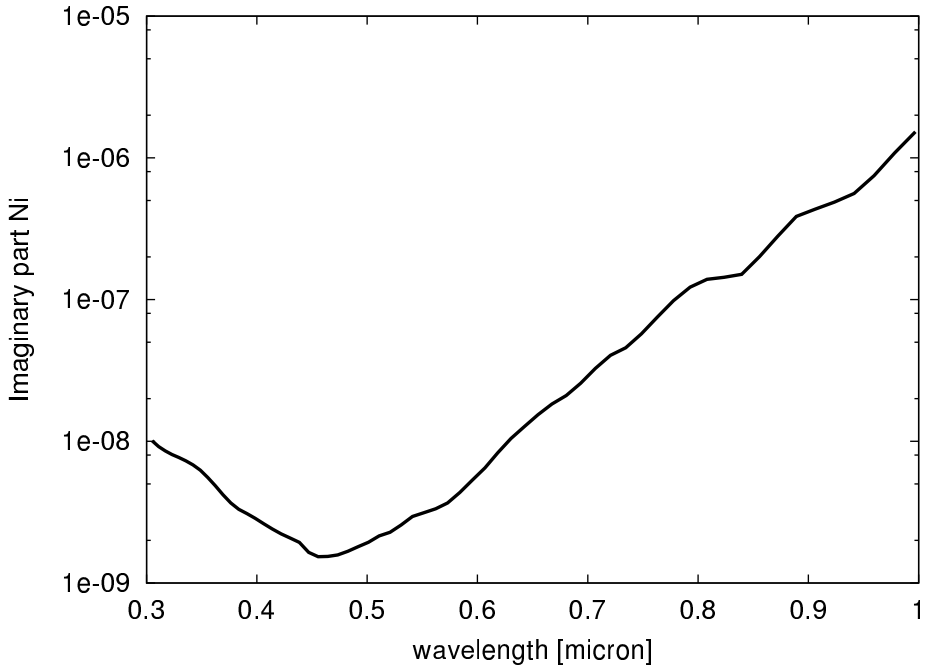

Figure B.4: A close-up view of Figure B.2 for 0.3μm to 1.0μm. Note that the vertical coordinate is in log scale.

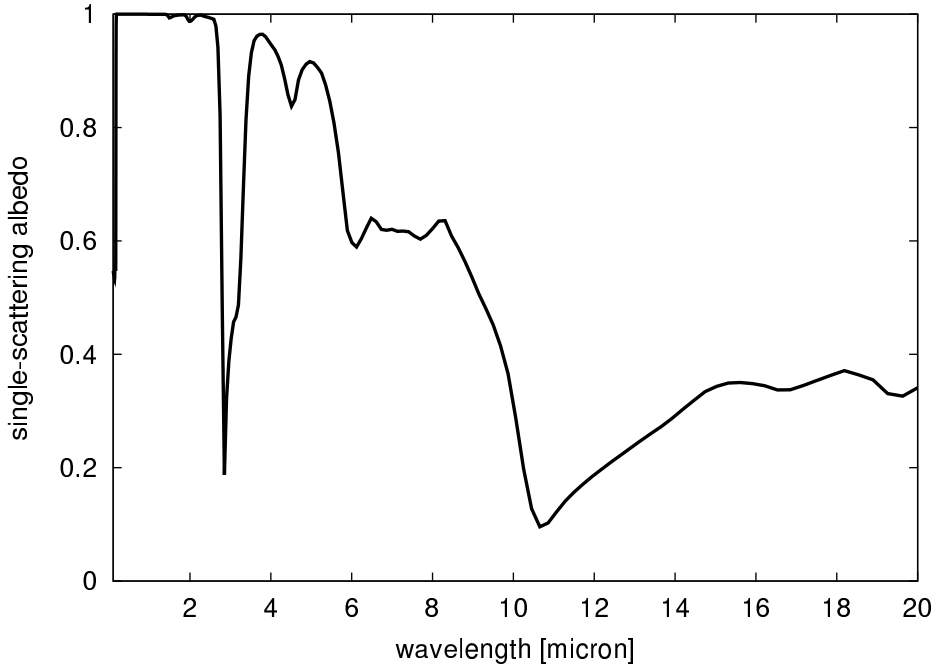

Figure B.5: Single scattering albedo of water ice particles derived from the Mie calculation for 0.1-20μm.

To evaluate the visibility of atmospheric water ice clouds, the most useful optical property is single-scattering albedo, which is defined as the ratio of the scattering efficiency to the absorption efficiency [see Eqs. (6.5)]. We thus calculate here the dependence of water ice single-scattering albedo as a function of wavelengths. The calculation code is based on the FORTRAN program used in *Hansen and Travis* [1974] arranged and adjusted by K. Kawabata, Y. Narumi, and T. Nakakushi. Input parameters followed the Mariner 9 estimates by *Curran et al.* [1973]: $\alpha = 8.0$, $\gamma = 3.0$, and $r_m = 2.0$.

Figure B.5 is the result of our calculation according to Figures B.1 and B.2. In shorter wavelengths, the manner in which the derived single-scattering albedo depends on wavelengths is conspicuously affected by the imaginary part of the complex refractive index, rather than the real part. It is quite obvious in a close-up view (Figure B.6) that the derived single-scattering albedo of water ice particles considered is almost unity independent of wavelength in the visible band. This is due to the low imaginary part of the complex refractive index.

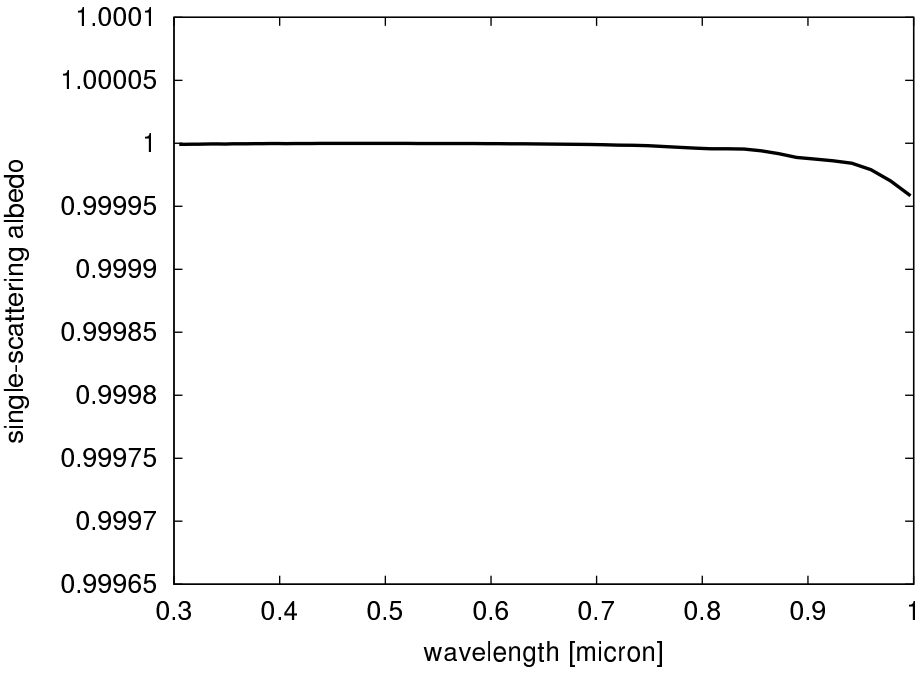

Figure B.6: A close-up view of Figure B.5 for 0.3-1.0μm.

Appendix C

Possible Extensions Ahead

We can extend the ground-based telescopic studies on Martian water ice clouds toward many directions. In this chapter we introduce our ongoing developments concerning this line of study. Away from supports for future spacecraft missions, there are many interesting scientific topics along the way ahead: suspected water ice particles in dust storm seasons, the effect of radiative cooling by water ice clouds on atmospheric temperature structure, the relationship among the polar caps, the polar hoods, the seasonal cloud belt, and the recently identified subsurface water (i.e., search for a total description of water cycle on Mars), and so on. Among those objectives, we focus these three in this chapter: observability of thermal tides and waves, surface properties, and data assimilation.

C.1 Observability of Thermal Tides and Waves

C.1.1 The True Character of the Local Hadley Cells

In Chapter 14, we stated that the suggested local Hadley cells and the corresponding cloud division may embody the prominence of thermal tides and waves. From this standpoint, the stable morning clouds may be interpreted as the westward migrating sun-fixed (or "sun-synchronous") wave; it is not possible to distinguish between stationary waves and non-migrating thermal tides or isolate the sun-synchronous tide from data MGS TES in the mapping orbit, because the mapping orbit is fixed on the fixed local time (about 0200 and 1400MLT) [e.g., *Wilson*, 2000]. Although MGS TES might be able to detect them in the aerobraking and science-phasing orbit (and did it actually [*Banfield et al.*, 2000]), the situation was not good for this issue, unfortunately (for example, $L_s = 180^\circ$ to 30° in the next Martian year and southerly poleward of 30°, in *Banfield et al.* [2000]). On the other hand, the divided cloud bands are to be interpreted as the stationary topography-fixed wave, which may be detected by TES in the mapping orbit [e.g., *Smith et al.*, 2001]. However, we cannot give any direct implication on this issue from the insufficiently accumulated results and discussions on waves, for example, presented in *Smith et al.* [2001]. More unfortunately, studies on tidal waves on observational bases have not so much (or rarely) been accumulated. For another basis, theoretical methods (i.e., GCMs) have still had some difficulties to include the effect of tides, topography, and phase changes of water, which are inevitable for this issue of the localized cloud bands, as yet.

The localized cloud cluster in the southwest of Amazonis showed in Section 13.4 is not so distinct on Plate 4 of *Smith et al.* [2001], while Plate 2a of *Pearl et al.* [2001] showed it. This cloudiness covered the longitudes of about 140° - 180°, which corresponds to the vast lowland between Elysium and Olympus, so that the cloud contrast in this area is expected to be

generated by a different mechanism from the less cloudiness in the Syrtis Major region discussed in Section 11.3. *Smith et al.* [2001] also showed a map depicting the horizontal variation of atmospheric temperatures at 1.36 mbar during a 5-sol period centered at $L_s = 135°$ on their Plate 8. The 1.36-mbar level corresponds to the highest layer of the troposphere. Their map shows a topography-fixed weak planetary-scale wave of wavenumber 2 in the tropics. On the map, although no solitary feature in the Syrtis Major region, this may imply that the effect of the "particular" dynamics there should be confined within low altitudes and it could not propagate up to such high altitudes. That may be attributed to the time-of-day-fixed observation (0200 and 1400MLT) in the mapping orbit of MGS. A similar analyses for the middle troposphere may reveal the situation. The map tells us that Syrtis Major was in a cooler zone (phase) of the wave, and that a warmer zone (phase) were present around 180°-200°W. The latter warmer zone is expected to have formed the less cloudiness in the west of the southwest-of-Amazonis cloud. However, other cloud *formations* and suspected localized Hadley cells cannot be explained by the only map of *Smith et al.* [2001]. The link of atmospheric physics with topography is a non-linear process (the Syrtis Major problem may be one of the most difficult case), which do not allow us to diagnose the problem simply by observations, even if it may be brought by spacecraft. We needs other clues, such as studies of *dynamics* with a GCM which will reproduce the longitudinal structure and variations.

C.1.2 The Wave Mode

As introduced in Section 2.3.3, T. Akabane and his collaborators proposed that most clouds in the late morning to the early afternoon parts of the cloud belt may be morning clouds that are reduced in brightness and optical thickness but still are visible and recover their brightness in the mid to late afternoon as evening clouds, which is the mechanism to form the cloud belt in their context. Because the Martian atmosphere is, fundamentally, quite stable and usually close to saturation, clouds will be able to persist in the atmosphere once they form. The processes to evaporate the remains of these clouds may be atmospheric divergence, adiabatic heating due to downward motions, and daytime solar heating (needless to say, the three do not have to occur concurrently). Even if any, the background upward motions due to the cross-equatorial Hadley circulation may keep the clouds in daytime from evaporation during northern summer. Horizontal winds are negligible compared to the rotation. In the season and the latitudes of interest, the horizontal winds are easterlies near the ground. They are not strong at all, of 10 ms^{-1} at most [e.g., *Haberle et al.*, 1993; *Smith et al.*, 2001]. Overall, the tide-based hypothesis of this thesis does not conflict with the "midday remainder" concept of Akabane et al.

If morning clouds embody a sun-synchronous thermal tide, what wave mode is it?

To answer this question, it will be useful to take the counterparts into account. Afternoon clouds are orographic clouds, fixed on topographic features, so that they belong to different modes. Hence, the counterpart of morning clouds appearing in daytime may likely be evening clouds.

The central region of the morning clouds presented in this thesis was around 0900MLT, as shown in Section 10.2. On the other hand, that of evening clouds are not clearly identified. Images of Mars in this season, Fig. 6 of *Akabane et al.* [2002] for example, often lead us to think that the center of morning clouds are closer to the terminator than the 0900MLT meridian. *Akabane et al.* [2002] also shows the opacity distribution of the cloud belt in their Figs. 7-9, which comes similar results from their images. This gap is acceptable at least three reasons: First, visual impressions do not include converting the on-image coordinate into geometric coordinate, so that clouds on the limbs are usually wider than you see on the image. Second, the Minnaert

function adopted in both their and our estimation has a difficulty that this general law breaks down completely at the limb of a planet where the emergent angle reaches 90° (if the index $k_{\rm M} < 1$ the calculated brightness becomes infinite and if $k_{\rm M} > 1$ the limb brightness is zero), so that estimated optical thicknesses in the earliest morning part and in the latest evening part are of less confidence. Third, sun-fixed stable morning clouds are not "stable" exactly. It is more natural for the clouds to move around to some extent even if they come from the processes of synoptic scale.

If we assume, based on Figs. 6-9 of *Akabane et al.* [2002], that the centers of morning and evening clouds should be near the terminators, and that morning and evening clouds belong to the same wave mode, we can firstly suppose that the semidiurnal tide (wavenumber 2) may be prominent and also may form these clouds. This idea is consistent with the common understanding that this mode is expected to the most prominent mode next to the diurnal tide (wavenumber 1). Morning and evening clouds are formed in the horizontal convergence (preferably with upward flows) induced by the semidiurnal mode, which is expected to be more prominent by our theory. It will not make any difference to assume the morning cloud's center may be around 0900MLT, however, without some more clues we can not rule out in this case possibilities of wave modes of wavenumber 3 instead of the semidiurnal tide, though those of wavenumber 3 is in general weaker than the semidiurnal components.

Flows induced by the diurnal mode may be the second most possible. Further investigation for them will be surely needed, which is beyond the scope of this thesis.

In anyway, the scenario we suggest here for the cloud dissipation, which is based on the above-mentioned tidal motions, is as follows:

Dissipation of thermal tides/waves. The solar flux is minimized around the northern summer solstice. The daytime-nighttime difference of the atmospheric heating by the ground surface is expected to thus relatively decreased, which will weaken the thermal tides/waves accordingly. In addition to this, the increase of water vapor in the low-latitude and the preferable condition for forming the cloud belt in this period (see Section 15.3) may thus apparently hide the motions due to the thermal tides/waves.

Reappearance of thermal tides/waves. Thereafter, the solar insolation increases as Mars approaches the northern autumnal equinox. Because the specific heat of the Martian atmosphere is small, atmospheric response to the heating by the ground surface is rapid, and the expected increase of the ground-to-atmosphere heating will thus directly and smoothly strengthen the thermal tides/waves. On the other hand, the cross-equatorial Hadley cell concurrently weakens, which abates the confinement of water vapor within the tropics, resulting in enervation of the cloud belt activity.

In accordance with this scenario, we can also note that although the division of the cloud belt may not occur apparently if the belt's activity is too strong, the cloud activity may be expected to localize. We concludingly give these two suggestions:

(1) The morning clouds before the formation of the cloud belt may by interpreted as the sun-fixed (topographically traveling) tidal wave.

(2) The cloud belt division may be interpreted as disturbance (or interference) of the less activated cloud belt by the more activated stationary topography-fixed tidal wave superimposed.

If our hypothesis that we see thermal waves of tides in the divided clouds and morning/evening clouds are real, Earth-based observations will have a new potential for the Mars science in this century. Observations of global waves are scarce, a fact which we hope to (even partially) remedy with our works. Tidal theory on Mars may become the most challenging and therefore, in a sense, the central study of this 21st century in "areoclimatology."

C.2 Surface Properties

As stated in Chapter 8, the opposition effect of the Martian ground should be the major cause of the phase-dependent component of blue clearings, which should be the next step to reveal the complete answer to the question. This seems to need more observations, which must be conducted in a long term, of the ground surface under a clear atmosphere on Mars. Those works will be desired to combine ground-based observations with those from spacecraft, regardless of whether past, present or in the future. The studies will also contribute the understanding the evolution and the present climate because the researches should include the surface mineralogy and the optical aspect of which will provide the radiative properties of the surface which control the thermal balance.

A rarer phenomenon is the albedo reversal seen when features imaged as dark through red filters are lighter than their surroundings on blue-filter images [e.g., *Thompson*, 1973; *Thomas and Veverka*, 1986]. This is the very rare that only a few reports are recorded in history: the comparably known is those observed around Syrtis Major in 1967 and 1971 (summarized by *Thompson* [1973]). The scarce records of this phenomenon do not allow us even to infer whether it was real or a photographic effect, still less whether it was an atmospheric phenomenon or that on the ground surface. This really is a mystery remained.

C.3 Data Assimilation

Briefly said, *data assimilation* is an idea of an algorithm that puts a sequence of observed data into a numerical simulation step by step along the calculation. *Zhang et al.* [2001] tried to assimilate some MGS TES data into the NASA/Ames Mars general circulation model (MGCM). Similarly, it should be possible to combine data from ground-based observations and numerical simulations. If it is achieved, the assimilation will provide more reliable and fruitful results than in a single way, though it may be restricted to synoptic or global scale phenomena. Development of such algorithms may be challenging, but those who will achieve will be highly appreciated and will encourage many ground-based observers.

Acknowledgments

First of all, I extend my particular thanks to Prof. T. Akabane for his years of cheerful, devoted, always stimulating support and collaboration. All the other collaborators, Prof. K. Iwasaki of Kyoto-Gakuen University and Dr. S. M. Larson of Lunar and Planetary Laboratory (University of Arizona), are also gratefully acknowledged. I express our gratitude to the staff of the Steward Observatory for making the telescopic time available and for assistance, without whom this work would not have been successful. This thesis could not completed without the support of Prof. K. Shibata. I also thank Prof. S. Saito for providing his ephemeris softwares, Prof. Y. Narumi of Kyushu-Tokai University for his original one-dimensional energy balance model codes and his developed version of Mie scattering calculation codes. IDL Figures 2.1, 2.2, and 11.7 was kindly reproduced by Dr. T. T. Ishii of Kwasan Observatory.

The fruitful discussions with, and the kind support from Prof. M. Makita of Osaka Gakuin Junior College, Prof. K. Kawabata of Science University of Tokyo, T. Yokohata and Dr. M. Odaka of Hokkaido University, Yoshiyuki Takahashi of Tohoku University, Dr. A. Yonehara of University of Tsukuba, Dr. T. T. Takeuchi and Dr. K. Yoshikawa of University of Tokyo, K. Watarai and T. Morimoto of Kyoto University, certainly the above-mentioned collaborators, and all the people of Department of Astronomy and Kwasan and Hida Observatories of Kyoto University have been always stimulating and encouraging me, and of course progress my studies (in addition, the "Room 518" fellows around me [Dr. D. Nogami, Dr. A. Yonehara, T. Yoshizawa, S. Eto, K. Watarai, M. Iino, and J. Sudo] had/have long heard my endless, annoying, and exhausting chatters, with incredible patience. Never could I have done, absolutely. Here I would like to offer them a thousand of my heartfelt apologies and special thanks!!!).

I could not thank any more to my family with love for supporting my research life; my wife Kaori, my mother Kihiko, and my brother Masahiro, and in particular, my father Kazuyoshi of blessed memory.

Bibliography

Akabane, T., M. Matsui, K. Ishiura, A. Hattori, K. Iwasaki, Y. Saito, T. Asada, S. Saito, and Y. Nakai, Photographic observations of Mars during the 1977-1978 opposition, *Contrib. Kwasan Hida Obs.*, Univ. Kyoto, No. 242, 1980.

Akabane, T., K. Iwasaki, Y. Saito, and Y. Narumi, The optical thickness of the blue-white cloud near Nix Olympica of Mars in 1982, *Publ. Astron. Soc. Jpn.*, *39*, 343-359, 1987.

Akabane, T., K. Iwasaki, Y. Saito, and Y. Narumi, Blue clearing of Syrtis Major at the 1982 opposition, *J. Geophys. Res.*, *95*, 14,649-14,655, 1990.

Akabane, T., Y. Saito, K. Iwasaki, and L. J. Martin, The north polar hood in early autumn on Mars, *Astron. Astrophys., 304*, 595-601, 1995.

Akabane, T., and K. Iwasaki, Blue clearing phenomena and equatorial clouds in the Syrtis Major region of Mars: 1997 Observations, paper presented at 30th ISAS Lunar and Planetary Symposium, Inst. of Space and Astron. Sci., Sagamihara, Kanagawa, Japan, 1997.

Akabane, T., T. Nakakushi, K. Iwasaki, and S. M. Larson, Mars: The opacity of the equatorial cloud belt in 1997 and 1999, paper presented at 32nd ISAS Lunar and Planetary Symposium, Inst. of Space and Astron. Sci., Sagamihara, Kanagawa, Japan, 1999.

Akabane, T., T. Nakakushi, K. Iwasaki, and S. M. Larson, Elysium afternoon cloud of Mars: 1999 Observations, paper presented at 33rd ISAS Lunar and Planetary Symposium, Inst. of Space and Astron. Sci., Sagamihara, Kanagawa, Japan, 2000.

Akabane, T., T. Nakakushi, K. Iwasaki, and S. M. Larson, Martian polar hoods and polar cap in 2001, paper presented at 34th ISAS Lunar and Planetary Symposium, Inst. of Space and Astron. Sci., Sagamihara, Kanagawa, Japan, 2001.

Akabane, T., T. Nakakushi, K. Iwasaki, and S. M. Larson, Diurnal variation of Martian water-ice clouds in Tharsis region of the low latitude cloud belt: Observations in 1995-1999 apparitions, *Astron. Astrophys., 384*, 678-688, 2002.

Banfield, D., B. Conrath, J. C. Pearl, M. D. Smith, and P. Christensen, Thermal tides and stationary waves on Mars as revealed by Mars Global Surveyor thermal emission spectrometer, *J. Geophys. Res.*, *105*, 9521-9537, 2000.

Baum, W. A., Earth-based observations of Martian albedo changes, *Icarus*, *22*, 363-370, 1974.

Beish, J. D., and D. C. Parker, Meteorological Survey of Mars, 1969-1984, *J. Geophys. Res.*, *95*, 14,657-14,675, 1990.

Boyce, P. B., and D. T. Thompson, A new look at the Martian "violet haze" problem, I, Syrtis Major-Arabia, 1969, *Icarus*, *16*, 291-303, 1972.

Briggs, G. A., K. Thorpe, J. Wellman, and W. Baum, *J. Geophys. Res.*, *82*, 4121-4149, 1977.

Briggs, G. A., and C. B. Leovy, Mariner 9 observations of the Mars north polar hood, *Bull. Am. Meteorol. Soc.*, *55*, 278-296, 1974.

Blumsack, S. L., P. J. Gierasch, and W. R. Wessel, An analytical and numerical study of the Martian planetary boundary layer over slopes, *J. Atmos. Sci.*, *30*, 66-82, 1973.

Carr, M. H., *Water on Mars*, Oxford Univ. Press, New York, 1996.

Chandrasekhar, S., *Radiative Transfer*, Dover, 1960.

Chapman, S. and R. S. Lindzen, *Atmospheric Tides*, D. Reidel Publishing Company, Dordrecht, Holland, 1970.

Christensen, P. R., and R. W. Zurek, Martian north polar hazes and surface ice: Results from the Viking Survey/Completion mission, *J. Geophys. Res.*, *89*, 4587-4596, 1984.

Clancy, R. T., A. W. Grossman, M. J. Wolff, P. B. James, D. J. Rudy, Y. N. Billawala, B. J. Sandor, S. W. Lee, and D. O. Muhleman, Water vapor saturation at low altitudes around Mars aphelion: A key to Mars' climate?, *Icarus*, *122*, 36-62, 1996.

Clancy, R. T., B. J. Sandor, M. J. Wolff, P. R. Christensen, M. D. Smith, J. C. Pearl, B. J. Conrath, and R. J. Wilson, An intercomparison of ground-based millimeter, MGS TES, and Viking atmospheric temperature measurements: Seasonal and interannual variability of temperatures and dust loading in the global Mars atmosphere, *J. Geophys. Res.*, *105* 9553-9571, 2000.

Clancy, R. T., and S. W. Lee, A new look at dust

and clouds in the Mars atmosphere: Analysis of emission-phase-function sequences from global Viking IRTM observations, *Icarus*, *93*, 135-158, 1991.

Colaprete, A., and O. B. Toon, The radiative effects of Martian Water ice clouds of the local atmospheric profile, *Icarus*, *145*, 524-532, 2000.

Curran, R. J., B. J. Conrath, R. A. Hanel, V. G. Kunde, and J. C. Pearl, Mars: Mariner 9 spectroscopic evidence for H_2O ice clouds, *Science*, *182*, 381-383, 1973.

Deirmendjian, D., Scattering and polarization properties of water clouds and hazes in the visible and infrared, *Appl. Opt.*, *3*, 187-196, 1964.

de Vaucouleurs, G. H., *Physics of the planet Mars; an introduction to areophysics*, London, Faber and Faber, 1954.

Dollfus, A., Polarization studies of planets, in *The Solar System*, vol. III, edited by G. P. Kuiper, and B. M. Middlehurst, Univ. Chicago Press, Chicago, pp. 343-399, 1961.

Dollfus, A., S. Ebisawa., E. Bowell, Polarimetric analysis of the Martian dust storm and clouds in 1971, *Astron. Astrophys., 131*, 123-136, 1984.

Dollfus, A., S. Ebisawa., D. Crussaire, Hoods, mists, frosts, and ice caps at the poles of Mars, *J. Geophys. Res.*, *101*, 9207-9225, 1996.

Erard, S., The 1994-1995 apparition of Mars observed from Pic-du-Midi, *Planet. Space Sci.*, *48*, 1271-1287, 2000.

Flasar, F. M, and R. M. Goody, Diurnal behaviour of water on Mars, *Planet. Space Sci.*, *24*, 161-181, 1976.

French, R. G., P. J. Gierasch, B. D. Popp, and R. J. Yerdon, Global patterns in cloud forms on Mars, *Icarus*, *45*, 468-493, 1981.

Gierasch, P., The north-south martian divide, *Nature*, *416*, 269-270, 2002.

Golombek, M. P., et al., Overview of the Mars Pathfinder mission and assessment of landing site predictions, *Science*, *278*, 1743-1752, 1997.

Haberle, R. M., J. B. Pollack, J. R. Barnes, R. W. Zurek, C. B. Leovy, J. R. Murphy, H. Lee, and J. Schaeffer, Mars atmospheric dynamics as simulated by the NASA Ames general circulation model. 1. The zonal-mean circulation, *J. Geophys. Res.*, *98*, 3093-3123, 1993.

Haberle, R. M., M. M. Joshi, J. R. Murphy, J. R. Barnes, J. T. Schofield, G. Wilson, M. Lopez-Valverde, J. L. Hollingsworth, A. F. C., Bridger, and J. Schaeffer, General circulation model simulation of the Mars Pathfinder atmospheric structure instrument/meteorology data, *J. Geophys. Res.*, *104*, 8957-8974, 1999.

Hansen, G. B., Control of the radiative behavior of the Martian polar caps by surface CO_2 ice: Evidence from Mars Global Surveyor measurements, *J. Geophys. Res.*, *104*, 16,471-16,486, 1999.

Hansen, J. E., and L. D. Travis, Light scattering in planetary atmospheres, *Space Sci. Rev.*, *16*, 527-610, 1974.

Hapke, B., Bidirectional reflectance spectroscopy, 1. Theory, *J. Geophys. Res.*, *86*, 3039-3054, 1981.

Hapke, B., Theory of Reflectance and Emittance Spectroscopy, in *Topics in Remote Sensing*, Cambridge Univ. Press, New York, 1993.

Hattori, K., and T. Akabane, Photographic observations of Mars during the 1973 opposition, *Contrib. Inst. Astrophys. Kwasan Obs.*, Univ. Kyoto, No. 221, 1974.

Herschel, W., On the remarkable appearance of the polar regions of the planet Mars, the inclination of its axis, the position of its poles, and its spheroidal figure; with a few hints relating to its real diameter and its atmosphere, *Philos. Trans. R. Soc. London*, *24*, 233-273, 1784.

Hess, S. L., Blue haze and the vertical structure of the Martian atmosphere, *Astrophys. J.*, *127*, 743-750, 1958.

Iwasaki, K., Y. Saito, Y. Nakai, T. Akabane, E. Panjaitan, I. Radiman, and S. D. Wiramihardja, Behavior of Martian south polar cap 1986, *Publ. Astron. Soc. Jpn.*, *41*, 1083-1094, 1989.

James, P. B., J. F. Bell III, R. T. Clancy, S. W. Lee, L. J. Martin, and M. J. Wolff, Global imaging of Mars by Hubble Space Telescope during the 1995 opposition, *J. Geophys. Res.*, *101*, 18,883-18,890, 1996.

James, P. B., M. Malolepszy, and L. J. Martin, Interannual variability of Mars' south polar cap, *Icarus*, *71*, 298-305, 1987.

James, P. B., R. T. Clancy, S. W. Lee, L. Martin, R. Kahn, R. Zurek, R. Singer, and E. Smith, Monitoring Mars with the Hubble Space Telescope: 1990-1991 observations, *Icarus*, *109*, 79-101, 1994.

Japan Meteorological Agency (Ed.), *Annual Report on Climate System 2000* [CD-ROM], Japan Meteorol. Business Support Cent., Tokyo, 2001.

Kahn, R., The spatial and seasonal distribution of Martian clouds, and some meteorological implications, *J. Geophys. Res.*, *89*, 6671-6688, 1984.

Kellog, W. W., and C. Sagan, *The Atmospheres of Mars and Venus*, A report by the ad hoc panel on planetary atmospheres of the Space Science Board, publication 944, National Academy of Sciences, National Research Council, Washington, D.C., 1961.

Kuiper, G. P., *The Atmospheres of the Earth and Planets*, rev. ed., (Chicago: Univ. of Chicago press), esp. pp. 358-361, 1952.

Lee, P., S. Ebisawa, and A. Dollfus, Crystal clouds in the Martian atmosphere, *Astron. Astrophys., 240*, 520-532, 1990.

Leovy, C. B., G. A. Briggs, A. T. Young, B. A. Smith, J. Pollack, E. Shipley, and R. Widley, The Martian atmosphere: Mariner 9 television experiment progress report, *Icarus*, *17*, 373-393, 1972.

Leovy, C. B., G. A. Briggs, and B. A. Smith, Mars atmosphere during the Mariner 9 extended mission: Television results, *J. Geophys. Res.*, *78*, 4252-4266, 1973.

Lindzen, R. S., On the relation of wave behavior to source strength and distribution in a propagating medium, *J. Atmos. Sci.*, *23*, 630-632, 1966.

Liou, K. -N., A numerical experiment on Chandrasekhar's discrete-ordinate method for radiative transfer: Applications to cloudy and hazy atmospheres, *J. Atmos. Sci.*, *30*, 1303-1326, 1973.

Liou, K. -N., *An Introduction to Atmospheric Radiation*, Academic Press, New York, Chapter 6, pp. 176-233, 1980.

Lumme, K., L. J. Martin, and W. A. Baum, Theoretical interpretation of photometric properties of the Martian surface and atmosphere, *Icarus*, *45*, 379-397, 1981.

Magalhães, J. A., J. T. Schofield, and A. Seiff, Results of the Mars Pathfinder atmospheric structure investigation, *J. Geophys. Res.*, *104*, 8943-8956, 1999

Martin, L. J., and W. A. Baum, A study of cloud motions of Mars, Final report, Part B, Planetary Research Center, Lowell Observatory, Flagstaff, Arizona, USA.

Martin, L. J., and W. M. Mckinney, North polar hood of Mars in 1969 (May 18-July 25). I. Blue light, *Icarus*, *23*, 380-387, 1974.

Martin, L. J., 1973 dust storm on Mars: Maps from hourly photographs, *Icarus*, *29*, 363-380, 1976.

Martin, L. J., P. B. James, A. Dollfus, K. Iwasaki, and J. D. Beish, Telescopic observations: Visual, photographic, polarimetric, in *Mars*, edited by H. H. Kieffer, B. M. Jakosky, C. W. Snyder, and M. S. Matthews, Univ. Arizona Press, Tucson, 34-70, 1992.

McCord, T. B., and J. A. Westphal, Mars: Narrowband photometry, from 0.3 to 2.5 microns, of surface regions during the 1969 apparition, *Astrophys. J.*, *168*, 141-153, 1971.

McCord, T. B., J. H. Elias, and J. A. Westphal, Mars: The spectral albedo (0.3-2.5μ) of small bright and dark regions, *Icarus*, *14*, 245-251, 1971.

Miyamoto, S., Meteorological observations of Mars during the 1965 opposition, *Contrib. Inst. Astrophys. Kwasan Obs.*, Univ. Kyoto, No. 141, 1965.

Miyamoto, S., Meteorological observations of Mars during the 1967 opposition, *Contrib. Inst. Astrophys. Kwasan Obs.*, Univ. Kyoto, No. 169, 1968.

Miyamoto, S., Meteorological observations of Mars during the 1973 opposition, *Contrib. Inst. Astrophys. Kwasan Obs.*, Univ. Kyoto, No. 217, 1974.

Nakakushi, T., T. Akabane, K. Iwasaki, and S. M. Larson, Mars: The cloud effect on the blue clearing in the Syrtis Major region, *J. Geophys. Res.*, *106*, 5043-5056, 2001a.

Nakakushi, T., T. Akabane, K. Iwasaki, and S. M. Larson, Preliminary analyses of the Martian aphelion cloud belt: 2001 observations, paper presented at 34th ISAS Lunar and Planetary Symposium, Inst. of Space and Astron. Sci., Sagamihara, Kanagawa, Japan, 2001b.

Nakakushi, T., T. Akabane, K. Iwasaki, and S. M. Larson, The blue clearing at Syrtis Major and its relation to equatorial clouds: 1997 and 1999 observations, in *The Fifth International Conference on Mars*, #6097. LPI Contribution No.972, Lunar and Planetary Institute, Houston (CD-ROM), 1999a.

Nakakushi, T., T. Akabane, K. Iwasaki, and S. M. Larson, The latest analyses of the optical thickness of equatorial clouds: 1997 and 1999 observations, paper presented at 32nd ISAS Lunar and Planetary Symposium, Inst. of Space and Astron. Sci., Sagamihara, Kanagawa, Japan, 1999b.

Nakakushi, T., T. Akabane, K. Iwasaki, and S. M. Larson, Mars: Dissipating behavior of the cloud belt, *Publ. Astron. Soc. Jpn.*, *54*, L31-L34, 2002a.

Nakakushi, T., Y. Narumi, and T. Hayakawa, Mars: A numerical experiment on mean vertical distribution of water ice clouds with a one-dimensional energy balance model, paper presented at 35th ISAS Lunar and Planetary Symposium, Inst. of Space and Astron. Sci., Sagamihara, Kanagawa, Japan, 2002b.

Narumi, Y., Thermal structure of the Martian Atmosphere with the effect of dust, (in Japanese), *J. Res. Inst. General Edu.* (Kyushu Tokai Univ.), *6*, 23-39, 1994.

Narumi, Y., Temperature environment at the landing site of Mars Polar Lander (in Japanese), *J. Res. Inst. General Edu.* (Kyushu Tokai Univ.), *12*, 59-74, 2000.

National Astronomical Observatory (Ed.), Part of Astronomy, in *Chronological Scientific Tables*

2002 (*Rika Nenpyo*, in Japanese), pp. 81-184, Maruzen Co. Ltd., 2001.

Parker, D. C., J. D. Beish, D. M. Troiani, D. P. Joyce, and C. E. Hernandez, Telescopic observations of Mars, 1996-1997: Results of the Marswatch Program, *Icarus*, *138*, 3-19, 1999.

Pearl, J. C., M. D. Smith, B. J. Conrath, J. L. Bandfield, and P. R. Christensen, Observations of Martian ice clouds by the Mars Global Surveyor Thermal Emission Spectrometer: The first Martian year, *J. Geophys. Res.*, *106*, 12,325-12,338, 2001.

Pickersgill, A. O., and G. E. Hunt, An examination of the formation of linear lee waves generated by giant Martian volcanoes, *J. Atmos. Sci.*, *38*, 40-51, 1981.

Pollack, J. B., and J. N. Cuzzi, Scattering by nonspherical particles of size comparable to a wavelength: A new semiempirical theory and its application to tropospheric aerosols, *J. Atmos. Sci.*, *37*, 868-881, 1980.

Pollack, J. B., D. Colburn, R. Kahn, J. Hunter, W. Van Camp, C. E. Carlston, and M. R. Wolfe, Properties of aerosols in the Martian atmosphere, as inferred from Viking lander imaging data, *J. Geophys. Res.*, *82*, 4479-4496, 1977.

Pollack, J. B., D. S. Colburn, F. M. Flasar, R. Kahn, C. E. Carlston, and D. Pidek, Properties and effects of dust particles suspended in the Martian atmosphere, *J. Geophys. Res.*, *84*, 2929-2945, 1979.

Pollack, J. B., M. E. Ockert-Bell, and M. K. Shepard, Viking lander image analysis of Martian atmospheric dust, *J. Geophys. Res.*, *100* 5235-5250, 1995.

Richardson, M. I., and R. J. Wilson, A topographically forced asymmetry in the martian circulation and climate, *Nature*, *416*, 298-301, 2002.

Richardson, M. I., Comparison of microwave and infrared measurements of Martian atmospheric temperatures: Implications for short-term climate variability, *J. Geophys. Res.*, *103*, 5911-5918, 1998.

Richardson, R. S., and P. E. Roques, An example of the blue clearing observed 74 days before opposition, *Publ. Astron. Soc. Pac.*, *71*, 321-323, 1959.

Sassen, K., and K. -N. Liou, Scattering of polarized laser light by water-droplet, mixed-phase and ice crystal clouds, part I, Angular scattering patterns, *J. Atmos. Sci.*, *36*, 838-851, 1979.

Schofield, J. T., J. R. Barnes, D. Crisp, R. M. Haberle, S. Larsen, J. A. Magalhães, J. R. Murphy, A. Seiff, and G. Wilson, The Mars Pathfinder Atmospheric Structure Investigation/Meteorology (ASI/MET) experiment, *Science*, *278*, 1752-1758, 1997.

Slipher, E. C., An outstanding atmospheric phenomenon on Mars, *Publ. Astron. Soc. Pac.*, *289* 137-140, 1937.

Slipher, E. C., *The Photographic Story of Mars*, Sky Publishing, Cambridge, Mass., 1962.

Smith, P. H., and M. Lemmon, Opacity of the Martian atmosphere measured by the Imager for Mars Pathfinder, *J. Geophys. Res.*, *104*, 8975-8985, 1999.

Smith, M. D., et al., The global topography of Mars and implications for surface evolution, *Science*, *284*, 1495-1503, 1999.

Smith, M. D., J. C. Pearl, B. J. Conrath, and P. R. Christensen, Thermal Emission Spectrometer results: Mars atmospheric thermal structure and aerosol distribution, *J. Geophys. Res.*, *106*, 23,929-23,945, 2001.

Smith, P. H., et al., Results from the Mars Pathfinder camera, *Science*, *278*, 1758-1765, 1997.

Smith, S. A., and B. A. Smith, Diurnal and seasonal behavior of discrete white clouds on Mars, *Icarus*, *16*, 509-521, 1972.

Snyder, C. W., and V. I. Moroz, Spacecraft exploration of Mars, in *Mars*, edited by H. H. Kieffer, B. M. Jakosky, C. W. Snyder, and M. S. Matthews, Univ. Arizona Press, Tucson, 71-119, 1992.

Stamnes, K., and H. Dale, A new look at the discrete ordinate method for radiative transfer calculations in anisotropically scattering atmospheres. II: Intensity computations, *J. Atmos. Sci.*, *38*, 2696-2706, 1981.

Stamnes, K., and R. A. Swanson, A new look at the discrete ordinate method for radiative transfer calculations in anisotropically scattering atmospheres, *J. Atmos. Sci.*, *38*, 387-399, 1981.

Stamnes, K., S.-C. Tsay, W. Wiscombe, and I. Laszlo, DISORT, a general-purpose fortran program for discrete-ordinate-method radiative transfer in scattering and emitting layered media: Documentation of methodology(version 1.1), 2000.

Stamnes, K., S.-C. Tsay, W. Wiscombe, and K. Jayaweera, Numerically stable algorithm for discrete-ordinate-method radiative transfer in multiple scattering and emitting layered media, *Appl. Opt.*, *27*, 2502-2509, 1988.

Tamppari, L. K., R. W. Zurek, and D. A. Paige, Viking era water-ice clouds, *J. Geophys. Res.*, *105*, 4087-4107, 2000.

Thomas, P., and J. Veverka, Red/violet contrast re-

versal on Mars: Significance for eolian sediments, *Icarus*, *66*, 39-55, 1986.

Thompson, D. T., Time variation of Martian regional contrasts, *Icarus*, *20*, 42-47, 1973.

Thorpe, T. E., Martian surface properties indicated by the opposition effect, *Icarus*, *49*, 398-415, 1982.

Toigo, A. D., and M. I. Richardson, Seasonal variation of aerosols in the Martian atmosphere, *J. Geophys. Res.*, *105*, 4109-4121, 2000.

Tomasko, M. G., L. R. Doose, M. Lemmon, P. H. Smith, and E. Wegryn, Properties of dust in the Martian atmosphere from the Imager on Mars Pathfinder, *J. Geophys. Res.*, *104*, 8987-9007, 1999.

Warren, S. G., Optical constants of ice from the ultraviolet to the microwave, *Appl. Opt.*, *23*, 1206-1225.

Webster, P. J., The low-latitude circulation of Mars, *Icarus*, *30*, 626-649, 1977.

Wells, R. A., *Geophysics of Mars*, Chapter 2, pp. 125-338, Elsevier Sci., New York, 1979.

Wilson, R. J., and M. I. Richardson, The Martian atmosphere during the Viking mission, 1: Infrared measurements of atmospheric temperatures revisited, *Icarus*, *145*, 555-579, 2000.

Wilson, R. J., Evidence for diurnal period Kelvin waves in the Martian atmosphere from Mars Global Surveyor TES data, *Geophys. Res. Lett.*, *27*, 3889-3892, 2000.

Wiscombe, W. J., The delta-M method: Rapid yet accurate radiative flux calculations for strongly asymmetric phase functions, *J. Atmos. Sci.*, *34*, 1408-1422, 1977.

Wolff, J. M., J. F. Bell III, P. B. James, R. T. Clancy, and S. W. Lee, Hubble Space Telescope observations of the Martian aphelion cloud belt prior to the Pathfinder mission: Seasonal and interannual variations, *J. Geophys. Res.*, *104*, 9027-9041, 1999.

Zhang, K. Q., A. P. Ingersoll, D. M. Kass, J. C. Pearl, M. D. Smith, B. J. Conrath, and R. M. Haberle, Assimilation of Mars Global Surveyor atmospheric temperature data into a general circulation model, *J. Geophys. Res.*, *106*, 32,863-32,877, 2001.

Zurek, R. W., J. R. Barnes, R. M. Haberle, J. B. Pollack, J. E. Tillman, and C. B. Leovy, Dynamics of the atmosphere of Mars, in *Mars*, edited by H. H. Kieffer, B. M. Jakosky, C. W. Snyder, and M. S. Matthews, Univ. Arizona Press, Tucson, pp. 835-933, 1992.

Zurek, R. W., Surface pressure response to elevated tidal heating sources: Comparison of Earth and Mars, *J. Atmos. Sci.*, *37*, 1132-1136, 1980.

Part VI

Research Publication Activity

International Refereed Papers

1. Akabane, T., T. Nakakushi, K. Iwasaki, and S. M. Larson,
   Diurnal variation of Martian water-ice clouds in Tharsis region of the low latitude cloud belt: Observations in 1995-1999 apparitions,
   Astron. Astrophys., *384*, 678-688, 2002.
2. Nakakushi, T., T. Akabane, K. Iwasaki, and S. M. Larson,
   Mars: The cloud effect on the blue clearing in the Syrtis Major region,
   J. Geophys. Res., *106*, 5043-5056, 2001.
3. Nakakushi, T., T. Akabane, K. Iwasaki, and S. M. Larson,
   Mars: Dissipating behavior of the cloud belt,
   Publ. Astron. Soc. Jpn., *54*, L31-L34, 2002.

Non-refereed Publications

International

1. Nakakushi, T., T. Akabane, K. Iwasaki, and S. M. Larson,
   The blue clearing at Syrtis Major and its relation to equatorial clouds: 1997 and 1999 observations,
   in *The Fifth International Conference on Mars*, #6097. LPI Contribution No.972, Lunar and Planetary Institute, Houston (CD-ROM), 1999a.

Domestic

1. Akabane, T., T. Nakakushi, K. Iwasaki, and S. M. Larson,
   Mars: The opacity of the equatorial cloud belt in 1997 and 1999,
   paper presented at 32nd ISAS Lunar and Planetary Symposium, Inst. of Space and Astron. Sci., Sagamihara, Kanagawa, Japan, 1999.
2. Akabane, T., T. Nakakushi, K. Iwasaki, and S. M. Larson,
   Elysium afternoon cloud of Mars: 1999 Observations,
   paper presented at 33rd ISAS Lunar and Planetary Symposium, Inst. of Space and Astron. Sci., Sagamihara, Kanagawa, Japan, 2000.
3. Akabane, T., T. Nakakushi, K. Iwasaki, and S. M. Larson,
   Martian polar hoods and polar cap in 2001,
   paper presented at 34th ISAS Lunar and Planetary Symposium, Inst. of Space and Astron. Sci., Sagamihara, Kanagawa, Japan, 2001.
4. Iwasaki, K., T. Akabane, and T. Nakakushi, Martian south polar cap 1997-1998,
   paper presented at 33rd ISAS Lunar and Planetary Symposium, Inst. of Space and Astron. Sci., Sagamihara, Kanagawa, Japan, 2000.
5. Iwasaki, K., T. Nakakushi, and T. Akabane, Temporal halt in Martian north polar cap regression,
   paper presented at 35th ISAS Lunar and Planetary Symposium, Inst. of Space and Astron. Sci., Sagamihara, Kanagawa, Japan, 2002.
6. Nakakushi, T., T. Akabane, K. Iwasaki, and S. M. Larson,
   The latest analyses of the optical thickness of equatorial clouds: 1997 and 1999 observations,

paper presented at 32nd ISAS Lunar and Planetary Symposium, Inst. of Space and Astron. Sci., Sagamihara, Kanagawa, Japan, 1999.

7. Nakakushi, T., T. Akabane, K. Iwasaki, and S. M. Larson,
Preliminary analyses of the Martian aphelion cloud belt: 2001 observations,
paper presented at 34th ISAS Lunar and Planetary Symposium, Inst. of Space and Astron. Sci., Sagamihara, Kanagawa, Japan, 2001.
8. Nakakushi, T., T. Akabane, K. Iwasaki, and S. M. Larson, Mars: Properties of the aphelion cloud belt, paper presented at 33rd ISAS Lunar and Planetary Symposium, Inst. of Space and Astron. Sci., Sagamihara, Kanagawa, Japan, 2000.
9. Nakakushi, T., Y. Narumi, and T. Hayakawa,
Mars: A numerical experiment on mean vertical distribution of water ice clouds with a one-dimensional energy balance model,
paper presented at 35th ISAS Lunar and Planetary Symposium, Inst. of Space and Astron. Sci., Sagamihara, Kanagawa, Japan, 2002b.